Investigating the temporal, seasonal, and spatial evolution of the atmospheric boundary layer using aerosol backscatter retrieval methods

---

A Dissertation Presented to

the Faculty of the Department of Earth and Atmospheric Science

University of Houston

In Partial Fulfillment

of the Requirements for the Degree

Doctor of Philosophy

By

Vanessa A. Caicedo

May 2017

Investigating the temporal, seasonal, and spatial evolution of the atmospheric boundary layer using aerosol backscatter retrieval methods

_____

Vanessa A. Caicedo

APPROVED:

_____

Dr. Bernhard Rappenglueck, Chairman

_____

Dr. Xun Jiang

_____

Dr. Yunsoo Choi

_____

Dr. Christine Haman

_____

Dean, College of Natural Sciences and Mathematics

Acknowledgements

To my big sister Piru, this is all for you. You are my motivation and inspiration. I miss you always.

My special thanks go to Dr. Barry Lefer and Dr. Bernhard Rappenglueck, for their unfailing guidance and support throughout this dissertation. I would like to thank my dissertation committee of Dr. Yunsoo Choi, Dr. Christine Haman, and Dr. Xun Jiang for their support over the past four years. In addition, very special thanks to Dr. James Flynn and team for all their encouragement and assistance.

My deepest gratitude to my parents for their constant encouragement, support and understanding in accomplishing this goal, without them none of this would be possible. To my sister Andrea, thank you for always believing in me and keeping me sane, I could not have done this without you. Finally thank you to all my friends and family for their support and encouragement.

Investigating the temporal, seasonal, and spatial evolution of the atmospheric boundary layer using aerosol backscatter retrieval methods

---

An Abstract of a Dissertation

Presented to

the Faculty of the Department of Earth and Atmospheric Science

University of Houston

In Partial Fulfillment

of the Requirements for the Degree

Doctor of Philosophy

By

Vanessa A. Caicedo

May 2017

Abstract

The purpose of this study is to examine and implement aerosol backscatter boundary-layer height (BLH) retrieval methods to continuously investigate the temporal, seasonal, and spatial evolution of the atmospheric boundary layer height. This study first evaluates three aerosol backscatter retrieval methods against radiosonde-derived BLHs in order to arrive at the most robust and automated method. Results demonstrated the ability of the Haar Wavelet method to more accurately detect BLHs than the other two methods tested. The Haar Wavelet was then applied to aerosol backscatter measured at a coastal site in Southeast Texas. Results showed that relatively low BLHs were associated with light-moderate onshore winds, while higher BLHs were associated with high offshore winds. Additionally, BLHs did not show a clear correlation to backward trajectories; therefore local circulations in a coastal area might largely modify turbulent properties of advected air masses and thus be of more influence in the development of the BLHs than the air mass type. Next, multiple ground-based aerosol (Light Detection And Ranging) LIDARs and one airborne LIDAR were used to analyze the spatial and temporal BLH evolution over the Houston-Galveston area. Results showed that, apart from the Galveston site, the sea breeze circulation did not have an impact on the observed BLHs as the inland progression of the sea breeze happened in the afternoon hours by the time the mixed layer was fully developed. Observed BLHs were compared with those simulated by the Advanced Research Weather Research and Forecast (ARW-WRF). Model simulations displayed an overall underestimation of BLHs with a significantly larger bias over water surfaces. Additionally, both, observations and WRF

results, showed two distinct layers consisting of the near-surface sea-breeze flow, and a lofted return flow layer above. Large biases were found as the aerosol backscatter BLH was identified as the top of the return flow layer and the model derived, thermodynamically based BLH as the top of the sea breeze layer. The presence of these two layers is highly relevant. Both layers should be considered for the correct simulation of thermodynamic processes and for the vertical mixing and spatial redistribution of pollutants.

Contents

1 Introduction

The boundary layer (BL) is defined as the lowest layer in the atmosphere directly influenced by the earth's surface. The boundary layer reacts to surface forcings such as evaporation and transpiration, heat transfer, frictional drag, and terrain-produced air flows within a time scale of an hour or less (Stull, 1988). Other forcings such as pollutant emission in particular PM 2.5 (Particulate Matter) can enhance the stability of the BL and decrease the boundary layer height (Petäjä et al., 2016). Above the boundary layer is the free troposphere (FT) acting as a cap to the BL. Convection and turbulence created by surface heating leads to the gradual growth of the BL starting at sunrise, mixing gaseous compounds and particles within the convective mixing layer (ML). Above the ML is the stable entrainment zone (EZ), where the FT is entrained downward into the ML, and ML thermals overshoot upward into the EZ (Stull, 1988; Toledo et al., 2014). The ML begins to decay as surface heating and turbulence decrease eventually creating a near surface nocturnal stable layer (NSL). Left over constituents from the daytime ML form the residual layer (RL) above the NSL (Stull, 1988).

More complex BL structures can also form in specific environmental conditions such as multiple stable layers and internal boundary layers (Garratt, 1990; Stull, 1988). Complexities in the spatial and temporal BL evolution arise from surface forcings such as evaporation and transpiration, surface heat transfer, frictional drag, and terrain-induced air flows that can change the stability of the BL, the structure of the BL (i.e.,

stratified BL), and the boundary-layer height (BLH). A coastal boundary layer for example, introduces complexities and dynamics that require further detailed characterization from continuous boundary layer measurements. Coupled with local circulations such as the land/sea breeze circulation, a coastal BL can develop complex structures such as the thermal internal boundary later (TIBL), and recirculation layers.

The determination of the BLH is vital in air pollution studies as it determines the extent of vertical mixing of pollutants. While the BLH is a key parameter in air pollution modeling and air quality studies, continuous monitoring of the BL is rarely available. The most common way of retrieving the BLH has been done with the use of radiosondes. However, radiosondes are seldom launched more than a few times a day except during extensive and costly scientific campaigns in which they are only launched for the duration of the campaign. Apart from a few occasions (e.g., André and Mahrt, 1982; Berman et al., 1999; Day et al., 2010), NSL measurements are particularly uncommon since most radiosonde launches are performed during daytime ML hours. In recent years, remote sensing techniques such as Light Detection and Ranging (LIDAR), Radio Acoustic Sounding Systems (RASS) and Sonic Detection and Ranging (SODAR) systems have allowed for the continuous monitoring of the BL (Cohn and Angevine, 2000; Schäfer et al., 2000; Seibert et al., 2000; Emeis et al., 2004, 2006; Eresmaa et al., 2006; Baars et al., 2008; McKendry et al., 2009; Muñoz and Undurraga, 2010; Emeis et al., 2012; Haman et al., 2012; Milroy et al., 20112; Compton et al., 2013; Scarino et al., 2014; Wiegner and Gasteiger, 2015; Uzan et al., 2016).

The purpose of this study is to examine and implement aerosol backscatter BLH retrieval methods to investigate the temporal, seasonal, and spatial BLH evolution. This

study first evaluates aerosol backscatter retrieval methods in order to arrive at the most robust and automated method requiring the least amount of manual inspection. This is achieved by comparing three aerosol backscatter retrieval methods to radiosonde derived BLHs. The method deemed the most reliable for BLH retrieval is then implemented to long-term measurements from a coastally located Vaisala CL31 ceilometer. Next, we use multiple aerosol LIDARs including an airborne LIDAR to analyse the spatial and temporal BLH evolution in a case study over the SE Texas region. Lastly, we investigate model simulations of the BLH and compare to the LIDAR retrieved BLHs. Overall, this study aims to effectively monitor and capture the temporal, season, and spatial BLH and evolution using aerosol LIDARs platforms, and aid in the correct simulation of BLHs for air quality modeling.

2 Comparison of aerosol LIDAR retrieval methods for boundary layer height detection using ceilometer aerosol backscatter data*

2.1 Introduction

The determination of the BLH is vital in air pollution studies as it determines the extent of vertical mixing of pollutants. In recent years, ceilometers have been used for BL studies as they facilitate the continuous monitoring of BL, the nocturnal stable layer, internal aerosol layers and the nighttime residual layer (Haman et al., 2012; Haman et al., 2014; Pandolfi et al., 2013; Peña et al., 2013). The extensive data set from continuous LIDAR measurements results in the need for determining the most reliable and accurate method to be used in automated retrievals.

In order to evaluate the retrieval of BLHs from aerosol LIDARS, we tested three distinct methods. Previous studies have evaluated retrieval methods such as the study done by Haeffelin et al. (2012) reviewing various methods (automated and manual) across three LIDARs. This study in turn, evaluates a gradient method, a Haar Wavelet method, and a Cluster Analysis method to retrieve BLHs using aerosol backscatter measured by a Vaisala CL31 ceilometer located in an urban environment. These BLHs are then compared to radiosonde derived BLHs for validation in order to arrive at the automated algorithm with the least manual inspection required. The effect of cloud signals on the BLH retrieval is also observed in all retrieval methods tested and discussed in this study.

---

* This work has been previously published: Caicedo, V., Rappenglueck, B., Lefer, B., Morris, G., Toledo, D., and Delgado, R. (2016). Comparison of aerosol LIDAR retrieval methods for boundary layer height detection using ceilometer backscatter data, Atmos. Meas. Tech. Discuss.

2.2 Data and Instrumentation

This study uses Vaisala CL31 ceilometer data and radiosonde profiles measured at the University of Houston (UH) Main Campus. UH Main Campus is located about 70 kilometres (km) northwest of the Gulf of Mexico and 5 km southeast of downtown Houston. The UH CL31 was mounted a top a trailer approximately 3.5 m above ground and radiosonde launches were performed next to the CL31 trailer. A total of 85 radiosonde profiles from the Tropospheric Ozone Pollution Project were analyzed for this study but only profiles corresponding to cloud-free aerosol backscatter vertical profiles are used for the BLH detection comparison. The Tropospheric Ozone Pollution Project seeks to understand the combination of pre- and post-frontal conditions ideal to high ozone events in the Houston area using ozonesonde and radiosonde profiles. The project is focused in the Fall and Spring seasons when high ozone events are frequent. This results in the data set used containing ~43% of launches during cloudy pre-frontal conditions with a remaining 48 cloud-free launches in post-frontal clear skies. Launches between January 2011 and March 2015 are used with the highest frequency in the months of May, June, September and October. All launches occurred between 6:00 and 17:00 CST with most radiosondes launching during convective ML hours between 13:00-15:00 CST (Fig. 2.1). The effect of cloud signals is analyzed separately for each method in Section 2.4.4. In addition, this data set includes ceilometer and radiosonde data from the NASA (National Aeronautics and Space Administration) DISCOVER-AQ (Deriving Information on Surface conditions from Column and Vertically Resolved Observations Relevant to Air Quality) Texas campaign in September 2013.

2.2.1 Vaisala CL31

The Vaisala CL31 ceilometer operates at a wavelength of 905 nanometers (nm) using an indium gallium arsenide laser diode (InGasAs) system with a 1.2 microjoule (mJ) pulse for 110 nanoseconds (ns) and mean pulse repetition rate of 8192 Hertz (Hz). It uses a single lens design to both transmit and receive light signals. This design reduces the optical crosstalk between transmitter and receiver and in turn increases the signal-to-noise ratio. A beam splitter gives full overlap of the transmitter and receiver field-of-view at an altitude of 70 m (Münkel et al., 2007).

The aerosol backscatter coefficient $\beta(x,\lambda)$ or the scattering cross section per unit volume is related to the received power with the following formula:

$$P(x,\lambda) = \frac{c}{2x^2}\ P_0\, A\eta O(x)\Delta t\ \times\ \beta(x,\lambda)\tau^2(x,\lambda), \qquad (2.1)$$

where P is the optical power received by the ceilometer from distance x, c is the speed of light, Δt is the pulse duration, P_0 is the average laser power during pulse, A is the area of receiver optics, η is the receiver optics' efficiency, $O(x)$ is the range dependent overlap integral between transmitted beam and received, $\tau(x,\lambda)$ is the transmittance of the atmosphere between LIDAR and volume, λ is the wavelength of the emitted laser pulse, x is the distance between LIDAR and scattering volume and B is the sum of electronic and optical background noise (Weitkamp, 2005). Aerosol backscatter profiles with signals from clouds, rain, or fog are identified as signals higher than 2000×10^{-9} m^{-1} sr^{-1} and were not used for this BLH comparison (Kamp and McKendry, 2010).

The CL31 can measure aerosol backscatter up to 7500 m. However, the CL31 does not record these signals, but instead only accumulates aerosol backscatter intensity every 16 seconds with a maximum height of 4500 m and 10 m resolution. The CL31 ran with firmware v1.7 and noise_h2 on. For more in depth information about the instrument see Münkel et al. (2007).

2.2.2 iMet Radiosondes

Radiosondes launched at UH Main Campus are International Met Systems Incorporated model iMet-1. iMet-1 radiosondes return GPS (Global Positioning System) location, GPS altitude, wind speed and direction, pressure, temperature, and relative humidity with a 1 Hz sampling rate using a 403 MHz transmitter. Radiosondes used here have a resolution of 0.01hPa, a response time of 1s, and an accuracy of 0.5hPa for pressure measurements. Temperature sensing has a resolution of 0.01 °C, accuracy of 0.2 °C, and a response time of 2s. The humidity sensors for the radiosondes have a resolution of less than 0.1%, accuracy of 5%, and a response time of 2s. Average ascent rate for all launches was about 5 m/s.

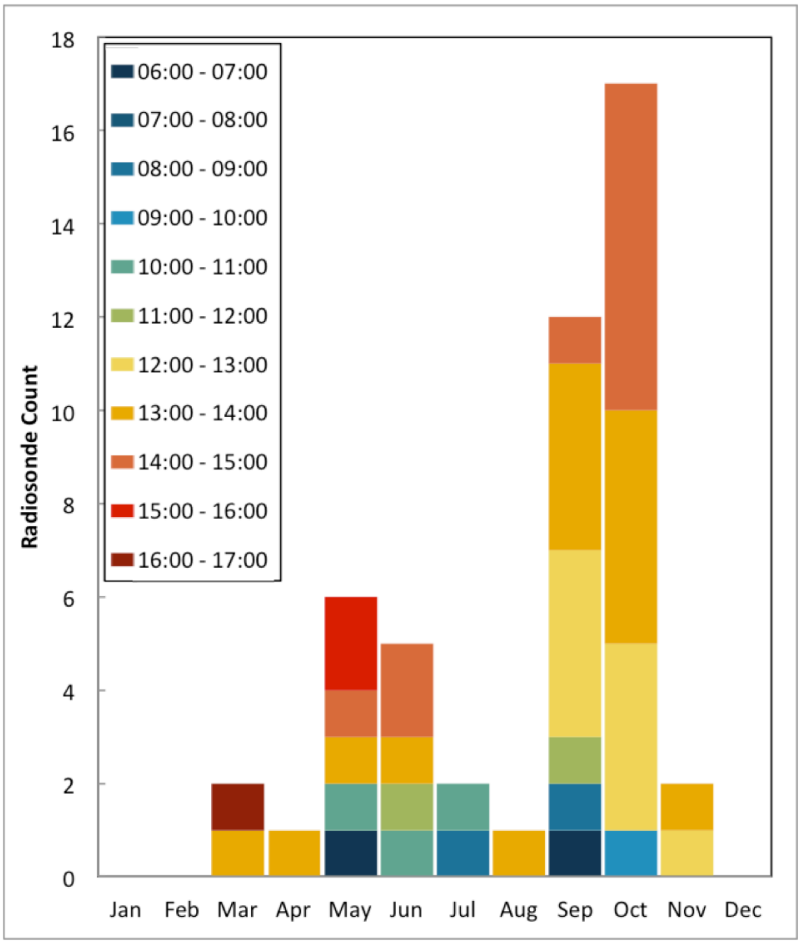

Figure 2.1. Cloud-free radiosondes used for method comparison specified by the time of launch in CST.

A total of 85 launches were analyzed for this study, but only launches corresponding to cloud-free aerosol backscatter vertical profiles are used in the retrieval method comparison. A resulting 48 launches between March 2012 and March 2015 are used with only four launches happened before 9:00, six before midday and the remaining 38 launches after midday with the highest number of launches happening from 12:00-14:00 CST (see Figure 2.1).

2.3 Boundary-Layer Height Retrieval Methods

All aerosol derived BLH methods presented here are based on two assumptions: 1) the BL contains somewhat constant concentrations of aerosols due to convective and turbulent mixing and 2) the clean FT above will create a negative gradient in aerosol backscatter from higher concentrations within the BL towards lower concentrations in the FT. The local maximum of this gradient is identified as the top of the BL (Steyn et al., 1999). Thermodynamic radiosonde BLHs are calculated using a skew-*T log-P* diagram method and are compared to aerosol derived BLHs calculated from aerosol backscatter profiles closest in time to the radiosonde launch but not exceeding 10 minutes before or after the launch.

2.3.1 Skew-*T log-P* Diagram for Radiosonde Boundary Layer Heights

A stable BL is characterized by having an environmental lapse rate greater than a moist/dry adiabatic lapse rate (Fig. 2.2a), while an unstable boundary layer is identified by having a dry adiabatic lapse rate greater than the environmental lapse rate (Fig. 2.2b). Stable profiles BLHs are identified as the top of the shallow stable layer as seen as a strong positive vertical gradient change in temperature and a strong negative gradient in dew point temperature profiles (Fig. 2.2a). BLHs during unstable conditions are identified as the base of the stable EZ (i.e., temperature inversion) where the temperature profile intersects dry adiabates and/or where relative humidity or dew point temperature profiles sharply decrease as seen in the skew-*T log-P* diagram in Fig. 2.2b (Stull, 1988; Kovalev and Eichinger, 2004; Haman et al., 2012). A previous study by

Haman et al. (2012) found a correlation coefficient of 0.96 during unstable conditions and 0.91 during stable conditions when comparing ceilometer and radiosonde derived BLHs (both manually) using the skew-*T log-P* method.

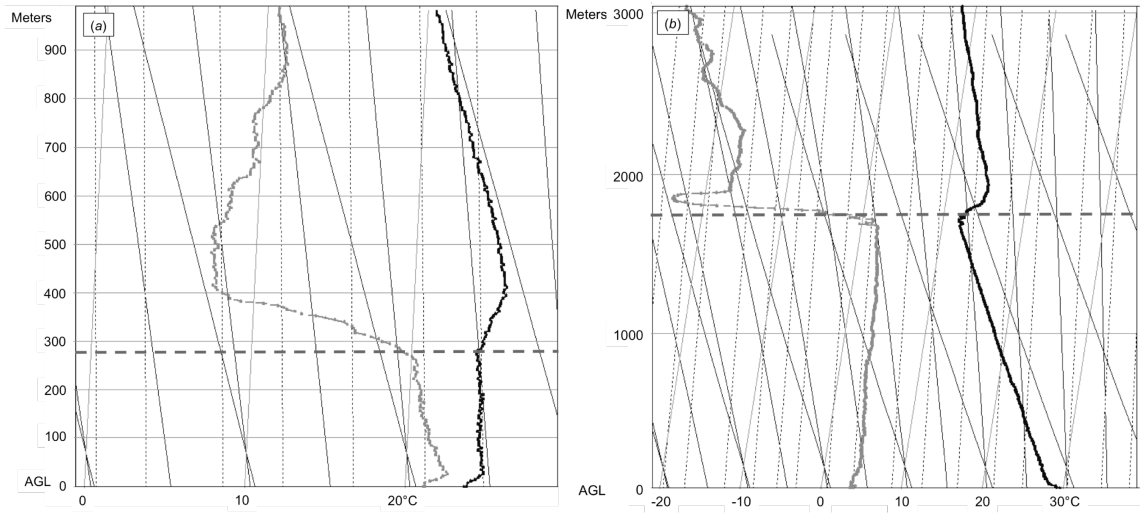

Figure 2.2. Skew-*T log-P* method for BLH detection using temperature (black) and dew point temperature (grey) for (a) stable and (b) unstable conditions with BLH shown as grey dashed line. Soundings from September 26, 2013 at 6:10 CST (a) and May 4, 2014 at 15:40 CST (b).

2.3.2 Vaisala Corporation Aerosol Backscatter Gradient

The Vaisala Corp. BL Matlab v3.7 algorithm is used in this study. This algorithm finds negative gradients with increasing altitude in aerosol backscatter profiles following the assumptions discussed in Section 2.3. A 10 minute and 120 meter height averaging is applied to the profile along with a temperature dependence curve of -10 as recommended by Vaisala Corporation (C. Münkel, pers. comm., September 2013) due to the tendency of the CL31 having a curvature in aerosol backscatter profiles with increasing internal temperatures. The temperature correction of -10 is an algorithm setting that adjusts the shape and curve of temperature affected aerosol backscatter

profiles with negligible effects on aerosol layer detection (Münkel et al., 2007; Vaisala Oyj, 2011, C. Münkel, pers. comm., April 2016).

The change in aerosol backscatter by height *(dβ/dx)* is calculated by the algorithm, which then finds the largest three negative gradients with minimum aerosol backscatter of gradient of $200 \times 10^{-9} m^{-1} sr^{-1}$. This study uses a minimum gradient height setting of 30 m along with a sensitivity setting of 15%, which requires a 15% change in the relative aerosol backscatter in the vicinity of the possible BLH. The largest of the negative gradients is usually defined as the BL (Münkel et al., 2007; Vaisala Oyj, 2011) however, the largest negative gradient does not always correspond to the BL (see results Sect. 2.4). Therefore, a manual analysis of the algorithm's three resulting layers (Fig. 2.3) is required in order to prevent the incorrect identification of other aerosol layers. The algorithm gives three maximum negative gradients every 1-minute of which one is manually chosen as the BLH. These are then averaged to 10 minutes for radiosonde comparison. The manual approach required to select one of the three maximum negative gradients as the BLH requires a priori knowledge of typical nocturnal and daytime BL heights. In addition, this manual selection analysis can be time-consuming especially when long term LIDAR data is evaluated.

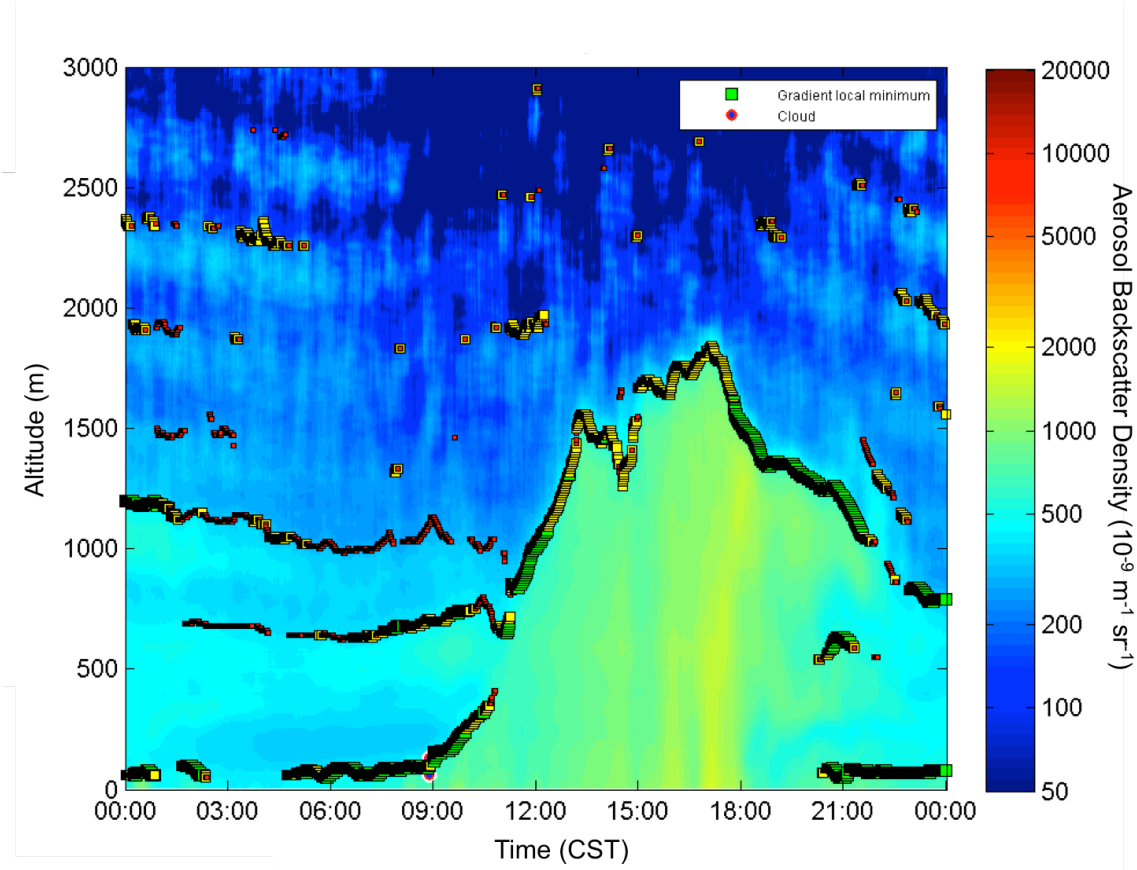

Figure 2.3. Aerosol backscatter time series for October 24, 2013. Three gradient local minimums are plotted for each 1-minute aerosol backscatter profile.

2.3.3 Cluster Analysis

This method uses variations in the measured aerosol vertical profiles for BLH calculations. The BLH is typically identified as the (temporal) variance local maximum local maximum based on the assumption that the EZ contains high aerosol variability due to clean air masses from the free atmosphere mixing with masses from the BL. The center of the EZ corresponds to the top of the BL (Hooper and Eloranta, 1986; Stull, 1988; Piironen and Eloranta, 1995).

Toledo et al. (2014) tested nonhierarchical and hierarchical cluster analysis on LIDAR retrieved vertical aerosol distribution and its variance. Both cluster methods were found to be reliable in calculating BLHs but with a tendency to overestimate the BLH compared to aerosol backscatter gradient methods. This overestimation was attributed to the gradient methods identifying the BLH as a significant decrease in signal, while the cluster method uses a local maximum in variance corresponding to the middle of the EZ. The maximum negative gradient does not always correspond to the local maximum in variance, in these cases the greater the EZ depth the greater the overestimation of the BLH (Toledo et al., 2014). Nevertheless, the cluster method offers a unique BLH, whereas aerosol gradient methods can give multiple results.

2.3.4 Data Processing for Cluster Analysis and Application

Due to low signal-to-noise ratio and noise-generated artifacts, both a 10-minute moving time average and moving height average was applied to raw aerosol backscatter profiles. Height averages were applied as seen in Table 2.1. These averaging settings were chosen as they created the most reliable cluster calculated BLHs, similar to findings in averaging done for gradient methods (Emeis et al., 2008a, b). Because the range correction needed to invert Eq. 2.1 increases noise in aerosol backscatter profiles with height, lower averaging was applied to lower altitudes while higher averaging was applied to higher altitudes (Table 2.1). This study found that these averaging settings worked best on most aerosol profiles and aerosol conditions. Typically, lower averaging than those listed in Table 2.1 caused artificial variance peaks, while greater averaging smoothed out variance peaks in the aerosol backscatter profiles. The moving time

average also leads to more profiles containing cloud signals; therefore only 45 comparisons were found to be valid for this method.

Table 2.1. Averaging heights by height range used on aerosol backscatter profiles for cluster and wavelet methods.

Altitude Range	Averaging Height
10 – 490 m	70 m
500 – 990 m	330 m
1000 – 1990 m	590 m
2000 – 4500 m	690 m

Variance V as a function of height z were then calculated from cloud-free profiles R using the following formula (Hooper and Eloranta, 1986):

$$V(z) = \frac{1}{(N-1)} \sum_{i=1}^{N} [R(z, t_i) - \overline{R}(z)^2], \quad (2.2)$$

where $R(z, ti)$ is the averaged LIDAR aerosol backscattered signal at time t_i and height z, and $\overline{R}$ is the averaged profile from N number of profiles corresponding to 10 minutes.

K-means clustering can then be applied to identify BLHs. K-means is a data-partitioning algorithm that assigns standardized 3-D point observations (height range of profile, aerosol backscatter signal, and variance) to exactly one of k clusters defined by centroids (cluster centers), where k is chosen before the algorithm starts (Anderberg, 1973; Toledo et al., 2014). The algorithm works as follows:

Step 1. Choose k initial cluster centers (centroid).

Step 2. Compute point-to-cluster-centroid Euclidean distances of all observations.

Step 3. Assign each observation to the cluster with the closest centroid.

Step 4. Compute the average of the observations in each cluster to obtain new centroid locations.

Step 5. Repeat steps 2 through 4 until cluster assignments do not change, or the maximum number of iterations is reached, whatsoever occurs first, depending on computational resources (Toledo et al., 2014).

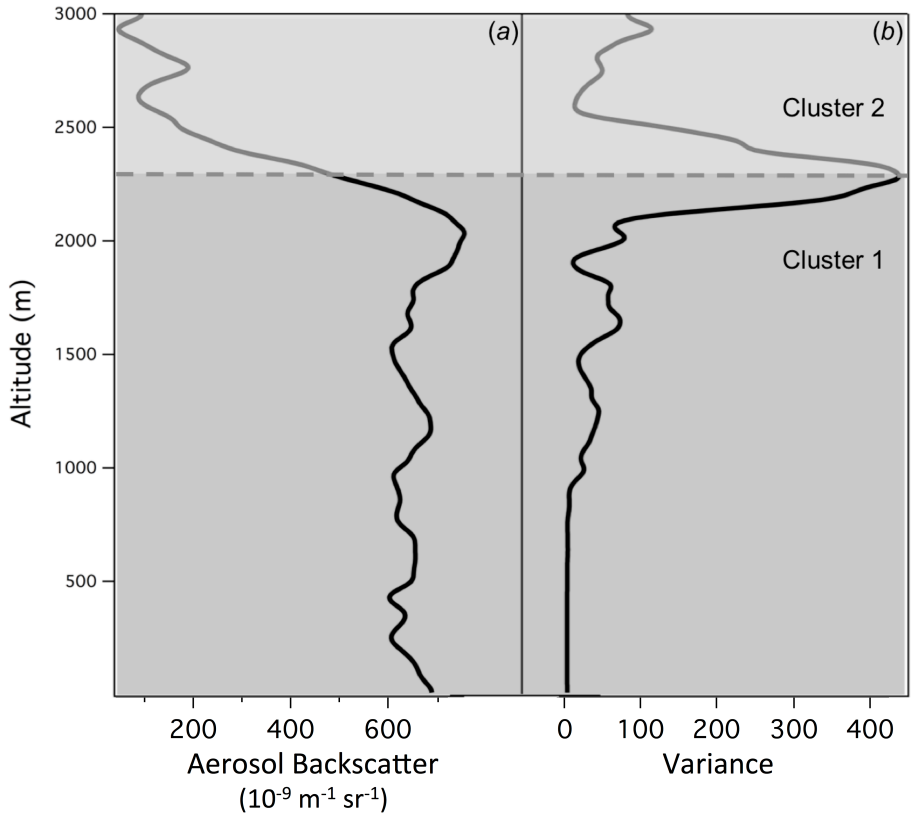

Figure 2.4. CL31 aerosol backscatter profile (a) and corresponding calculated variance (unit-less) profile (b) for September 25, 2014 at 14:30 CST. Dashed line shows the cluster derived BLH (2360 m) at the height where the variance cluster assignment changes from cluster 1 to cluster 2.

Previous determination of the number of clusters present or needed in the dataset is required for cluster validation, since the number of clusters is a parameter to be introduced into the cluster algorithm (Step 1). By choosing k=2, cluster analysis will

typically divide a well-mixed boundary layer into two clusters, one below a peak in variance corresponding to the center of the EZ, one below a peak in variance corresponding the center of the EZ, and one above the variance peak (Fig. 2.4), however profiles with increasing noise and/or lofted aerosol layers will cause the cluster analysis to assign clusters elsewhere (for detailed description of criteria see Results Section 2.4). The maximum height of these clusters are limited by the time of day to prevent the detection of other aerosol layers such as the top of the residual layer during nocturnal hours when only the NSL is of interest. Here, the maximum height for nighttime BL detection is 400 m, whereas it is 2800 m for daytime BL heights.

2.3.5 Haar Wavelet Method

Aerosol backscatter BLHs are derived with a Covariance Wavelet Transform utilizing the Haar wavelet compound step function with multiple user defined wavelet dilations (Cohn and Angevine, 2000; Davis et al., 2000; Brooks, 2003; Baars et al., 2008; Compton et al., 2013; Uzan et al., 2016). This method identifies the sharp aerosol backscatter gradient corresponding to the top of the BL by calculating the wavelet transform. The Haar wavelet function h is defined as follows:

$$h\left(\frac{z-b}{a}\right) = \begin{Bmatrix} -1: b - \frac{a}{2} \le z < b \\ +1: b \le z \le b + \frac{a}{2} \\ 0 : elsewhere \end{Bmatrix}, \tag{2.3}$$

where z is the vertical altitude in this application, a is the vertical extent or dilation of the Haar function, and b is the center of the Haar wavelet function. The covariance transform of the Haar wavelet function, w_f, is defined as:

$$w_f(a,b) = a^{-1} \int_{z_b}^{z_t} f(z) h\left(\frac{z-b}{a}\right) dz, \quad (2.4)$$

where z_t and z_b are the top and bottom altitudes in the backscatter profile, $f(z)$ is the backscatter profile as a function of altitude, and a is the normalization factor or the inverse of the dilation, respectively.

Defining the dilation factor *a* and the range of centers of *b* of the Haar wavelet function are key in correctly identifying the BLH using aerosol backscatter profiles. In this study, *b* ranges from the lowest ceilometer recorded aerosol backscatter altitude of 10 m to a maximum BLH of 2800 m. This limit was set as no previous studies have found BLHs above 2800 m and as no radiosonde derived BLHs were found above 2800 m (Haman et al., 2012; Rappenglück et al., 2008).

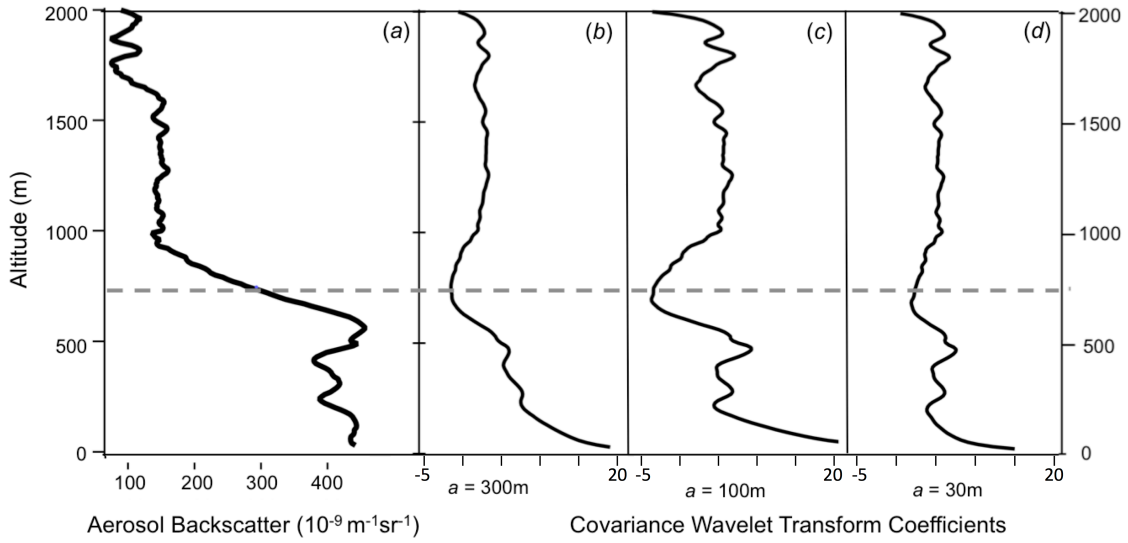

Figure 2.5. Daytime aerosol backscatter profile (a) for November 13, 2013 at 13:30 CST and (b-c) its corresponding covariance wavelet transform coefficients (unit-less) with increasing magnitudes of 30, 100, and 300 m respectively. Wavelet retrieved BLH is shown as the dashed grey line at 750 m.

As with previous studies (Brooks, 2003; Baars et al., 2008; Compton et al., 2013; Scarino et al., 2014), the dilation factor a affects the number of covariance

wavelet transform coefficients (CWTC) local minimums. Larger values create large local minimums (Fig. 2.5b and 5c) at the heights of the biggest aerosol gradients in the aerosol backscatter profile (Fig. 2.5a). Lower dilation values create numerous CWTC local minimums (Fig. 2.5d) at heights of smaller aerosol gradients in the measured profiles. A range of dilation values is applied to the aerosol backscatter profile. Here we use a maximum dilation of 30 m for nighttime BLHs since the NSL tends to have a smaller aerosol backscatter gradient than the above RL creating a need for more than one local minimum (not shown). In these cases, the CWTC local minimum closest to the surface is chosen as the BL. A higher limit of 300 m (Fig. 2.5b) for the dilation factor *a* is applied for daytime BLHs and the strongest CWTC local minimum is used to identify the sharp transition between ML and FT. This larger dilation value also serves to decrease signals from smaller aerosol gradients below the BLH. Cloud-free CL31 aerosol backscatter profiles are averaged first vertically according to Table 2.1 followed by a 10-minute average before applying the Haar Wavelet algorithm. The algorithm is applied to each averaged profile with incremental dilations until the maximum dilation factor is reached (30 m for nighttime hours and 300 m for daytime hours). The mean of all resulting CWT coefficients is then calculated and the local minimum of the mean CWT coefficients is identified as the BLH.

2.4 Results

BLH retrieval methods are evaluated and quantified against radiosonde derived BLHs using bias and standard deviation calculated in accordance to Nielsen-Gammon et al. (2008) and Haman et al. (2012). Here, the bias is the difference between the means

of aerosol retrieved BLH and the corresponding radiosonde BLH, and the standard deviation is the root-mean-square value of the departures of the individual pair sample differences from the bias. A two-sided, paired sample t-test is used to define the statistical significance of the bias:

$$t = \frac{\bar{X} - \mu}{s} \sqrt{N}, \tag{2.5}$$

where $\bar{X}$ is the mean aerosol BLH samples, μ is the radiosonde BLHs mean, S is standard deviation of samples, and N is the number of pair samples.

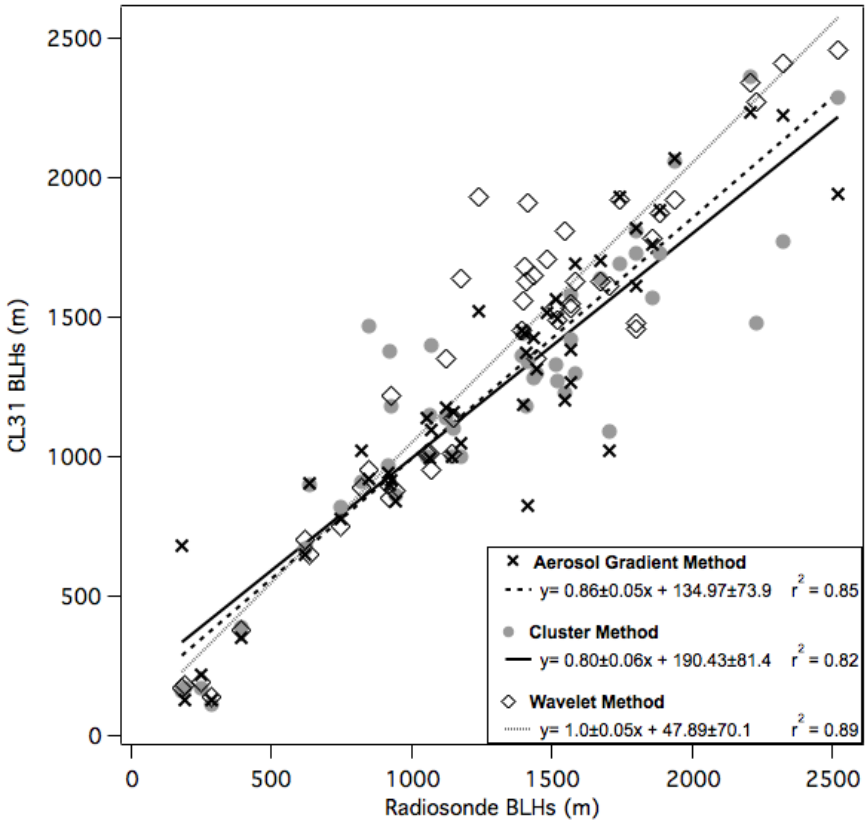

Figure 2.6. Comparison of CL31 aerosol backscatter BLHs and radiosonde derived BLHs. The three methods tested are compared to radiosonde BLHs calculated using the skew-*T log-P* method. The linear regression lines, regression line equations, and correlation coefficients r^2 are listed for each BLH retrieval method comparison.

The null hypothesis is defined as unbiased aerosol derived BLHs when compared to radiosonde BLHs. It was not rejected when the calculated t-test value (t) was within ±1.96 and the p-value was greater than 0.05 or 5% significance level, in alignment with previous approaches (Nielsen-Gammon et al., 2008; Haman et al., 2012). Correlation of all methods to radiosonde BLHs is shown in Figure 2.6 and an intercomparison of the methods in Figure 2.7. The uncertainties from the sensor were not calculated for this study as the exact aerosol backscatter profiles used in the aerosol gradient method are not given by the Vaisala algorithm and therefore the uncertainties could not be calculated equally across all BLH retrieval methods. However, Biavati et al. (2015) shows a promising new statistical method to review sensor related uncertainties in similar studies.

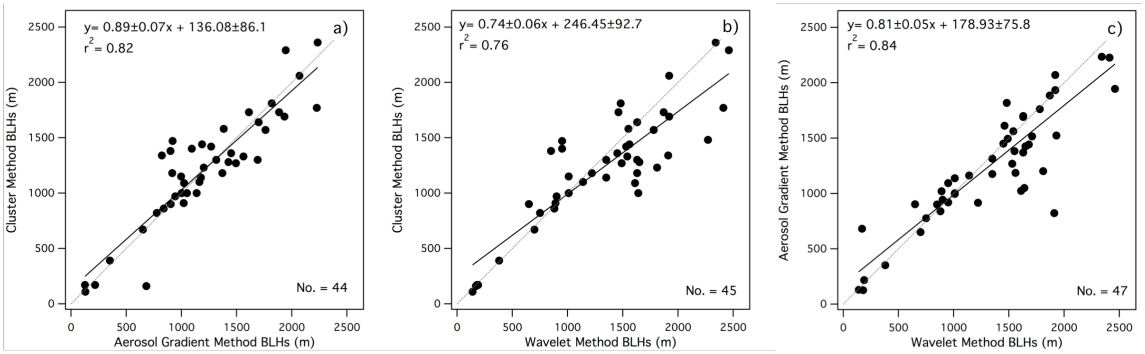

Figure 2.7. Intercomparison of all methods using cloud-free profiles. One-to-one line in dashed grey and linear regression lines in solid black.

The algorithms were applied to October 24, 2013 when two radiosondes launches corresponded to cloud-free signals. The cluster analysis and wavelet method were subjected to a 500 m height detection limit during nighttime BLH detection in order to prevent the detection of RL signals and 2800 m two hours after sunrise at 9:30

CST (afternoon BL decoupling not shown). The 500 m and 2800 m limit is chosen as it is well above the previously identified BLHs in the study area (Haman et al., 2012; Rappenglück et al., 2008). The results are shown in Figure 2.8.

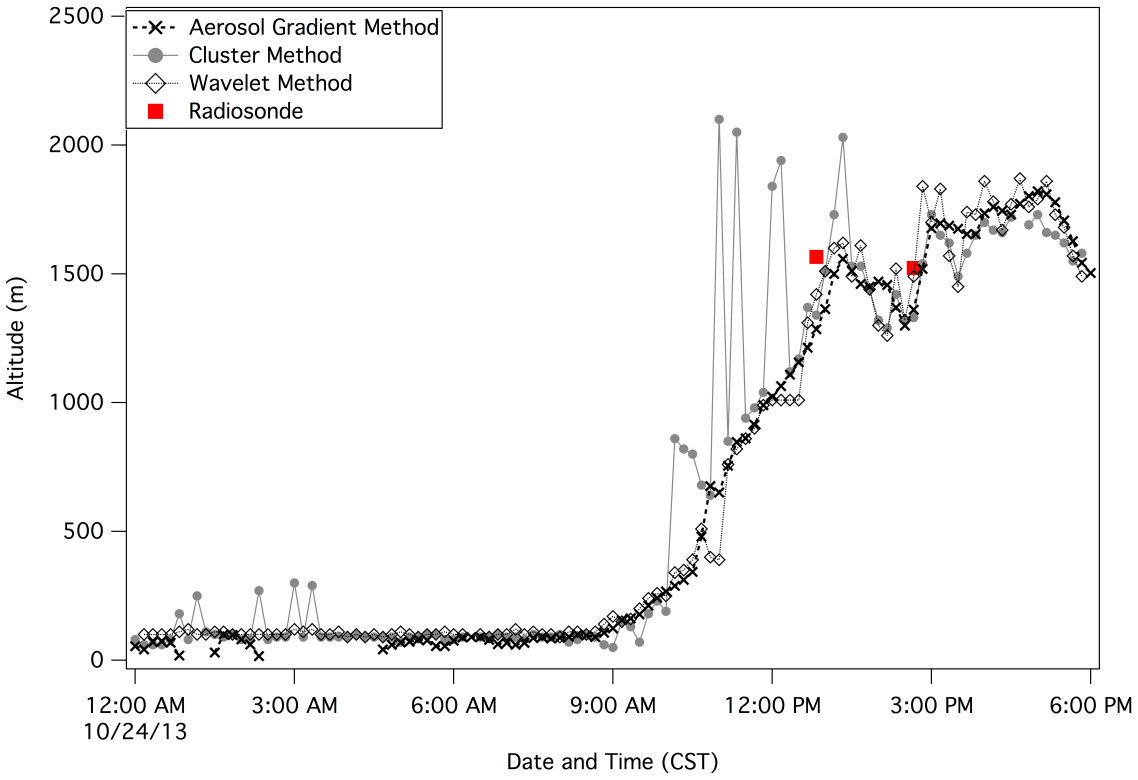

Figure 2.8. Resulting BLH for October 24, 2013 with 10-minute averages for all methods. Radiosonde estimated BLHs are shown as red squares.

2.4.1 Aerosol Backscatter Gradient Method Results

A previous study done by Haman et al. (2012) found that ceilometer BLHs derived from the aerosol backscatter gradient showed excellent correlation to radiosonde BLHs for both stable and unstable conditions, over a period of two years using more than 60 daytime radiosonde profiles. Haman et al. (2012) found the aerosol backscatter gradient capable of continuously identifying the height of the BL after

manually choosing one of the three resulting aerosol layers, with limited detection following precipitation or during periods of high wind speeds. Low aerosol content after rain events through wet deposition of aerosols and dispersion of aerosol due to high winds speeds limit the formation of aerosol layers, therefore limiting the detection of the BLH with aerosol gradients. These limitations however, are less relevant for air quality studies since typically these situations are also accompanied by lower pollutant levels (e.g. through air mass change, enhanced vertical mixing, enhanced dry deposition due to high winds, and wet removal of soluble gases during the preceding precipitation). Late afternoon hours also present a challenge since the discontinuous transition from unstable (ML) to stable boundary layer (NSL) can create multiple aerosol layers (Endlich et al., 1979; Seibert et al., 2000; Haman et al., 2012). This is still an important time period for primary pollutant concentrations as they would still be critically determined by the BLH (in particular during evening rush hour), however the diurnal peak in photochemistry activity for build-up of secondary pollutants has passed making this a less crucial time for these pollutants.

This study found similar results using 47 cloud-free radiosondes with a slight difference in correlation most likely due to the manual analysis used. Haman et al. (2012) does not report a BLH if the height of the BL is not clear while this study always reports a gradient found by the algorithm so long as algorithm is able to calculate a gradient. The manual analysis used in this study resulted in a correlation coefficient (r^2) of 0.85 was found (Fig. 2.6) when comparing the aerosol backscatter gradient BLHs to daytime radiosonde BLHs. A bias of -42.5 m and a standard deviation of 209.5 m (Table 2.2) were found (not statistically significant; $p > 0.05$). The bias indicates aerosol

gradient method BLHs are generally lower than radiosonde BLHs. The overall agreement shows the ability of this method to calculate the BLH reasonably well once one of the three calculated aerosol backscatter gradients is chosen as the BL. However, this requires a priori knowledge of typical BLHs at the measurement site and a manual inspection of aerosol gradients calculated. In addition, limited detection of the BLH was also seen in conditions with low aerosol content when the algorithm did not find strong enough gradients in the aerosol backscatter profile. No combination of available setting options was found to improve BLH detection in these conditions. Furthermore, disagreement was found when the largest gradient in an aerosol profile does not correspond to the thermodynamic BLH found using radiosonde profiles. This is due to the different assumptions in the methodologies when using aerosol gradients to detect LIDAR BLHs or thermal parameters to detect radiosonde BLHs.

Table 2.2. Bias, Standard Deviation and number of data points (No.) for comparison of BLH retrieval methods to radiosonde BLHs.

BLH Retrieval Method	Bias (m)	Standard Deviation (m)	No.
Aerosol Gradient	-42.5	209.5	47
Cluster	-61.0	243.5	45
Wavelet	51.1	187.0	48

Figure 2.8 shows a time series of BLHs reported after manual analysis and 10 minute averaging of the three calculated aerosol layers (Fig. 2.3). The gradient method is able to resolve for BLHs under stable and unstable conditions for this October day but underestimates the BLH by about 300 m and 170 m when compared to the first and second radiosonde launch respectively. Nocturnal BLHs are similar to those calculated by the wavelet and cluster analysis method but occasionally measure a lower NSL than the other two methods, likely due to the difference averages used in the aerosol gradient

method. Daytime BLHs after manual selection of the three calculated gradients is seen slightly less variable than those calculated by the cluster analysis and wavelet methods and are occasionally lower than those calculated by the wavelet method. Overall, all methods are able to capture the NSL, the growth of the BL and the peak BLH reasonably well, with the cluster method showing the most variability due to the detection of lofted aerosol layer signals incorrectly identified as the BLH. The aerosol gradient method and the wavelet method BLHs show very similar results after the manual selection of the aerosol gradient method BLHs. Figure 2.7 shows the aerosol gradient method having the best correlation with the wavelet method as expected as both search for the maximum aerosol backscatter gradients in a profile, but slightly lower agreement with the variance method. Overall, this method works well under stable and unstable conditions so long as the user is able to identify the correct BLH from the three gradients reported.

2.4.2 Cluster Method Results

CL31 BLHs using the cluster method showed a slightly lower correlation than the aerosol gradient method with a correlation coefficient of 0.82 (Fig. 2.6), a bias of -61.0 m and a standard deviation of 243.5 m (not statistically significant; see Table 2.2). Disagreements found between radiosonde and cluster derived BLHs were most commonly due to noise in aerosol backscatter profiles and lofted aerosol layers. From the 45 comparisons performed, 13.3% showed the algorithm finding a maximum variance peak not corresponding to the BL but to noise or other aerosol layers. Sixteen cases (35.5%) were found where noise created multiple variance peaks in higher

altitudes therefore the cluster analysis divided aerosol backscatter profiles into clusters of similar variance intensity (Fig. 2.9) rather than above and below a single variance peak (as seen in Fig. 2.4). This division underestimated the BLH (bias of -61.0) since the cluster was divided into relatively low variance closer to the surface and high variance in higher altitudes. This is due to the fact that CL31 displays a significant increase in noise with increasing altitude. Five instances were found where the variance maximum did not equal radiosonde derived BLH due to signals from lofted aerosol layers. In these cases a smaller maximum corresponded to the BL. These were not errors due to algorithm limitations created by noise (35.5%) but instead due to the implicit assumptions in using aerosol backscatter for BLH detection (constant aerosol backscatter signals within the BL and a negative gradient in aerosol backscatter corresponds to the top of the BL). When compared to the wavelet and aerosol gradient method, the cluster analysis agrees well with the aerosol gradient method ($r^2 = 0.82$) but lightly less with the wavelet method ($r^2 = 0.76$) as seen in Figure 2.7.

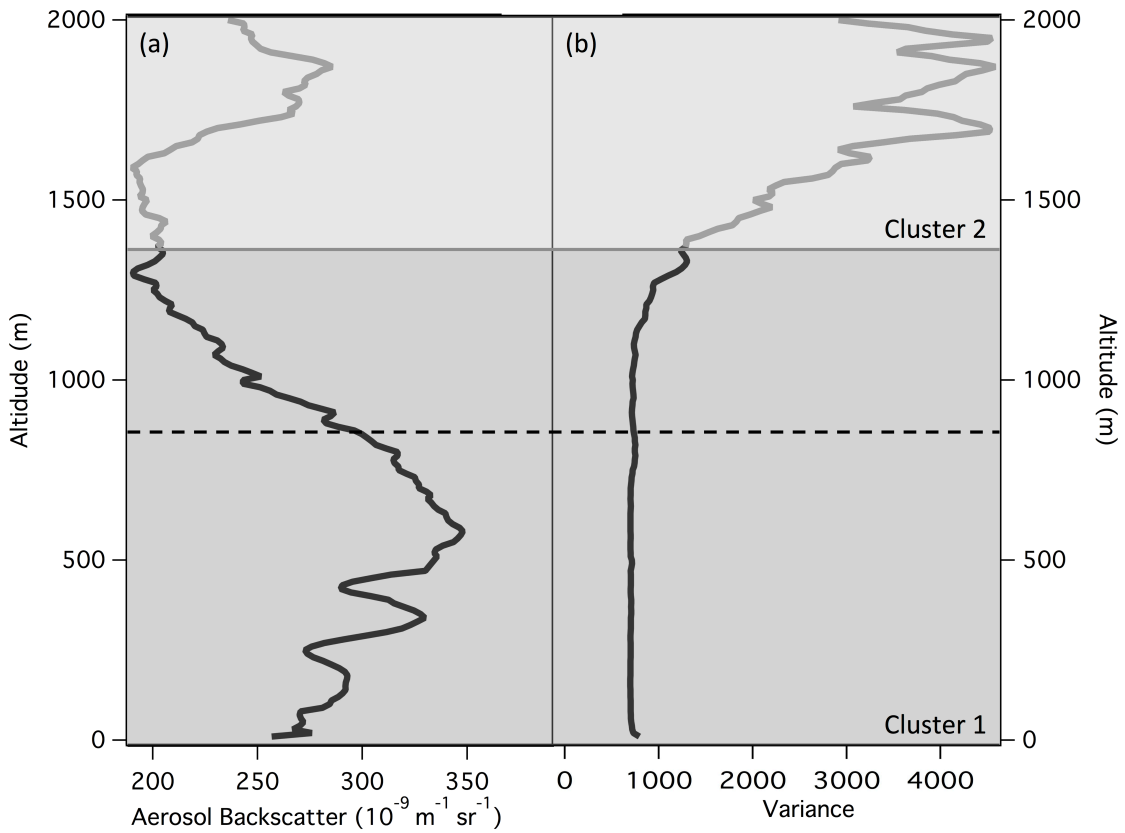

Figure 2.9. Aerosol backscatter profile (a) on October 19, 2013 at 14:00 CST and corresponding calculated variance (unit-less) profile (b) showing division of cluster analysis and estimated BLH (1370 m) at the transition from low to high variance. Radiosonde BLH is shown as a dashed line at 850 m.

The errors calculated by other aerosol layers can be seen to occur during October 24, 2013 (Fig. 2.8). Here, the cluster method mistakenly identifies signals higher than the BL, some of which the aerosol gradient method also identified (see Fig. 2.3) but were manually rejected as a possible BLH candidates. When compared to the radiosondes launched in this day the cluster analysis does well but slightly underestimating the BLH by no more than 100 m in the first launch and 250 m in the second launch. The cluster analysis method does well during the nocturnal hours when the algorithm is limited by height preventing the detection of the RL, but errors occur

when the nighttime signals are assigned to clusters according to noise similar to the profile shown in Figure 2.9.

2.4.3 Wavelet Method Results

The Haar wavelet method showed excellent agreement when compared to 48 radiosonde BLHs with a correlation coefficient of 0.89 (Fig. 2.6). Statistical analysis showed a bias of 51.1 m (not statistically significant) and a standard deviation of 187.0 m (Table 2.2). Disagreement was found when aerosol backscatter profiles contained multiple sharp gradients corresponding to lofted aerosol layers (~12.5% of total cases). These shallow aerosol layers often have stronger gradients than that of the BL. In these cases, the second largest gradient is very often the BL (~67%). In addition, another ~10% of total cases showed deviations where the radiosonde derived BLH did not correspond to the greatest gradient in the aerosol profile as shown in Figure 2.10. This disagreement and positive bias found can be attributed to the differences in determining BLHs using aerosols and thermodynamically using radiosondes. Aerosols can penetrate into the stable layer transporting aerosols to higher altitudes than the BLH (inversion height) causing an overestimation of aerosol derived BLHs (McElroy and Smith, 1991; Seibert et al., 2000). Removing the ~22.5% of deviations falling into the cases described above would improve the correlation drastically (r^2 = 0.98). This provides confidence that all potential causes for deviations were identified. Overall, the wavelet method showed the best correlation of all methods when compared to radiosondes. In particular, this method was superior in the detection of BLHs in profiles with low

aerosol backscatter. Under these conditions it was able to resolve weaker local maximums thus reasonably capturing the BLH. This method was also less affected by noise than the gradient method or the cluster method. The wavelet method is shown to perform well with the addition of a height restraint for nocturnal BLH retrievals (Fig. 2.8) in order to prevent the detection of RL signals or lofted aerosol layers. Other methods to prevent the incorrect detection of the BLH include those proposed by de Haij et al. (2016), Di Giuseppe et al. (2012), and Pal et al. (2013). However, our study uses the height restraint as it has shown to successfully prevent the detection of RL signals in the example shown in Figure 2.8. Both wavelet estimated BLHs are within 30 m of the radiosonde derived BLHs. The comparison with the cluster and gradient methods in Figure 2.7 shows this method generally agrees well with the aerosol gradient method ($r^2 = 0.84$) but appears to calculate the BLH slightly lower than the wavelet method most likely due to difference averaging quantities used. The correlation with the variance method of $r^2 = 0.76$ is most likely due to the noise sensitivity of the cluster analysis method and the calculation of a BLH by using the variance of an aerosol backscatter profile versus finding a gradient in an aerosol backscatter profile.

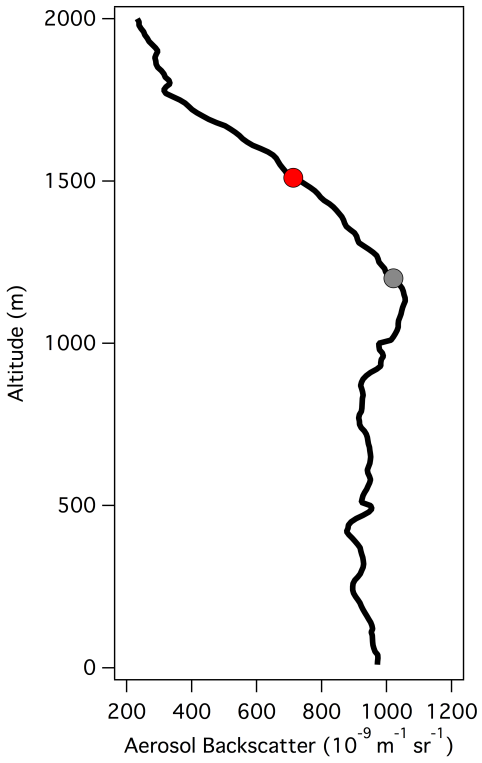

Figure 2.10. Aerosol backscatter profile for October 20, 2014 at 14:00 CST where radiosonde derived BLH does not correspond to the height of the largest negative gradient in the aerosol backscatter profile. Radiosonde BLH at 1290 m is shown as a grey circle and wavelet method derived BLH at 1510 m is shown as a red circle.

2.4.4 BLH Retrieval with cloud signals

The identification of the BLH is more difficult in the presence of clouds when aerosol backscatter algorithms identify the strong signals of the cloud layer as the BLH. Strong cloud signals (>2000×10^{-9} m^{-1} sr^{-1}) can limit the detection of the BLH due to the extinction of the aerosol backscatter signals above cloud layers. The effect of these cloud signals is observed for all BLH retrieval methods (not including fog or rain events). Although this study observes daytime cloud signals, continuous ceilometer

measurements may find similar signals during nighttime hours therefore our findings are not limited to daytime convective mixed layers.

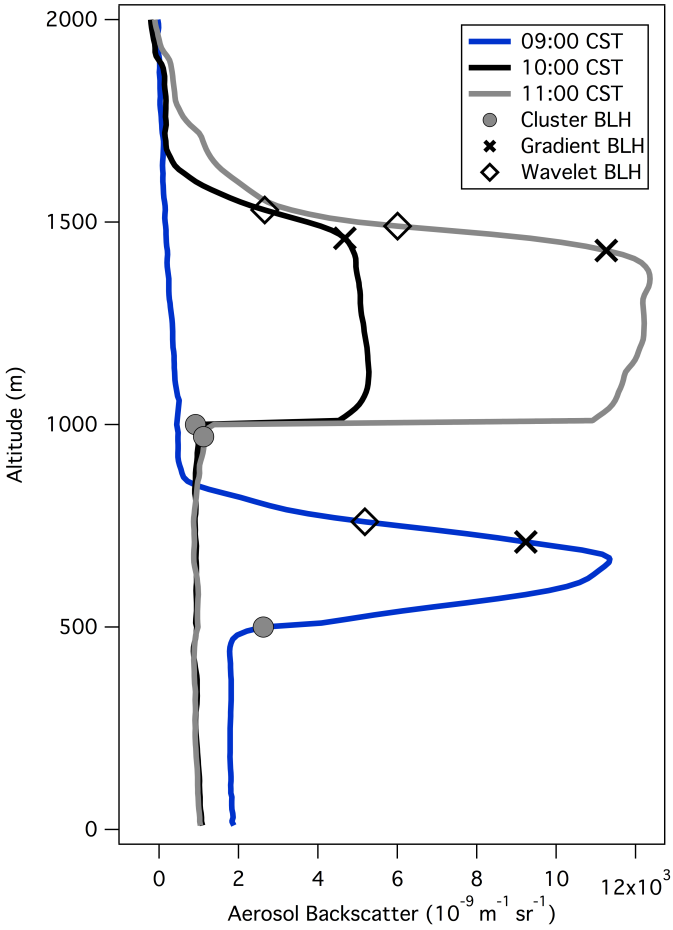

Figure 2.11. Aerosol backscatter profiles on September 15, 2013 measured at 09:00 CST (blue), 10:00 CST (black), and 11:00 CST (grey). BLHs retrieved by each method are shown on all profiles. Cloud layers signals measured at about 470-870 m, 1000-1620 m, and 1000-1520 m for 09:00 CST, 10:00 CST and 11:00 CST respectively.

Figure 2.11 shows hourly aerosol backscatter profiles for September 15, 2013 and corresponding BLHs retrieved by the aerosol gradient, cluster and wavelet methods. Both aerosol gradient and wavelet methods consistently identify the BLH as the top of the cloud layer due to the large negative gradient created by strong cloud signals. This is

often the height of the thermodynamic BL identified using relative humidity and dew point temperature methods, which find the height of the ML as the sharp decrease in moisture at the top of the cloud layer. Low cloud layers however impede the detection of the above BLH therefore the aerosol gradient and wavelet method will mistakenly identify the large gradient of the low cloud layers as the BLH, while the cluster method will identify the BL as the base of the low cloud layer. The aerosol gradient method typically found the BLH at the beginning of the large negative gradient (top of the cloud layer) while the wavelet method calculated the BLH slightly higher than the aerosol gradient method. Differences between these two methods were found to not exceed 200 m and could be attributed to the different averaging settings applied for these methods.

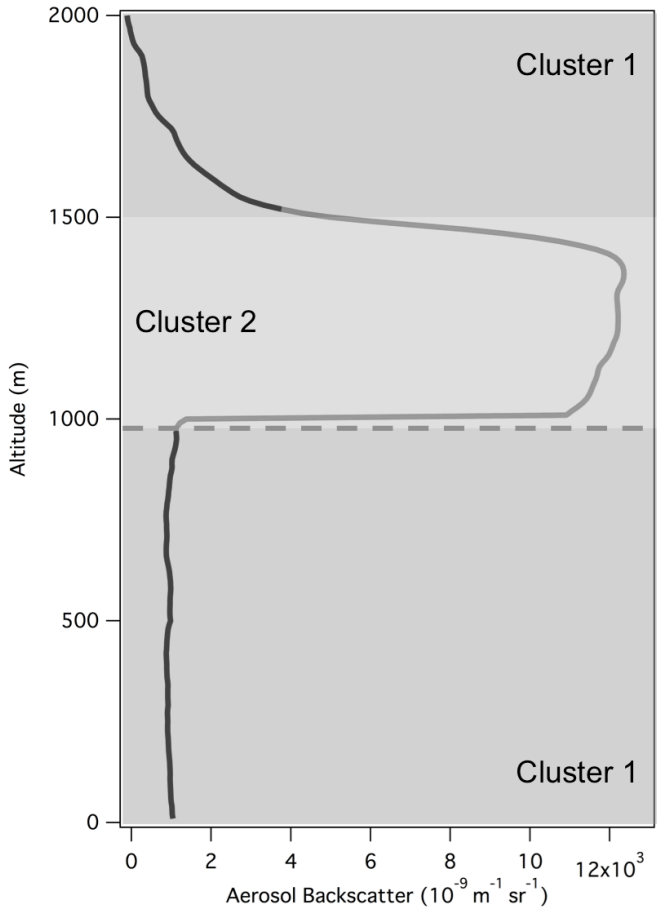

Figure 2.12. Cluster assignments of aerosol backscatter profile with cloud layer at about 1000-1520 m on September 15, 2013 measured at 11:00 CST. Automated BLH was found at 970 m.

The cluster method was found to constantly identify the cloud base as the BLH by assigning aerosol signals into a cluster of cloud signals and a second cluster of cloud-free signals with the first transition (BLH) of these clusters located at the base of the cloud layer (Fig. 2.12) at 970 m. A second transition of clusters is located at the top of the cloud layer (about 1400 m) corresponding to the BLHs retrieved by the aerosol gradient and wavelet methods. The cluster method then essentially calculates the cloud layer depth by assigning a cluster solely to the cloud layer.

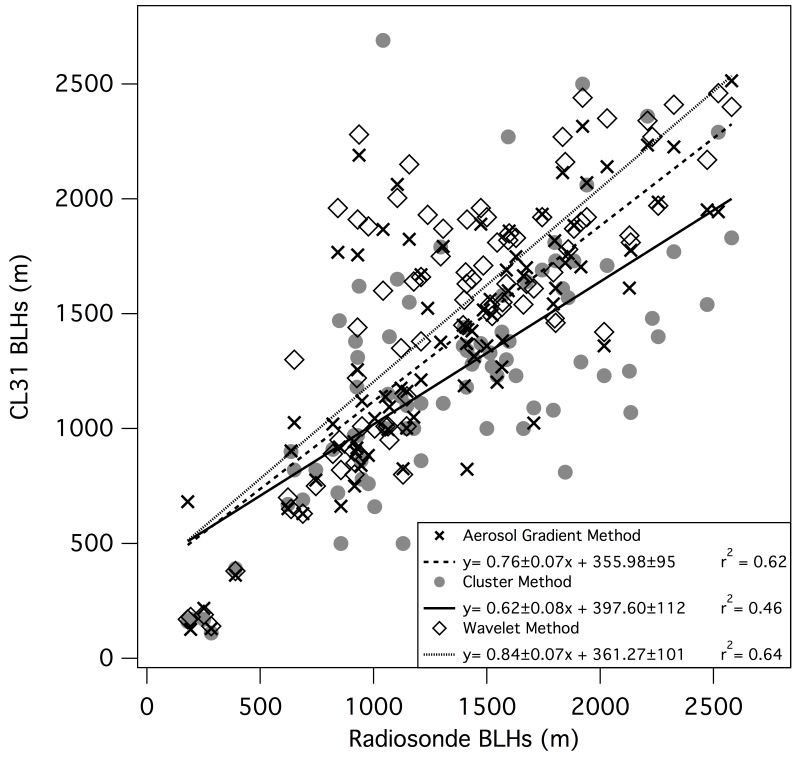

Figure 2.13. Comparison of CL31 aerosol backscatter BLHs and radiosonde derived BLHs including cloud signals. The linear regression lines, regression line equations, and correlation coefficients r^2 are listed for each BLH retrieval method comparison.

The effect of clouds in the overall correlation between aerosol backscatter methods and radiosonde BLHs in both cloud and cloud-free profiles is seen in Figure 2.13. During a fully developed convective cloud topped ML, the aerosol gradient methods agree reasonably well with the radiosonde derived BLHs. However, under less developed MLs the agreement decreases due to the aerosol gradient methods identifying the BLH at the top of a cloud layer while the skew-*T log-P* method finds the BL at a strong inversion lower than the cloud layer. This effect can be seen in the radiosonde BLH range of about 800 m) to 1500 m in Figure 2.13. The cluster analysis method

showed the highest decrease in correlation due to the detection of the cloud base as the BLH significantly underestimating the BLH.

The presence of clouds creates difficulties in the detection of the BLH for all methods due to the extinction of aerosol backscatter signals above the cloud, the presence of low clouds mistakenly identified as the BLH, or the detection of high cloud signals above the skew-*T log-P* derived BLH. Hence the removal of profiles with cloud signals is preferred for the automatic retrieval of the BLH. This affects the cluster and aerosol gradient methods in particular since the moving time averaging performed before the application of the algorithms will expand cloud signals to a greater number of profiles subsequently eliminating these profiles for BLH detection.

2.5 Summary and Conclusions

Aerosol backscatter-derived boundary-layer heights from three distinct methods were tested and compared to radiosonde retrieved BLHs. An aerosol gradient method, a cluster analysis method, and a Haar wavelet method were compared to daytime radiosonde profiles using measured aerosol backscatter from a Vaisala CL31 ceilometer. This comparison used 47 radiosondes for the aerosol gradient method, 45 for the cluster analysis method, and 48 for the Haar wavelet method due to limitations implicit to each algorithm (see Results Section 2.4). The first method, the Vaisala Corp. aerosol gradient method finds the three largest gradients in an aerosol backscatter profile, one of which must be chosen as the height of the boundary layer. The second method, a cluster analysis method calculates variance in an aerosol backscatter profile with the BLH correlating to a peak in variance. K-means cluster analysis then divides a

variance profile at the height of the BL (variance peak). The final method uses a Covariance Wavelet Transform utilizing the Haar wavelet compound step function to identify a sharp aerosol backscatter gradient corresponding to the top of the BL by calculating the wavelet transform at various dilations. The results presented here used daytime measurements only, however the findings can be applied to similar signals as those found in the nighttime residual and nocturnal stable layers.

Overall good agreement was found for all methods with no statistically significant bias found. Yet all methods found cases where thermodynamic BLHs from radiosondes did not correlate with a maximum gradient in aerosol backscatter due to differences in thermodynamic and aerosol BLHs and the methodology used to derive these heights. The comparison between the aerosol gradient method and radiosonde derived BLHs showed difficulties in determining the BLH in low aerosol backscatter conditions. The calculation of the three largest gradients particular to this method was useful in situations where the largest gradient does not correlate with the radiosonde derived BLH. Yet this requires a priori knowledge of typical boundary layer heights and evolution in the location of interest. In contrast, the cluster method showed drawbacks due to sensitivity to noise generated artifacts or lofted aerosol layers where the algorithm mistakenly found peaks in variance and incorrectly identified them as the BLH. Profiles were also mistakenly divided due to the increasing noise with height rather than a peak in variance, underestimating the height of the BL. With this automated cluster analysis method, a previous knowledge of the BL aids in identifying such algorithm errors, but is otherwise not necessary. Further work is needed to improve the cluster method sensitivity to noise and should be kept in mind when using

the cluster method or other variance-based algorithms for BLH detection. All methods are able to resolve for BLHs under stable and unstable conditions after manual selection of the calculated aerosol backscatter gradients reported by the aerosol gradient method, and an addition of a height limit of 500 m for nighttime hours applied to both the wavelet and cluster methods. The cluster method showed the most variability due to the incorrect identification of lofted aerosol layer signals as the BLH, while the aerosol gradient method and the wavelet method BLHs showed very similar results for the tested time period.

Overall, the wavelet method showed the best agreement of all methods tested here, with 77.5% of cases showing excellent agreement with radiosonde BLHs without previous knowledge of the BL required, as this method is also automated. The cases where deviations occurred (~ 22.5% of all observations) were due to multiple sharp gradients corresponding to lofted aerosol layers and to the thermodynamically derived BLH not corresponding to the greatest gradient in an aerosol profile (Fig. 2.10). A bias of 51.1 m was found indicating that wavelet method BLHs are generally higher than radiosonde derived BLHs. This disparity has been previously attributed to aerosol penetrating into the stable layer above the BLH leading to the overestimation of aerosol derived BLHs (McElroy and Smith, 1991; Seibert et al., 2000). The wavelet method also showed a higher ability of calculating the BLH under low aerosol conditions.

The effect of cloud signals in the determination of the BLH showed a clear difference between the negative gradient methods (aerosol backscatter and wavelet methods) and the cluster analysis method. Both aerosol gradient and wavelet methods identify the BLH as the top of the cloud layer where a sharp negative gradient created

by strong cloud signals was found, while the cluster method identified the BLH as the base of the cloud layer. The cluster method was found to assign a cluster for cloud signal and a cluster for cloud-free signal along an aerosol backscatter profile (Fig. 2.12). The automatic detection of the first transition of clusters identifies the BLH as the base of the cloud layer with the second transition at the top of the cloud layer, i.e. it identifies the cloud layer depth. Limited detection of the BLH in aerosol profiles with cloud signals is seen for all methods (Fig. 2.13) with the cluster and aerosol gradient methods being more sensitive due to the moving time averaging applied expanding cloud signals to a greater number of profiles, consequently eliminating these profiles for BLH detection. Both the wavelet and aerosol aerosol gradient methods agree reasonably well with the radiosonde derived BLHs in a fully developed convective cloud topped ML. Agreement decreases when the aerosol gradient and wavelet methods identify the BLH at the top of a cloud layer while the skew-*T log-P* BLHs are calculated at a height lower than the cloud layer under less developed MLs.

The results presented here demonstrate the ability of the Haar Wavelet method to more accurately detect BLHs than the aerosol gradient and cluster methods while requiring the least amount of manual inspection. The errors found with this method were due to lofted aerosol layers, low-level clouds and differences in determining BLHs using aerosols and thermodynamically using radiosondes. In order to use this method on other instruments and locations, dilation values should be determined carefully and individually. Out of the three methods tested in this study, it is suggested to employ the wavelet method in future studies, in particular for long-term seasonal and diurnal boundary layer studies and spatial analysis of the BL using multiple LIDAR aerosol

backscatter measurements. Spatial analysis of the BL can also be done by combining multiple LIDAR aerosol backscatter measurements using the wavelet and cluster analysis methods. These methods were seen to perform well using various LIDAR instruments in studies such as Compton et al. (2013), Scarino et al. (2014), and Toledo et al. (2014). A combination of the wavelet method BLH retrievals during clear skies and the cluster analysis method's ability to calculate cloud depth is also recommended for more robust BL studies to retrieve more information about the boundary layer under both conditions. Although not tested in this study, de Bruine et al. (2016) shows promising results using an automated method which prevents incorrect detection of the BLH using graph theory.

3 Coastal boundary-layer heights and evolution using long-term ceilometer aerosol backscatter data

3.1 Introduction

Understanding the behavior and dynamics of the boundary layer and its impact on the dispersion and distribution of air pollutants is vital for air quality studies. Influences from surface forcings such as evaporation and transpiration, heat transfer, frictional drag, and terrain-produced air flows can change the stability of the BL and the BLH. A coastal BL introduces complexities and dynamics that require further detailed characterization. For instance, the sea-breeze circulation and the stratification of the marine BL and their impact over a coastal BL need to be accounted for in order to successfully implement air quality and weather forecast models in complex coastal regions. Various studies have attempted to measure and assess the ability of models to predict the dispersion of aerosols and air pollutants and the evolution of a coastal BL. However these models are not typically able to simulate complex coastal boundary layers (Floor et al., 2013; Peña et al., 2013; Calmet and Mestayer, 2016). In particular, the stratification of the coastal BL leading to internal layers such as the thermal internal boundary layer (TIBL) or intrusive marine layers further increase the difficulty in understanding the dispersion and distribution of air pollutants.

More recent studies use remote sensing instruments in particular high spatial resolution wind profilers (Feudo et al., 2010; Peña et al., 2013; Floors et al., 2013; Peña et al., 2014) that have allowed for the study of coastal atmospheric environments increasing our knowledge of a typical coastal boundary-layer evolution. In particular,

the TIBL has been studied as an important characteristic of costal boundary layers directly associated with the sea-breeze circulation. A TIBL is created when cool onshore wind is heated over a continental surface creating an internal boundary layer within the developing coastal mixed layer (Garratt, 1990). McElroy and Smith (1991) used an airborne LIDAR to investigate the TIBL in the coastal environment in southern California. The airborne LIDAR was able to document the TIBL and characterize the boundary between a marine layer and a continental convective layer as having a "mini-cold front" effect about 10 km inland. Parameswaran (2001), Talbot et al. (2007), and Tomasi et al. (2007) also illustrate the evolution of internal boundary layers related to the sea-breeze circulation and its impact on the advection of both sea salt and land surface aerosols. The TIBL was found to deliver sea aerosols inland while significantly hindering the penetration of aerosols to altitudes above the TIBL (below ~400 m above ground level [agl]) making it an essential part in the distribution of BL aerosols in coastal areas.

McElroy and Smith (1991) and Tomasi et al. (2011) among others report sea-breeze episodes and detail the typical heights of the TIBL between 100-300 m agl and detected up to 5 km inland from the sea shore. Further studies have then used observations to evaluate the ability of weather models to reproduce a complex stratified coastal boundary layer such as those studies done by Floors et al. (2013), Draxl et al. (2014), Calmet and Mestayer (2016) and Salvador at al. (2016).

The goal of this study is to characterize the evolution of a coastal boundary layer using continuous aerosol backscatter measurements from a ceilometer located on Galveston Island, Texas. A BLH climatology is established based on separating the data

into four scenarios of similar BLHs and BL evolution and are analyzed with accompanying surface wind measurements and HYSPLIT backward trajectories. A case study is performed using radiosonde launches at the Galveston site to further discuss and describe the coastal BL characteristics and evolution.

3.2. Data Set

The data used in this study is based on continuous aerosol backscatter measurements from September 1, 2013 to September 30, 2016 retrieved by a Vaisala CL31 ceilometer located at the TCEQ CAMS (Texas Commission of Environmental Quality Continuous Ambient Monitoring Station) C1034 Galveston 99th site described below. Meteorological data from this CAMS site was available throughout the entire study period as well as albeit a limited number of radiosonde launches. Launches were only performed at the site on a case study day in October 2016. Supportive data includes aircraft vertical profiles from the NASA P3-B aircraft and HSRL (High Spectral Resolution LIDAR) aboard the NASA King Air B200 measured during the September 2013 NASA DISCOVER-AQ (Deriving Information on Surface conditions from Column and Vertically Resolved Observations Relevant to Air Quality) Texas Campaign.

The study site is located in at the TCEQ C1034 CAMS site on Galveston Island, Texas (Figure 3.1) at an elevation of about 5 m agl. The site has its closest Gulf of Mexico shore about 0.9 km south and the closest Galveston Bay shore about 2.8 km north. The east and western shores are about 1.4 km and 6 km away from the measurement site, respectively.

The sea-breeze circulation will impact this site typically from the E and SE direction and land breeze flow is expected from the W and NW direction as also described by Darby (2005), and Banta et al. (2005). The sea-breeze circulation arises from the difference in temperatures over land and water. After sunrise, air over land will warm faster than air over water. This warm air over land will eventually rise and allow cooler surface onshore air from the E and SE to move inland while a warmer offshore return flow typically from the W and NW can be experienced above. The difference in air temperature also creates the land breeze during nighttime hours when the air over land cools down quicker than the air over water. The rising warmer air allows for the cool land breeze air to move in replacing the warm air typically from the N and NW directions.

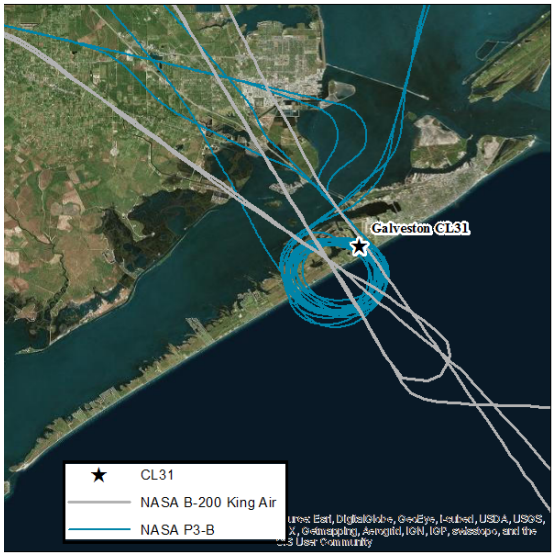

Figure 3.1. Flight tracks for the NASA B200 King Air and P3-B aircraft above the CL31 measurement site during DISCOVER-AQ on September 25, 2013.

3.2.1. Vaisala CL31

The Vaisala CL31 ceilometer operates at a wavelength of 905 nanometers (nm) using an indium gallium arsenide laser diode (InGasAs) system with a 1.2 microjoule (mJ) pulse for 110 nanoseconds (ns) and mean pulse repetition rate of 8192 Hertz (Hz). It uses a single lens design to both transmit and receive light signals. This design reduces the optical crosstalk between transmitter and receiver and in turn increases the signal-to-noise ratio. A beam splitter gives full overlap of the transmitter and receiver field-of-view at an altitude of 70 m (Münkel et al., 2007).

The aerosol backscatter coefficient $\beta(x,\lambda)$ or the scattering cross section per unit volume is related to the received power with the following formula:

$$P(x,\lambda) = \frac{c}{2x^2} \; P_0 \, A\eta O(x)\Delta t \; \times \; \beta(x,\lambda)\tau^2(x,\lambda) \qquad (3.1)$$

where P is the optical power received by the ceilometer from distance x, c is the speed of light, Δt is the pulse duration, P_0 is the average laser power during pulse, A is the area of receiver optics, η is the receiver optics' efficiency, $O(x)$ is the range dependent overlap integral between transmitted beam and received, $\tau(x,\lambda)$ is the transmittance of the atmosphere between LIDAR and volume, λ is the wavelength of the emitted laser pulse, x is the distance between LIDAR and scattering volume and B is the sum of electronic and optical background noise (Weitkamp, 2005). Aerosol backscatter profiles with signals from clouds, rain, or fog are identified as signals higher than $2000\times10^{-9}\mathrm{m}^{-1}\mathrm{sr}^{-1}$ and were not used for this BLH comparison (Münkel et al., 2007; Vaisala Oyj, 2011). The CL31 can measure aerosol backscatter up to 7500 m. However, the CL31 does not record these signals, but instead only accumulates aerosol

backscatter intensity every 16 seconds with a maximum height of 4500 m and 10 m resolution. The CL31 ran with firmware v1.7 and noise_h2 on. For more in depth information about the instrument see Münkel et al. (2007).

A total of 1126 days of aerosol backscatter data are analyzed in this study. Communication problems between the ceilometer and the logging computer were removed (78 days) resulting in a total of 1047 days of aerosol backscatter data. Data from May 19, 2016 through September 30, 2016 were measured by a replacement CL31 ceilometer due to water damage of the original Galveston CL31. From September 2016 – January 2017 both ceilometers measured side-by-side at the Galveston site in order to evaluate the consistency of the BLH time series calculated by both ceilometers. Section 3.4 presents the results of the comparisons and validation methods used.

3.2.2. TCEQ CAMS site

Wind speed and wind direction data from the TCEQ CAMS C1034 is used in this study. Wind speed and wind direction are used to characterize aerosol backscatter BLH results and define wind patterns associated with various aerosol derived BLH schemes.

3.2.3. Supporting Data

iMet Radiosondes

International Met Systems Incorporated model iMet-1 radiosondes were launched at the ceilometer site on October 9, 2016 at 06:53, 08:36, and 10:21 CST. iMet-1 radiosondes return GPS (Global Positioning System) location, GPS altitude,

wind speed and direction, pressure, temperature, and relative humidity with a 1 Hz sampling rate using a 403 MHz transmitter. Radiosondes used here have a resolution of 0.01hPa, a response time of 1s, and an accuracy of 0.5h Pa for pressure measurements. Temperature sensing has a resolution of 0.01 °C, an accuracy of 0.2 °C, and a response time of 2 s. The humidity sensors for the radiosondes have a resolution of less than 0.1%, an accuracy of 5%, and a response time of 2 s. Average ascent rate for all launches was about 4 m/s.

P3-B Meteorological data

The NASA P-3B aircraft spiraled over the Galveston site typically three times a day for a total of 9 days during the NASA DISCOVER-AQ campaign in September 2013 (sample flight track is shown in Figure 3.1). Spirals usually occurred at 9:00, 12:00 and 14:00 CST with a maximum distance of 5 km from the Galveston CL31 and a vertical altitude from about 9 m agl during missed approaches at the Galveston airport adjacent to the CL31 site and up to about 4000 m agl. Here, we will use the P-3B vertical profiles of dewpoint temperature, potential temperature, and relative humidity. Flight tracks of the NASA P-3B for September 25 are shown in Figure 3.1 (all spirals followed similar trajectories). No wind speed or wind direction measurements are available during aircraft spirals.

NASA HSRL (High Spectral Resolution LIDAR)

The HSRL aboard the NASA B200 aircraft measures aerosol extinction at 532 nm, backscatter at 532 nm and 1064 nm, depolarization at 532 nm and 1064 nm and aerosol optical depth (AOD) at 532 nm.

NASA derived BLHs are based on 532 nm profiles and a Haar wavelet algorithm, which is similar to the approach we apply for the Vaisala CL31 data described in Section 3.3.2. Therefore, this study uses the 532 nm aerosol backscatter profiles from the HSRL to compare to BLHs derived from the CL31. An example of a flight track during the NASA DISCOVER-AQ campaign is shown in Figure 3.1. The 532nm aerosol backscatter measurements are averaged over ~1000 m horizontal and 30 m vertical resolution with a 15 m sampling interval computed every 0.5 s using a 10 s running average (Hair et al., 2008). The NASA B200 aircraft measured over the Galveston Island 4-8 times on each measurement day, typically at about 8:00, 9:00, 13:00, 14:00 and 15:00 CST for 10 days during the NASA DISCOVER-AQ Texas 2013 campaign. The HSRL typically measured 4-5 profiles every overpass of Galveston Island; here we use 103 profiles none of which exceed a 8 km distance from the CL31 site while still remaining directly over Galveston Island (no measurements over water).

3.3. Methods

3.3.1. Skew *T Log-P*

A stable BL is characterized by having an environmental lapse rate greater than a moist/dry adiabatic lapse rate, while an unstable boundary layer is identified by

having a dry adiabatic lapse rate greater than the environmental lapse rate. Stable profiles BLHs are identified as the top of the shallow stable layer seen as a strong positive vertical gradient change in temperature and a strong negative gradient in dew point temperature profiles. BLHs during unstable conditions are identified as the base of the stable EZ (i.e., temperature inversion) where the temperature profile intersects dry adiabates and/or where relative humidity or dew point temperature profiles sharply decrease (Stull, 1988; Kovaled and Eichinger, 2004 and Haman et al., 2012). A previous study by Haman et al. (2012) found a correlation coefficient of 0.96 during unstable conditions and 0.91 during stable conditions when comparing ceilometer and radiosonde derived BLHs (both manually) using the skew-*T log-P* method.

3.3.2. Haar Wavelet Method

Aerosol derived BLH methods presented here are based on two assumptions: 1) the BL contains somewhat constant concentrations of aerosols due to convective and turbulent mixing and 2) the clean FT above will create a negative gradient in aerosol backscatter from higher concentrations within the BL towards lower concentrations in the FT. The local maximum of this gradient is identified as the top of the BL (Steyn et al., 1999)

Aerosol backscatter BLHs are derived with a Covariance Wavelet Transform utilizing the Haar wavelet compound step function with multiple user defined wavelet dilations (Cohn and Angevine, 2000; Davis et al., 2000; Brooks et al., 2003; Baars et al., 2008; Compton et al., 2013; Uzan et al., 2016). This method identifies the sharp

aerosol backscatter gradient corresponding to the top of the BL by calculating the wavelet transform. The Haar wavelet function *h* is defined as follows:

$$h\left(\frac{z-b}{a}\right) = \begin{Bmatrix} -1: b-\frac{a}{2} \le z < b \\ +1: b \le z \le b+\frac{a}{2} \\ 0: \text{elsewhere} \end{Bmatrix}, \quad (3.2)$$

where z is the vertical altitude in this application, a is the vertical extent or dilation of the Haar function, and b is the center of the Haar wavelet function. The covariance transform of the Haar wavelet function, w_f is defined as:

$$w_f(a,b) = a^{-1}\int_{z_b}^{z_t} f(z)h\left(\frac{z-b}{a}\right)dz\,, \quad (3.3)$$

where z_t and z_b are the top and bottom altitudes in the aerosol backscatter profile, $f(z)$ is the aerosol backscatter profile as a function of altitude, and a is the normalization factor or the inverse of the dilation, respectively.

Defining the dilation factors a and the range of centers of b of the Haar wavelet function are key in correctly identifying the BLH using aerosol backscatter profiles. In this study, b ranges from the lowest acceptable ceilometer recorded aerosol backscatter altitude of 100 m to a maximum BLH of 1300 m.

As with previous studies (Brooks, 2003; Baars et al., 2008; Compton et al., 2013; Scarino et al., 2014) the dilation factor a affects the number of covariance wavelet transform coefficients (CWTC) local minimums. Larger values create large local minimums at the heights of the biggest aerosol gradients in the aerosol backscatter profile. Lower dilation values create numerous CWTC local minimums at heights of smaller aerosol gradients in the measured profiles. A range of dilation values is applied to the aerosol backscatter profile. Here we use a maximum dilation of 30 m for

nighttime BLHs since the nocturnal stable layer (NSL) tends to have a smaller aerosol backscatter gradient than the above residual layer (RL) creating a need for more than one local minimum (not shown). In these cases, the CWTC local minimum closest to the surface is chosen as the BL. A higher limit of 100 m for the dilation factor *a* is applied for daytime BLHs and the strongest CWTC local minimum is used to identify the sharp transition between ML and FT. This larger dilation value also serves to decrease signals from smaller aerosol gradients below the BLH.

Aerosol backscatter signals below 100 m are removed due to an artificial peak in the ceilometer measured at the 40 m height most likely due to hardware related perturbations and CL31 software corrections in the Vaisala software (Kotthaus et al., 2016). Removing these signals prevent the incorrect calculation of the BLH due to strong gradients created by this artifact (Sokól et al., 2014; Kotthaus et al., 2016). Layers below 100 m are not detected by the Haar Wavelet Method due to the removal of the first 100 m in aerosol backscatter data. As a consequence this would also include the NSL as the removal of the first 100 m in aerosol backscatter might remove signals needed to calculate a lower NSL height.

Cloud-free CL31 aerosol backscatter profiles are averaged first vertically according to Table 3.1 followed by a 10-minute average before applying the Haar Wavelet algorithm. Here we use smaller vertical averaging (Table 3.1) than in Chapter 2 due to the lower BLHs expected in coastal environments. Too much averaging in lower altitude ranges will smooth gradients corresponding with possible coastal BLHs. Increasing noise with height requires higher spatial averaging in higher altitudes. However here, high averaging is not needed for BLH detections of lower BLHs in a

coastal environment. The algorithm is applied to each averaged profile with incremental dilations until the maximum dilation factor is reached (30 m for nighttime hours and 100 m for daytime hours). The Haar Wavelet algorithm also uses a height detection limit of 300 m limit during nighttime which is changed to 1300 m two hours after sunrise. The mean of all resulting CWT coefficients is then calculated and the local minimum of the mean CWT coefficients is identified as the BLH. Caicedo et al. (2016) compared BLH retrievals from radiosonde and CL31 aerosol backscatter data using three distinct BLH retrieval methods. The results presented in Caicedo et al. (2016) showed the Haar Wavelet method to be the most robust and having the best agreement between radiosonde and Haar Wavelet derived BLHs ($r^2 = 0.89$).

Table 3.1. Averaging heights used on aerosol backscatter profiles by height range.

Altitude Range	Averaging Height
10 – 490 m	110 m
500 – 990 m	190 m
1000 – 4500 m	230 m

The same method is used for HSRL mixing layer height (MLH) retrievals during daytime (note: there are no HSRL nighttime measurements). For this instrument we use a 10 m moving height average on each profile prior application of the code. The wavelet method is applied with a dilation factor *a* of 30 m and a *b* range from 0 m to 1300 m. The higher signal to noise ratio of this instrument requires less averaging and lower dilation values than those required for the ceilometers.

3.4. Data Validation

3.4.1. Instrument Intercomparison

A three-month side-by-side comparison (September 2016 – January 2017) at the Galveston site was performed between the repaired Galveston ceilometer and the replacement CL31 used for the data measured from May 2016 - September 2016. This comparison showed a slight difference in sensitivity of the lasers with the original Galveston CL31 having a more sensitive laser than the replacement CL31. The laser sensitivity and noise inherent to the ceilometers makes a raw aerosol backscatter comparison unreliable. In order to compare the two instruments we use two comparisons methods. The first uses the cloud base height calculated by both ceilometers by using a modified version of the Haar Wavelet method. The second comparison uses BLHs calculated using the Haar Wavelet method with more restrictive height limitations in order to verify a reoccurring layer measured at around 300 m – 600 m agl most often detected around 400 m agl.

The first comparison requires a modification to the Haar Wavelet algorithm to be applied to profiles containing cloud signals after a 10-minute temporal averaging and a vertical averaging according to Table 3.1 is applied. The same averaging was used for both ceilometers. However it must be noted that these settings were used for consistency and might not be the best application to the replacement CL31 due to possible differences in measurement sensitivities for each instrument. In order to detect a cloud base as an increase in aerosol backscatter signal we needed to modify the algorithm, in this case covariance transform of the Haar wavelet function. First, the

Haar wavelet function h is defined with Equation (3.2). Then the covariance transform of the Haar wavelet function, w_f, w_f is modified as:

$$w_f(a,b) = -a^{-1}\int_{z_b}^{z_t} f(z)h\left(\frac{z-b}{a}\right)dz \quad , \tag{3.4}$$

where z_t and z_b are the top and bottom altitudes in the backscatter profile $f(z)$ is the backscatter profile as a function of altitude, and a is the normalization factor or the negative inverse of the dilation, respectively. The negative inverse of the dilation modifies the algorithm to find the largest positive gradient created by high cloud signals. The dilation factor a is kept at the same value at 100 m and b ranges from 100 m to 1300 m. The results for hourly averages of the cloud base heights are shown in Table 3.2.

The second comparison uses the Haar Wavelet algorithm described in Section 3.3.2. The same vertical and temporal averaging was used for both ceilometers, however these settings were initially tested for the original Galveston CL31 only. As these settings may be instrument specific, they may introduce some bias to the results. These settings provided the best noise reduction without the removal of important gradients related to the BLH specific to the aerosol backscatter profiles measured by the original Galveston CL31. Daytime and nighttime a dilation values were kept consistent to those in Section 3.3.2 and b ranges were kept at 300 m agl for nighttime profiles while the daytime profiles were limited to a max range of 600 m agl. The 600 m agl limit was needed in order to verify the gradient present at the reoccurring ~300-600 m agl layer due to the difference in sensitivity of the lasers. Both ceilometers calculated a gradient at the height of interest but the intensity of the gradient differed between the

instruments. Therefore the 600 m agl limit forces the algorithm to look for the same gradient below 600 m agl. These settings were applied only to those days from September 2016 - January 2017 which showed a strong and consistent layer top measured at about 400 m agl in the original Galveston CL31. A total of 37 days met this requirement.

Table 3.2. CL31 Instrument Intercomparison. Correlation coefficients and linear regression lines (m) calculated from the cloud base height method and the wavelet method.

	Cloud Base Method	**Wavelet BLH Method**
r^2	0.91	0.97
Linear Regression	$y = 0.97\ (\pm\ 0.01)x + 32.26\ (\pm\ 9.85)$	$y = 1.11\ (\pm\ 0.01)x - 16.26\ (\pm\ 1.2)$

Both comparisons showed a fairly good correlation between the two instruments with uncertainties likely attributed to different averaging needed for the two instruments. Nonetheless, the estimation of the layer-top height at ~300-600 m agl by both ceilometers verifies the presence of this layer at the Galveston site.

3.4.2. Validation of measured aerosol layers

The complex stratification created by the mixing of marine air over the Galveston site creates difficulties in the retrieval of BLHs using aerosol backscatter profiles. Preliminary results using the Vaisala Corp. aerosol gradient method showed a nearly constant low layer with its top 100-200 m agl almost persistently in all data. This layer is not fully measured by the Haar Wavelet Method due to the removal of the first 100 m in aerosol backscatter data.

The Vaisala Corp. BL Matlab v3.7 algorithm finds negative gradients with increasing altitude in aerosol backscatter profiles. A 10-minute and 120-meter height averaging is applied to the profile along with a temperature dependence curve of -10 as recommended by Vaisala Corp. (C. Münkel, pers. comm., September 2013) due to the tendency of the CL31 having a curvature in aerosol backscatter profiles with increasing internal temperatures. The temperature correction of -10 is an algorithm setting that adjusts the shape and curve of temperature affected aerosol backscatter profiles with negligible effects on aerosol layer detection (Münkel at al., 2007; Vaisala Oyj, 2011). This study uses a minimum gradient height setting of 30 m along with a sensitivity setting of 15% which requires a 15% change in the relative aerosol backscatter in the vicinity of the possible BLH. The largest of the negative gradients is usually defined as the BL (Münkel at al., 2007; Vaisala Oyj, 2011).

The aerosol gradient method by Vaisala Corp. takes the artificial gradient into account and attempts to correct for it, therefore the calculation of this low layer should be valid (C. Münkel, pers. comm., September 2016). This layer was lower during the night at a minimum of about 50 m agl and had little growth during the daytime hours to its maximum height typically between 200-300 m agl. Figure 3.2 shows this layer as measured by the aerosol gradient algorithm during the month of September 2013. This low level layer is most likely a TIBL created by cool onshore wind flow heating up over the ground in the area of the site. As multiple studies have shown, the TIBL can be observed up to 5 km inland and can have a height up to 400 m agl consistent with the results seen with the aerosol gradient method. However, most studies report a gradual departure of this layer after sunset followed by the formation of the NSL (McElroy and

Smith, 1991; Parameswaran, 2001; Talbot et al., 2007; Tomasi et al., 2011; Floors et al., 2013). During nighttime hours the aerosol gradient method finds a gradient at a similar height as the TIBL however this layer most likely corresponds to the recently formed NSL. The RL is not shown in Figure 3.2, however it is measured by the aerosol gradient method as another aerosol gradient.

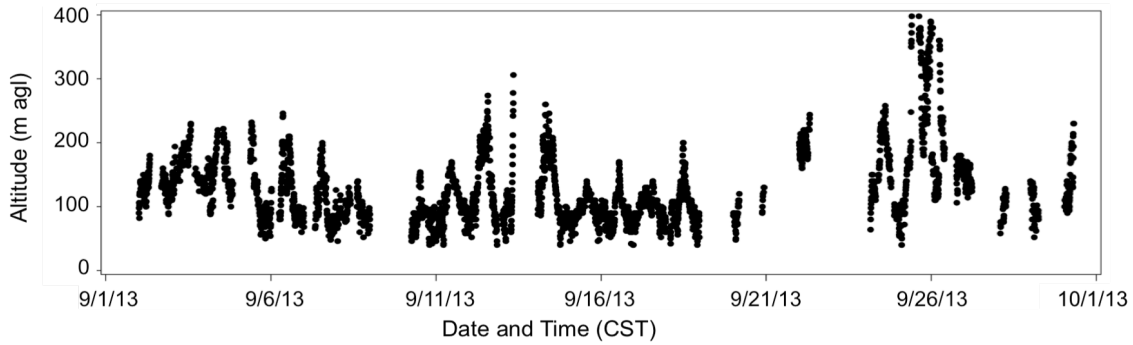

Figure 3.2. Time-series of the aerosol layer measured by the Vaisala aerosol gradient method during the month of September 2013.

An aerosol layer with a top ranging from about ~300-600 m agl was detected in 21.4% of the days observed in this study. This layer did not exhibit significant growth during the daytime hours. In order to rule out possible aerosol backscatter artifacts or measurement errors and to confirm the presence of such layers, additional BLH data from the NASA P3-B aircraft and the HSRL aboard the NASA B200 King Air during the DISCOVER-AQ campaign was used. Figure 3.3 shows the comparison of BLHs calculated using the methods described in Section 3.3. P3-B and HSRL BLHs measured directly over Galveston were compared to the ceilometer BLHs. The ceilometer BLHs used for the comparison were measured closest in time but not exceeding 10 minutes before or after a P3-B or HSRL measurement. Correlations show reasonable agreement between these BLHs and BLHs derived from the CL31 aerosol backscatter data.

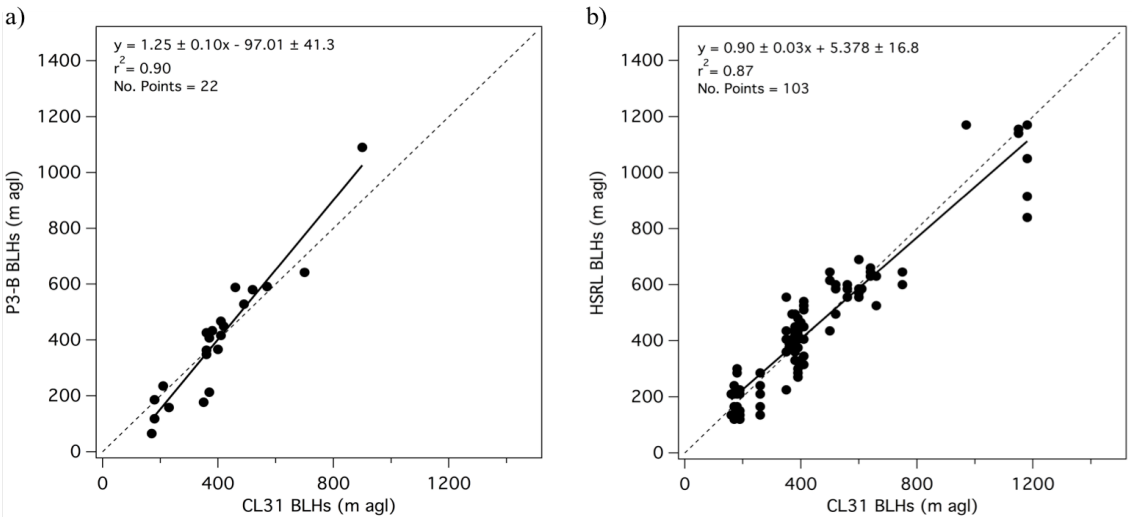

Figure 3.3. Comparison of CL31 aerosol backscatter BLHs and P3-B (a) and HSRL (b) derived BLHs. The CL31 BLHs using the Haar Wavelet method are compared to P3-B BLHs calculated using the skew-*T log-P* method and HSRL BLHs using the Haar Wavelet method. The linear regression lines, regression line equations, and correlation coefficients r^2 are listed for each BLH comparison.

To further examine the results in Figure 3.3 by verifying that the layers measured by the CL31 are simultaneously seen by both P3-B and HSRL measurements, Figures 3.4a - 3.44f illustrates profiles when both HSRL and P3-B measurements over the Galveston site were taken within 30-minutes. A corresponding CL31 profile measured within the same 30-minute window is displayed along with the aircraft profiles. This reduces a potential change in BLH in a time period longer than 30 minutes. We discuss these profiles in order to obtain the most comprehensive BLH data set retrieved by the three different platforms measuring the BL over Galveston.

Figures 3.4a - 3.4f show vertical profiles from the HSRL and CL31 averaged as stated in Section 3.2, while the P3-B profiles shown are smoothed using a binomial smoothing filter (for easier visual observation of the profiles, only; not used for analysis). BLHs are derived based on the Haar Wavelet method for the HSRL and CL31 data and the skew-*T log-P* method for the P3-B profiles. The resultant BLHs are

indicated as red dots along each corresponding profile in Figure 3.4. Figures 3.4a - 3.4e show an aerosol layer with its top between ~300-600 m agl measured by the three platforms. These days were associated with consistent SE and E winds below 7 m/s. In contrast, Figure 3.4f displays a higher MLH calculated by all methods. Both Figures 3.4e and 3.4f show measurements taken on September 25, 2013 at about 09:20 and 14:30 CST respectively - a high ozone day in the Houston-Galveston Area following a cold front passage on the preceding day. September 25, 2013 begins with NW winds reaching the Galveston site at low wind speeds below 2 m/s. Figure 3.4e is representative for these conditions at about 9:30 CST, when a ML has started to form in these air masses. Around 10:30 CST winds shift to the SE direction around along with a slightly increase in wind speeds yet not reaching wind speeds above 5 m/s. The higher MLH seen in Figure 3.4f (~700 m agl) than those in Figure 3.4a-4e, could be explained by the transport of air masses by NW winds. These air masses are expected to have a higher BLH than for instance marine air masses affecting the Galveston site due to increasing distance from ocean surfaces (Stull 1988; Garratt, 1992). Higher buoyancy and frictional drag inland from the coast will lead to more turbulence and stronger vertical mixing of air within the BL. Within these air parcels also aerosols will be transported to higher altitudes, carried to the study site and will ultimately be detected as the BL. The transported physical properties combined with clear skies conditions observed on September 25, 2013, which likely enhanced surface heat fluxes, could allow for aerosol mixing at higher altitudes resulting in the detected ~700 m agl BLH (Figure 3.4f). A weaker aerosol gradient at about 350 m is still detected in the CL31

profile, yet this layer no longer caps the majority of aerosols below it and is therefore not the greatest aerosol gradient identified as the BLH.

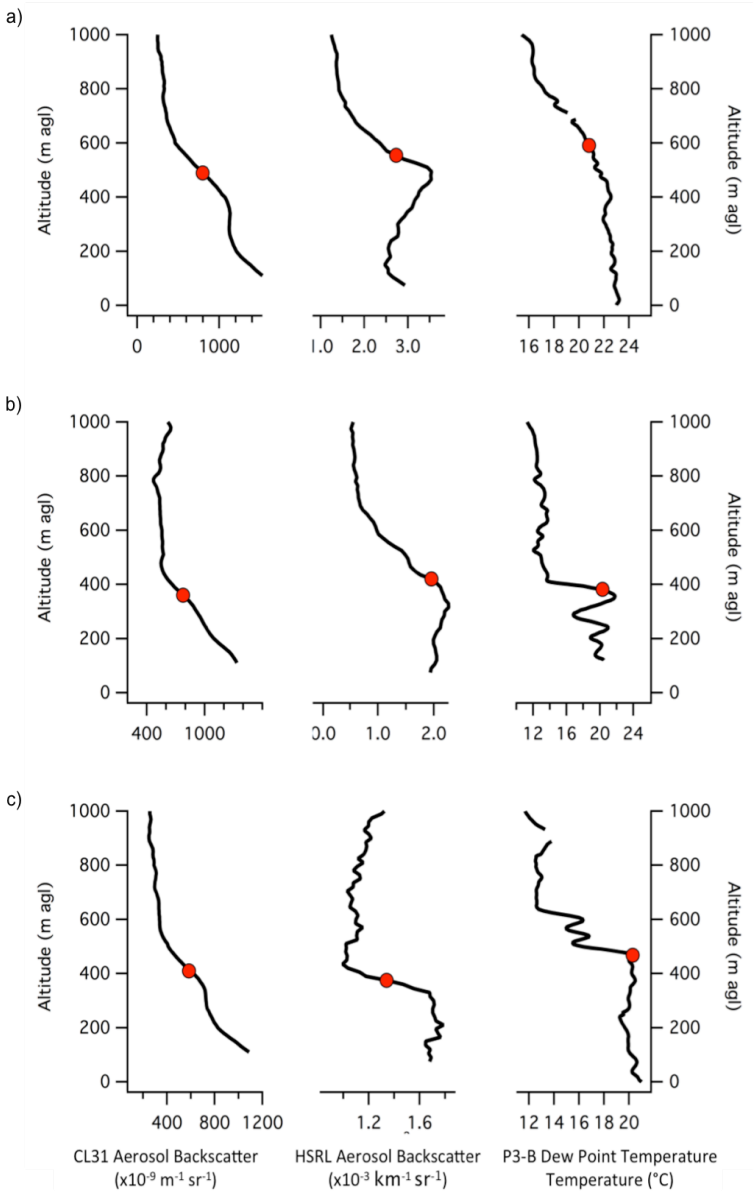

Figure 3.4. Vertical profiles measured (from left to right) by the CL31, HSRL and P3-B on (a) September 11, 2013 at about 14:30 CST, (b) September 12, 2013 at about 13:30 CST, (c) September 13, 2013 at about 14:20 CST, (d) September 14, 2013 at about 13:00 CST, (e) September 25, 2013 at about 9:20 CST, and (f) September 25, 2013 at about 14:30 CST. BLHs derived from each profile are indicated as red dots.

Figure 3.4, cont.

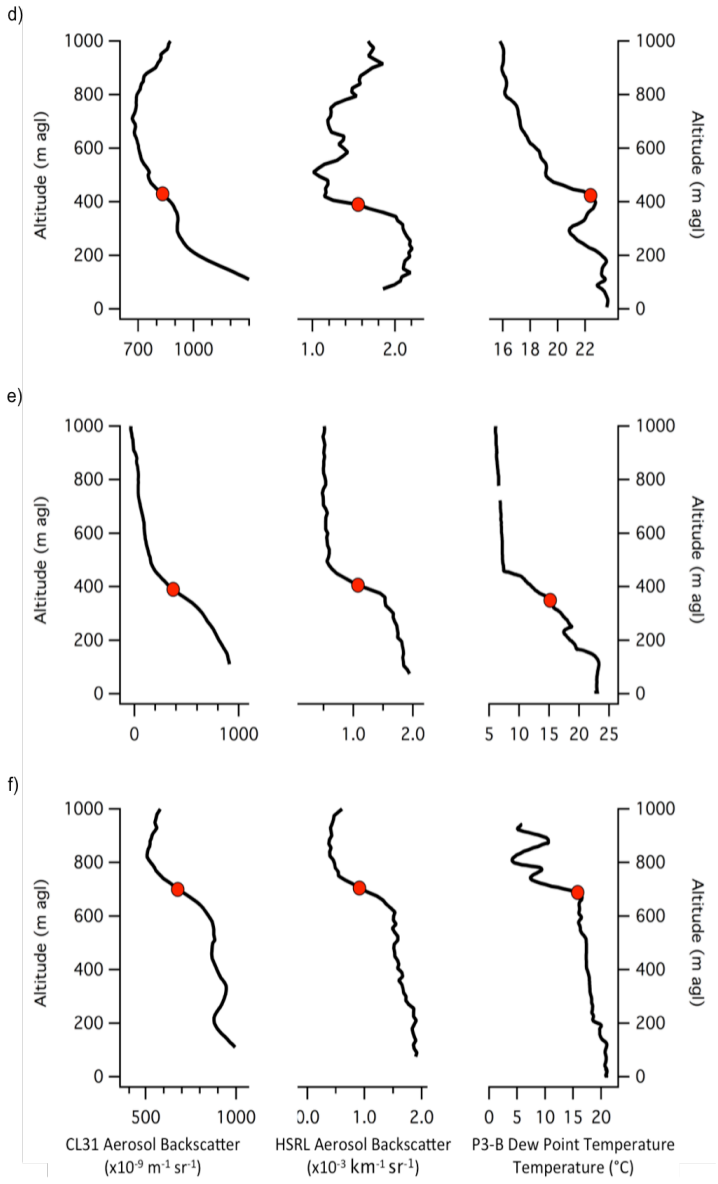

Radiosondes are still the standard comparison used to validate and evaluate remote sensing BLH retrieval techniques. Caicedo et al. (2016) compared over 40 daytime BLH retrievals from radiosonde and aerosol backscatter data using the replacement ceilometer used in this study. Caicedo et al. (2016) showed overall good agreement between radiosonde and aerosol derived boundary layer heights using the

same methods using in this study. On October 9, 2016, three radiosondes were launched at the Galveston site and allowed an additional evaluation of the CL31 BLHs at that site. These radionsondes were launched after a frontal passage on October 5, 2016 in order to maximize the probability of clear sky conditions and therefore limit the signals from clouds that might prevent the retrieval of aerosol backscatter BLHs. At this time, both the Galveston CL31 and the replacement CL31 were measuring at the Galveston site as part of their side-by-side comparison described before. Figure 3.5 shows the aerosol backscatter plots measured by the Galveston CL31 (Fig. 3.5a) and the replacement CL31 (Fig. 3.5b) along with the aerosol backscatter retrieved BLHs. The radiosonde estimated BLHs are plotted on each graph as a red-framed white triangle. The errors bars displayed correspond to the beginning and end of the negative gradient in the aerosol backscatter profile or the decrease in the dew point temperature profile in the radiosonde data, respectively. This decrease in both, the aerosol backscatter and the dewpoint temperature, corresponds to the EZ and therefore a BLH should fall within the depth of the EZ. Both, the CL31 and the radiosonde BLHs fall within this range.

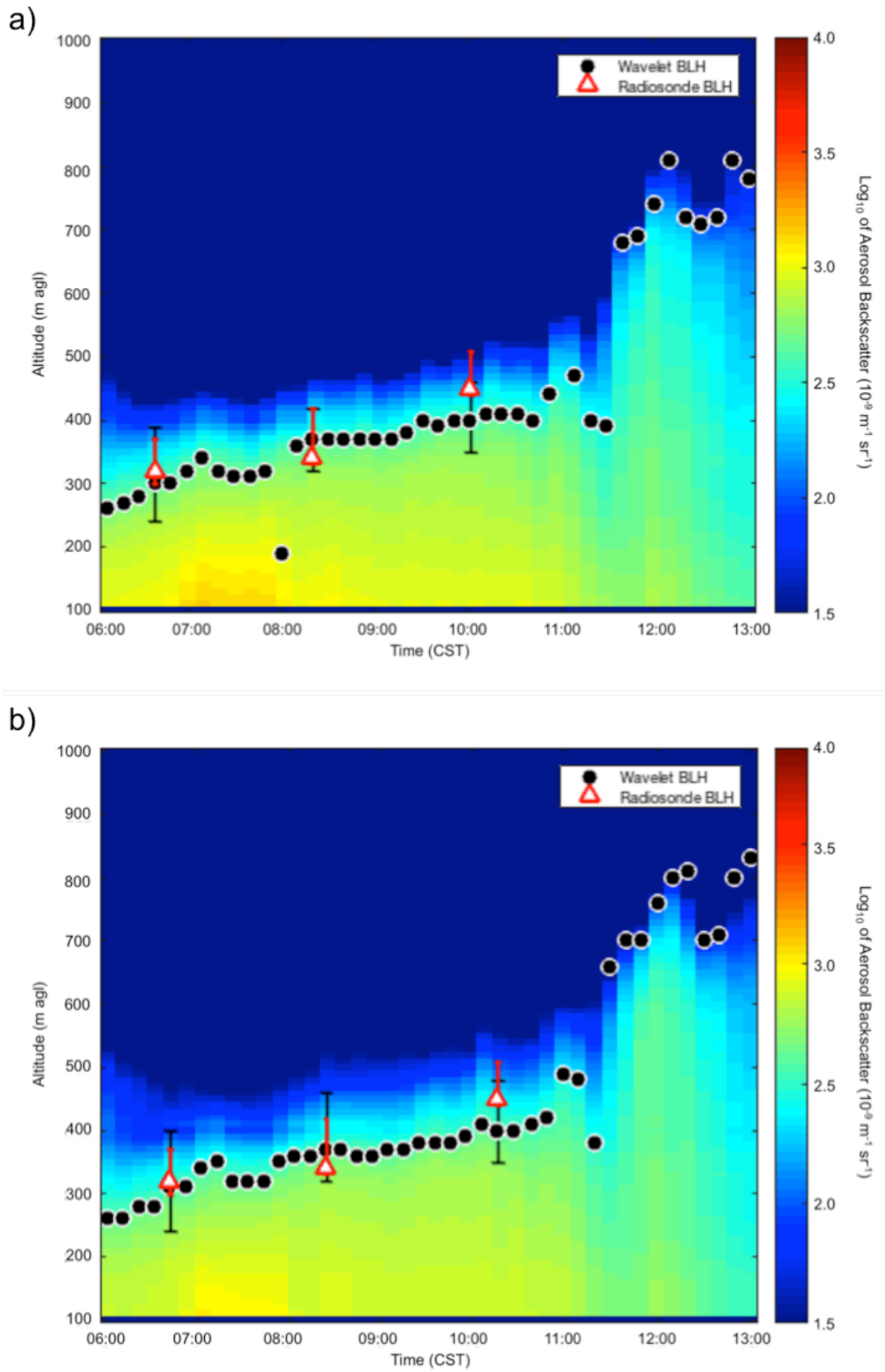

Figure 3.5. Aerosol backscatter plots from CL31 ceilometers for October 9, 2016. Radiosonde derived BLHs are shown as red triangles; (a) original Galveston ceilometer plots, (b) replacement ceilometer.

3.5. Results

3.5.1. BLH detection and limitations

The presence and the effects of the sea breeze, rain showers, fog, cloud cover, and the nearby marine boundary layer make this site a very complex area to study BLH variations and in turn highlights the limitations of BLH retrievals using aerosol backscatter (Fig. 3.6). The significant amount of unusable data due to frequent rain showers and cloud cover typical of a coastal site reduced the number of aerosol backscatter profiles valid for BLH retrievals to 608 days (45.7% of all 1126 study days). These findings are similar to those by Baars et al. (2008) at Leipzig, Germany for a period of one year. Days when rain signals prevented any identification of the BLH were about 19.7% of all the 1126 study days. Cloud signals that limited daily BLH detection accounted for 8% of the days. These days needed to be removed due to the extinction of aerosol backscatter signals above the cloud, the presence of low clouds mistakenly identified as the BLH, the distortion of aerosol backscatter below a cloud layer, or the incorrect detection of cloud signals at heights above the skew-*T log-P* derived BLH. The strong signals from cloud layers below 700 m agl impede the detection of gradients below the cloud layer of both the NSL and ML. Hence, these days were also removed from the analysis. Days where only NSL measurements were possible due to either rain or cloud signals contribute to about 17.7% of all the data set and are categorized as NSL only days (Figure 3.6). Figure 3.6 shows other occasions where BLHs derived from the wavelet method showed jumps between various aerosol layers. These conditions represent about 7.4% of days analyzed ("Other" category in

Figure 3.6). These days are particularly difficult for the identification of an individual MLH due to the jumps between the various aerosol layers. One potential reason for this behavior is that the aerosol layers measured in this scenario have similar aerosol backscatter gradients and the algorithm may not properly distinguish among different aerosol layers, as BLHs are measured at the top of different aerosol layers. Another likely source of these jumps are the settings used in this study. An adequate dilation factor and/or averaging settings that are successful on most retrieval days might not suffice in days categorized in the "Other" category creating the jumps between aerosol layers. A dilation factor a might be too low in some instances consequently creating multiple CWT coefficients at various altitudes which translates to jumps between retrieved BLHs. For this reason, these days are excluded from this climatological study.

The spring and winter seasons had the greatest number of days removed due to precipitation (31.9% and 29.2% of spring and winter data sets respectively), and summer had the highest number of cloudy days and consequently the most days removed due to cloud signals (16.3% of summer data set). The spring season had the least amount of data due to water damage and communication problems with the ceilometer resulting in about 19.2% of missing data.

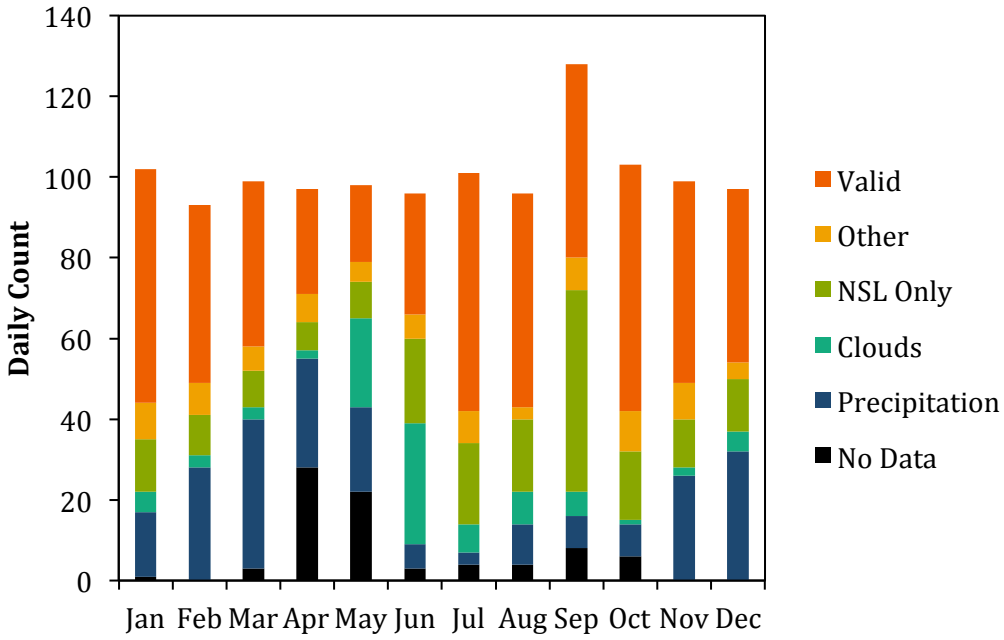

Figure 3.6. Total number of days of aerosol backscatter measurements during each month used in this study from September 2013 to September 2016 and corresponding number of days not used.

3.5.2. Characterization of Coastal Boundary-Layer stratification

The various aerosol layers measured by the previously discussed platforms demonstrate a stratification of the coastal boundary layer over Galveston Island and prevents the identification of a typical diurnal BL evolution of the NSL transition to ML and the decay of the ML to a NSL. This stratification creates difficulty in detecting the BLH using aerosol backscatter data; thus we divide the diurnal aerosol backscatter BLH results into four scenarios A, B, C, and D quantified in Figure 3.7 and illustrated in Figures 3.8a - 3.8d. Categories of CL31 results are additionally separated into the winter (December-February), spring (March-May), summer (June-August) and fall (September-November) seasons to establish a BLH climatology (Tables 3.3 and 3.4).

Wind surface measurements are used to describe scenarios and outline the wind patterns associated with each scenario. NW and N winds are indicative of local land air mass transport from the NW and N direction. As mentioned before, these air masses are expected to have higher BLHs with increasing distance from the coast due to higher buoyancy and shear related turbulence resulting in higher BLHs compared to those of a coastal site. These thermodynamic properties also allow for BL aerosol mixing at higher altitudes, which can then be transported to the Galveston site. In contrast, surface SE and E winds are associated with marine air from the Gulf of Mexico. Marine air masses are expected to have less buoyancy and shear-related turbulence than air masses over land due to (i) the heat capacity of water limiting the heat exchange between the surface and atmosphere and (ii) the low surface roughness of ocean surfaces. For this reason, lower BLHs are expected with SE and E winds. Air pollutants, in particular PM 2.5 (Particulate Matter with diameters larger than 2.5 micrometers), can also enhance the stability of the BL and decrease the BLH (Petäjä et al., 2016). However, due to the limited data set, this study cannot account for this specific effect of particulates on the BLH. Although the sea breeze can bring less-polluted air to the Galveston area, Banta et al. (2005) found that the land-sea breeze systems can actually carry ozone-polluted air inland and eventually back towards Galveston. The convergence of an offshore synoptic flow and the sea breeze create a period of stagnation that favors the accumulation of pollutants and lead to high ozone concentrations. The polluted air masses can then be carried offshore by a recirculation generated by rising warm air creating an offshore return flow aloft. In addition, a near surface return flow can also carry aged air masses offshore during nighttime hours with the onset of the land breeze. Both return flows

(lofted land recirculation or near surface land breeze) will have imbedded physical characteristics. Pollutants that are carried offshore and once over water, can interact differently with the water surface depending on their water solubility. Ozone for example, once carried over water will not be efficiently removed due to its low water solubility and can be carried back over land with the next day's onset of the sea breeze.

Hybrid Single-Particle Lagrangian Integrated Trajectory model (HYSPLIT) backward trajectories are used to identify the trajectory of air masses to the study site (Draxler and Rolph, 2003; Stein et al., 2015; Rolph, 2017). The meteorological input for the trajectory model was the NAM (North America Mesoscale) model with 12 km resolution. Backward trajectories were calculated for a 48-hour duration with level heights at 200 m, 600 m and 1000 m agl at 10:00 CST and 15:00 CST. Trajectories were run twice a day in order to detect possible changes in flow from morning times to afternoon times. The 10:00 CST and 15:00 CST times were chosen to identify air flow in the morning hours and afternoon hours before the collapse of the BL.

Backward trajectories identified as having originated and traveled over land for the majority (more than 30 hours) of their trajectory are considered to be bringing polluted air masses to the Galveston site and will be referred as continental trajectories, while backward trajectories originated and traveled over the Gulf of Mexico for the majority of their trajectory are considered to be delivering clean air to the study site and will be referred as marine trajectories. Both continental and marine air masses are not defined with a specific direction. Although continental (marine) trajectories are typically traveling from the N (SE) direction, instances, where trajectories arrive at the Galveston site from other directions are also seen. For instance, a 48-hour trajectory

identified as a continental trajectory might show air masses traveling from the N direction over the central US for the majority of trajectory (>36 hours), yet the last 12 hours show a small shift in direction resulting in the air mass arriving at Galveston from an E direction. For cases showing different trajectories at the three height levels calculated, the trajectories from the lowest 200 m level is used to define the model output.

Although backward trajectories are used to identify the transport of air masses to the Galveston site, the effect of local circulation cannot be overlooked. For example, a strong sea breeze will carry marine air to the study site replacing the continental air masses close to the surface. In these cases, the sea breeze will have a stronger influence of the BL evolution and height than the transported continental air mass. In rare cases, the spatial (12 km) and temporal (3 hour NAM Meteorological Input) resolutions of the HYSPLIT model input meteorological data could be insufficient to detect short-term local circulations that may be discernable in surface wind measurements.

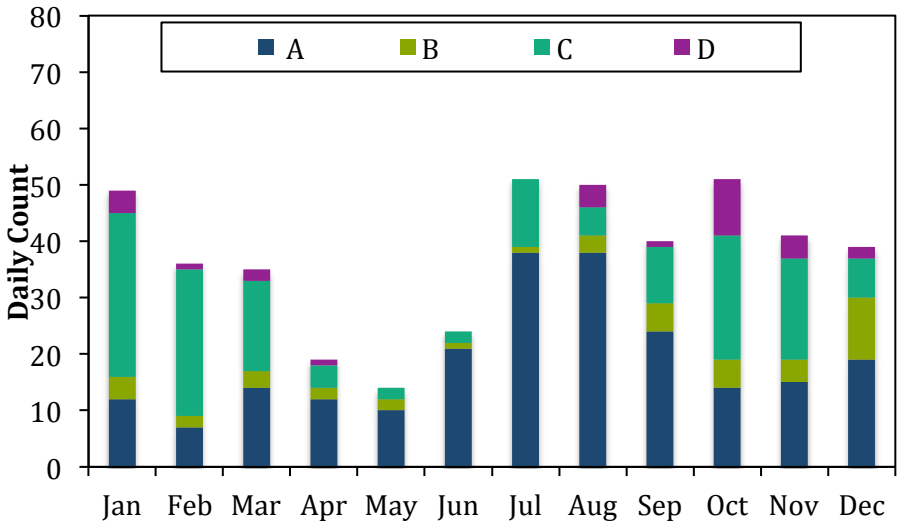

Figure 3.7. Daily count of BLH scenarios as described in the text. Data shown is based on 970 days which remained after the removal of days when BLH detection was not possible due to clouds, precipitation or missing data.

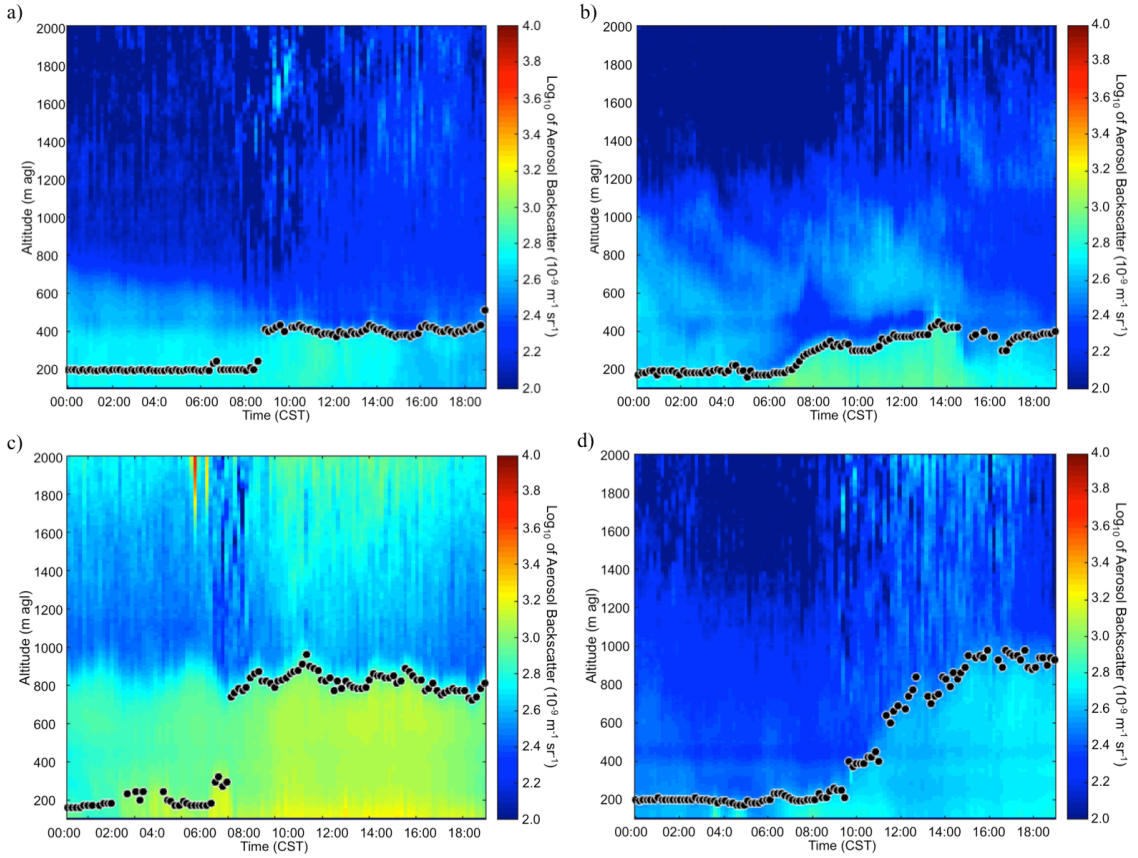

Figure 3.8. Aerosol backscatter plots depicting scenarios of aerosol layers over the Galveston site. Scenario A was measured on January 5, 2015 (a), scenario B on November 29, 2013 (b), scenario C on November 14, 2015 (c), and scenario D on March 13, 2014 (d).

Scenario A constitutes about 19.9% of days evaluated. It presents a NSL layer at about 200 m agl followed by a nearly constant aerosol layer, i.e., with no clear growth or connection between a NSL and the top of the layer (Figure 3.8a). This layer can have a height between 300-600 m agl depending on the specific day, but is at a nearly constant height after sunrise. The detection limits applied in the Haar Wavelet algorithm create a sudden jump between a NSL and the layer top measured at about ~300-600 m agl. This jump occurs when the height detection limit of the algorithm is raised to 1300 m two hours after sunrise allowing for the detection of aerosol gradients above 300 m. These days were associated with persistent sea breeze winds coming form the Gulf of Mexico, typically from the SE direction. However winds from the S and NE directions can also bring air from the Gulf of Mexico (see Fig. 3.1). The height of the ~300-600 m agl ML correlated to wind speeds. The higher the wind speed (typically higher than 7 m/s), the higher the ML.

BLHs calculated in this scenario do not present a gradual diurnal growth between a NSL and a ML but instead a MLH without substantial increase or decrease in height (Figure 3.8a). A season average of the results found in this scenario would show very little variability in daytime measurements. For this reason, we calculate the daily maximum in MLH seasonally. This same method is applied for scenario C which shows a diurnal evolution similar to scenario A. These are then averaged by season and are shown in Table 3.4. The summer months showed the highest average in peak BLHs detected in this scenario (about 612 ±114 m agl) and the winter months showed the lowest maximum BLHs at about 526 ±101 m agl.

For scenario A, HYSPLIT backward trajectories did not show one prevalent air mass trajectory but showed both continental US and Gulf of Mexico air masses reaching the study site. No differences in the BLHs between an identified continental or marine trajectory was seen. In these cases, local circulations might have some stronger impacts in the BLH than that of the air mass type. For instance, during a sea breeze circulation, the replacement of warm rising air by cooler surface onshore air can limit the BLH to lower altitudes (Parameswaran, 2001; Talbot et al., 2007; Feudo et al., 2010; Tomasi et al., 2011), while still having a continental air mass transport above the BL in the free troposphere. This is supported by the frequently observed SE winds and a BLH persistently reaching ~300-600 m agl indicating a close link to the marine BL of the Gulf of Mexico. Here, sea salt aerosols could form a substantial fraction of aerosol in this layer making this an easily distinguishable layer in the ceilometer signal.

Table 3.3. Categories of CL31 results in (%) of entire data set. Scenarios A-D are used for boundary layer height climatology.

	A	**B**	**C**	**D**	**Precipitation**	**Clouds**	**NSL Only**	**Missing Data**	**Other**
Winter	14.0	6.3	22.9	2.6	28.0	4.8	13.3	0.4	7.7
Spring	13.0	2.5	8.0	1.1	30.8	9.8	9.1	19.2	6.5
Summer	35.1	1.8	6.9	1.4	6.9	16.3	21.4	4.0	6.2
Fall	17.5	4.6	16.5	5.0	13.9	3.0	26.1	4.6	8.9
Average	19.9	3.8	13.6	2.6	19.7	8.3	17.7	7.0	7.4

Table 3.4. Seasonal averaged peak BLHs in [m agl] for scenarios A and C.

	A			**C**		
	Average Peak BLH	Standard Deviation	No. Days	Average Peak BLH	Standard Deviation	No. Days
Winter	526	101	38	996	155	62
Spring	536	123	36	1121	164	22
Summer	612	114	97	1006	103	19
Fall	567	128	53	1018	161	50

Scenario B is similar to scenario A, but shows a clear growth between the NSL and a ML with its top at about 400-600 m agl (3.8%) as shown in Figure 3.8b. This scenario is observed significantly less frequently than scenario A for the entire study period. Unlike scenario A, it is not often observed during the summer months from September 2013 through September 2016 while scenario A is most often observed in the summer months. This might be due to the presence of clouds during the summer months, particularly in the morning hours, where cloud signals might be preventing the detection of a connection between a NSL and a ML using aerosol backscatter signals. The growth from the NSL to the ML was correlated with a significant increase in wind speeds mixing aerosol to higher altitudes. Figure 3.9a shows hourly averaged wind speeds and CL31 calculated BLHs for all days in scenario B. A wind speed increase of a factor of 2.1 on average (ranging from 1.2 to 4.9) was seen in these days and correlates well with the morning time growth of the BLH at about the same time (Figure 3.9a). The wind speed increase during these days was found to be higher than those in scenario A, which showed a factor of 0.9 or less. The wind direction in this scenario was very similar to those in scenario A, i.e., SE winds coming onshore from the Gulf of Mexico. A wind shift from N to SE shortly after sunrise indicative of the sea breeze was identified on 15 out of the 23 days classified in this scenario. A few days were observed to have N winds and low wind speeds (less than 3 m/s) after rain events, yet no wind speed increase indicative of this scenario.

Scenario B backward trajectories all identified air masses traveling over the continental US reaching the Galveston site. Continental air masses are expected to result in higher BLHs than those with marine air masses, except for instances were a

strong local circulation is present. In this scenario, the predominant surface winds were measured from the SE direction and often associated with the sea breeze. Similar to scenario A, a strong sea breeze circulation can bring marine air to the study site and replace a continental air mass close to the surface. A sea breeze circulation can also maintain relatively low BLHs (compared to those measured in scenario D with predominant continental trajectories and N/NW winds). This suggests that a combination of 1) strong SE/E winds transporting marine air to Galveston and 2) a significant wind speed increase in the morning hours greater (by a factor of 1.2 – 4.9), might be key in the detection of a textbook BLH evolution from a NSL to the ML in general, regardless of the origin of air masses.

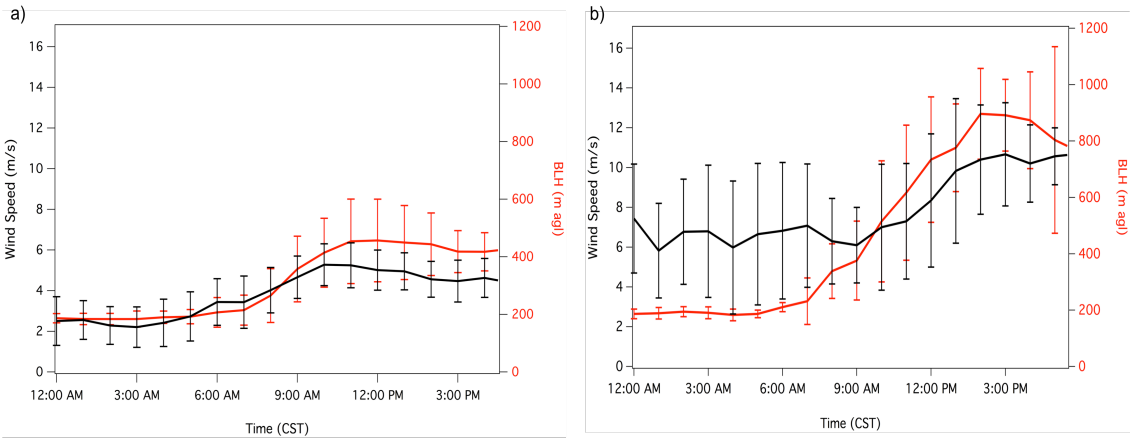

Figure 3.9. One-hour median wind speeds and BLHs for all days designated into scenarios B (a) and D (b).

Scenario C (13.6%) consists of days where the largest aerosol gradient is found above the regularly detected 400-600 m agl layer top as in shown in Figure 3.8c. These days were typically associated with northerly winds. The jump between the NSL and the ML due to time-of-day height limits is also seen on those days when the wavelet algorithms increase its detection height two hours after sunrise. These days were either

preceded by northerly or westerly winds in previous days or hours and/or had N/W winds during the MLH detection time. This points to higher MLHs when land air masses arrive at Galveston Island likely transporting aerosols at higher altitudes (above ~400 m agl) and allowing for relatively higher MLH over the Galveston site than those without N/W winds. Days categorized in this scenario did not show a significant morning time wind speed increase (less than a factor of 1 increase).

Backward trajectories for days in scenario C had both marine and continental air masses similarly observed for scenario A. However, surface-wind measurements for scenario A and C showed predominant SE winds and NW winds, respectively, and higher BLHs in scenario C than A. This suggests that a combination of long range continental air mass transport, surface winds from the NW, and high wind speeds (i.e. greater than 7 m/s) are favorable for higher BLHs. Stronger aerosol mixing due to higher wind speeds could explain the higher BLHs detected in this scenario as opposed as those BLHs measured in scenarios A and B. Days, in which backward trajectories displayed transport of clean marine air mass to the site, were typically associated with higher surface wind speeds than those days with continental trajectories. Although marine trajectories are expected to correspond to lower BLHs than those with continental trajectories, the high wind speeds observed can explain higher BLHs similar to continental trajectories. This suggests that in this scenario, more recent boundary layer forcing mechanisms (heat flux, frictional drag, wind speeds, etc.) outbalance previous physical properties of the air mass.

Scenario C was most often observed in the winter and fall seasons. Maximum BLHs were measured during the spring season at about 1120 m agl whereas the winter season maximum BLHs are lower at approximately 995 m agl (Table 3.4).

Scenario D (2.6%) differs from scenario C in that a continuous transition between the NSL and the ML is clearly observed (Fig. 3.8d). These days were associated with winds typically greater than 7 m/s (Figure 3.9b) from the from N or NW direction on the same or preceding days, as well an increase in wind speeds at the time of the morning BL growth, similar to scenario B cases, but with a higher increase of at least a factor of 3 and a factor of 4.2 in average (Figure 3.9b). The wind speed increase was seen less frequently (19 out of 29 days) than those in scenario C (55 out of 153 days).

Scenario D backward trajectories showed air masses traveling over the continental US except for two cases that corresponded to the highest wind speed increase measured for all days in scenario D. Both scenarios B and D show a connection between the NSL and ML and continental air mass trajectories, however scenario D surface winds were typically from the N and NW directions, while scenario B shows winds typically from the S/SE direction. Wind speeds and BLHs for scenario D (Figure 3.9b) show both higher BLHs and higher wind speeds than scenario B (Figure 3.9a).

3.5.3. Case study of the Coastal Boundary Layer

Here, we present a case study that shows the coastal BL evolution for October 9, 2016 using aerosol backscatter from the two collocated ceilometers and three-morning time radiosonde launches. Synoptic conditions on October 9, 2016, show high pressures

over the central US, including the Galveston site. This high pressure follows a frontal passage on October 4, 2016. Upper level winds are from the NE direction. Surface observations during October 9, 2016, also show persistent NE winds at 4-8 m/s. HYSPLIT backward trajectories at 14:00 and 15:00 CST show continental air mass flows from NE passing over the US southeast and mid-west regions.

Figures 3.10a – 3.10c display radiosonde profiles in skew-*T log-P* diagrams from launches at 6:30 CST (Figure 3.10a), 8:30 CST (Figure 3.10d), and 10:40 CST (Figure 3.10c). Wind profiles from all radiosonde launches show NE winds and wind speeds at about 6-8 m/s from the surface to about 300 m agl; above this altitude winds slightly shift to the E direction with slightly higher wind speeds of about 10-12 m/s. At about 700 m agl winds shift back towards the NE direction with wind speeds decreasing to about 6-8 m/s. Winds above 700 m agl are consistently from the NE direction. These wind shifts correlate with the multi-layer structure over the Galveston site shown in Figure 3.10a – 10c. Figure 3.10a shows temperature inversions or layer tops at about 320 m agl and 520 m agl at 6:30 CST, which later rise to 340 m agl and 650 m agl at 8:30 CST (Figure 3.10b) and at 450 m agl and about 700 m agl, respectively, at 10:40 CST (Figure 3.10c).

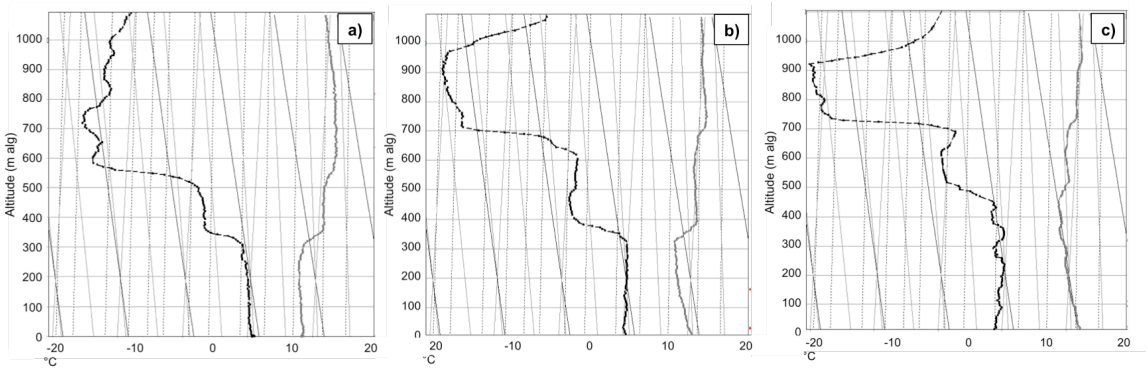

Figure 3.10. Radiosonde vertical profiles of dew point temperature (black line) and temperature (grey line) in m agl. Radiosonde launches at about 6:30 CST (a), 8:30 CST (b), and 10:40 CST (c).

The case study day October 9, 2016 is assigned to scenarios D, as it agrees well with the conditions previously discussed associated with this scenario. Peak BLH on this day was measured at ~1120 m agl at 14:30 CST, however only a small wind speed increase of a factor of 1.7 was seen. This factor is a significant departure from the average factor of 4.9 typically accompanying scenario D. No wind direction shift to S/SE winds indicative of a sea breeze was observed on this day, where synoptic winds could have inhibited the development of the sea breeze. Additionally, the TIBL typically linked with the sea breeze was not detected in either radionsonde or aerosol backscatter profiles, further supporting the TIBL as a phenomenon directly associated with the sea breeze.

Overall, the radiosonde data results show a stratified coastal boundary layer with aerosol layer tops measured by the CL31 data that correspond to layers measured in the radiosonde profiles. Each of these layers has different wind speed and directions than layers above or below. The stratification present on this day suggests that a stratified coastal boundary layer commonly seen in the CL31 measurements is not specific to

aerosol backscatter measurements, but actually corresponds to thermodynamically derived layers by the radiosondes over the Galveston site.

3.6. Summary and Conclusions

In this work aerosol backscatter derived BLHs measured at a coastal site in Southeast Texas were studied. Continuous aerosol backscatter measurements from September 1, 2013 to September 30, 2016 retrieved by a Vaisala CL31 ceilometer are used. CL31 aerosol backscatter profiles are measured every 16 seconds with a maximum height of 4500 m and a 10 m resolution. BLHs are calculated every 10 minutes using data screened for rain showers, fog and cloud cover events, as they create limitations in the BLH retrieval using aerosol backscatter. The removal of these events from the analysis accounted for 45.7% of all 1126 study days. The removal of these signals in turn revealed that the Galveston area experiences the most precipitation in spring seasons, and clouds layers are most often present in the summer months.

Cloud and precipitation-free aerosol backscatter signals were divided into four scenarios of similar BLHs and BL evolution. Surface wind measurements and HYSPLIT backward trajectories were observed for each scenario and are summarized in Table 3.5.

Table 3.5. Predominant conditions and HYSPLIT backward trajectories observed for scenarios A-D.

Scenario	MLH range	Wind Direction	Wind Speed	Wind speed increase*	HYSPLIT
A	~400-600 m	S/SE	Light - Moderate < 7 m/s	0.5 0.2 – 0.9	Both continental and marine
B	~400-600 m	S/SE	Light - Moderate < 7 m/s	2.1 1.2 – 4.9	Continental
C	~600-1100 m	N/NW	Moderate - High > 7 m/s	0.8 0.7 - 1	Both continental and marine
D	~600-1100 m	N/NW	Moderate - High > 7 m/s	4.2 1.4 – 10.4	Continental

**Average factor of wind speed increase and their ranges; average times vary daily and seasonally.*

1) Scenarios A (19.9% of days) and C (13.6% of days) were the most frequently observed scenarios with most occurring in the summer and winter months, respectively. Scenarios B and D were less frequent (3.8 and 2.6 % of days, respectively) and had the highest number of days in the winter and fall months respectively.

2) Overall scenarios A and B showed relatively low BLHs ranging from ~400-600 m agl, but only scenario B displayed a gradual connection between the NSL and the ML. Both scenarios are associated with light to moderate wind speeds (<7 m/s) from the S/SE directions. They differ in backward trajectories with scenario A showing a combination of both continental and marine trajectories, while B consisted of mostly continental trajectories. Most importantly however, the increase in wind speeds during the morning hours (by a factor of 2.1) correlated very well with the gradual connection between the NSL and ML in scenario B.

3) Scenarios C and D detect higher BLHs up to about ~1100 m agl with scenario D distinctly measuring a gradual growth from a NSL to a ML with accompanying wind speeds increase by a factor of 4.2 on average (scenario C sees increases by a factor of 0.8). Both scenarios were associated with moderate to high wind speeds (>7 m/s) N/NE surface winds. However, they were different in backward trajectories, where C days were linked to both continental and marine trajectories, while D days were linked to mostly continental trajectories.

4) BLHs are found to be relatively low in scenarios A and B and associated with low winds speeds from the S/SE directions, while higher BLHs occur in scenarios C and D with high wind speeds from the N/NW directions. Additionally, as BLHs did not show a strong correlation to backward trajectories, it can be concluded that over a coastal area the local land-sea breeze circulation might largely modify turbulent properties of advected air masses and thus be of more influence in the development of the BLHs than the air mass type.

5) The case study showed a stratified coastal boundary layer with aerosol layer tops corresponding to layers measured in the radiosonde profiles. Each of these layers displayed different wind speed and directions than layers above or below. The results show that the detected layers are not only specific to aerosol backscatter measurements, but also correspond to thermodynamically derived layers measured by radiosonde data over the Galveston site.

4 Spatial boundary-layer-height observations using aerosol LIDARs and comparison to WRF model – A case study

4.1 Introduction

The Houston-Galveston area has been of considerable interest over the past decades as it contains a large and diverse source of emissions from automobiles, power plants, refineries, and petrochemical plants combined with a complex local to regional scale wind circulation from the nearby Gulf of Mexico and Galveston Bay (Banta et al., 2005). The sea and bay breeze circulations arise from the difference in specific heat of land and water. After sunrise, air over land will warm faster than air over water. This warm air will eventually rise and allow cooler surface onshore air from the E and SE to move inland while a warmer offshore return flow typically from the W and NW can be experienced above (Tijm et al., 1999). The difference in air temperature also creates the land breeze during nighttime hours when the air over land cools down more quickly than the air over water. The rising warmer air allows for the cool land breeze air to move in replacing the warm air typically from the N and NW directions.

Recirculation of aged air masses is an important aspect of the sea breeze systems. As described above, rising warm air will allow cooler surface onshore air to move inland while a warmer offshore return flow can be experienced aloft. A near-surface return flow is also commonly seen in the nighttime hours with the onset of the land breeze. Both return flows (lofted land recirculation or near-surface land breeze) will have imbedded physical characteristics and pollutants that can be carried offshore where, once over water, will be subject to different removal processes depending on the

water solubility of each individual traces gas. Pollutants with low water solubility such as ozone will not be efficiently removed over water and can be carried back over land with the next day's onset of the sea breeze. In these cases, the land/sea breeze recirculation can contribute to increased upwind pollutant concentrations.

Various studies have investigated the meteorological conditions responsible for high ozone events in the Houston area, such as those studies performed by Banta et al. (2005) and Darby (2005), which take a closer look at the effect of the sea breeze and circulation patterns in the Houston area. Banta et al. (2005) determined that the progression of the sea breeze can simulate a frontal structure along the Galveston Bay and the Gulf of Mexico coast and advance inland. The convergence of an offshore synoptic flow and the sea breeze create a period of stagnation that favor the accumulation of pollutants that lead to high ozone concentrations. Banta et al, (2005) also found that the strength, speed and onset times were determined to be slower and later in the day during offshore flow than in calm onshore flow.

Similar to the August 30, 2000 high ozone event day described in Banta et al. (2005), the case study we present here on September 25, 2013, was also characterized by a strong sea breeze contributing to high ozone concentrations. Here, we will study the effect of the sea breeze in the BL evolution and the implications for air quality.

The airborne LIDAR measurements provide an opportunity to quantify spatial and temporal variations of BLHs and pollutants. For instance, Banta et al. (1998) used an ozone LIDAR to investigate the buildup and transport of ozone in the BL during a stagnation episode in Nashville, Tennessee. Hoff et al. (1997) investigated the sources and removal processes of aerosols in the Georgia Strait region. More recently,

Langford et al. (2009) used an airborne ozone LIDAR to characterize the spatial distribution and mixing of ozone in the Houston area. Scarino et al. (2014) used a high spectral resolution LIDAR to study the BL evolution over the Los Angeles and Sacramento areas in California. Similar to these studies, the extensive data set collected during the DISCOVER-AQ (Deriving Information on Surface conditions from Column and Vertically Resolved Observations Relevant to Air Quality) Campaign, where multiple aerosol backscatter LIDARs including one airborne LIDAR were deployed, allows for a spatial analysis of the BLH. Here we present results from September 25, 2013. On this day clear sky conditions (with only a very few scattered clouds for the entire day) and significant aerosol loading as observed with the CL31 (not shown) allowed for optimal BLH detection across LIDAR instrumentation. This study will first observe BL evolution at each ground LIDAR site and corresponding surface wind measurements, then use an airborne LIDAR to spatially connect ground sites into a spatial BL evolution study. Surface wind measurements will be used to study the inland progression of the sea breeze and relate the finding to potential impacts on the BLH.

Further, this study will compare LIDAR observed BLHs with those simulated by an air quality model system. This modeling platform will be used to examine the relationship between the evolution of the modeled BLH, the sea breeze simulated by the model, and the connection between BLHs and the sea breeze.

4.2 Data

The data used in this study was measured during the 2013 Texas NASA DISCOVER-AQ Campaign in the Houston area during the month of September 2013.

The overarching goal of this campaign was to improve ground-truthing of total-column satellite observations related to air quality conditions in the atmospheric boundary layer. For this reason, all observational data were coordinated to be close in time and space to be comparable to various surface, remote sensing, and in-situ airborne measurement platforms. In this study, we combine CL31 aerosol backscatter data measured on the campus of the University of Houston (UH) and on Galveston Island, Micro-Pulse LIDAR aerosol backscatter data measured at Smith Point, aerosol backscatter data from the Ozone LIDAR (TOPAZ) measured at La Porte, and aerosol backscatter from the NASA High Spectral Resolution LIDAR (HSRL) aboard the King Air B200 aircraft (Table 4.1). Figure 4.1 shows the locations of ground LIDARs and the flight tracks of the HSRL over each site.

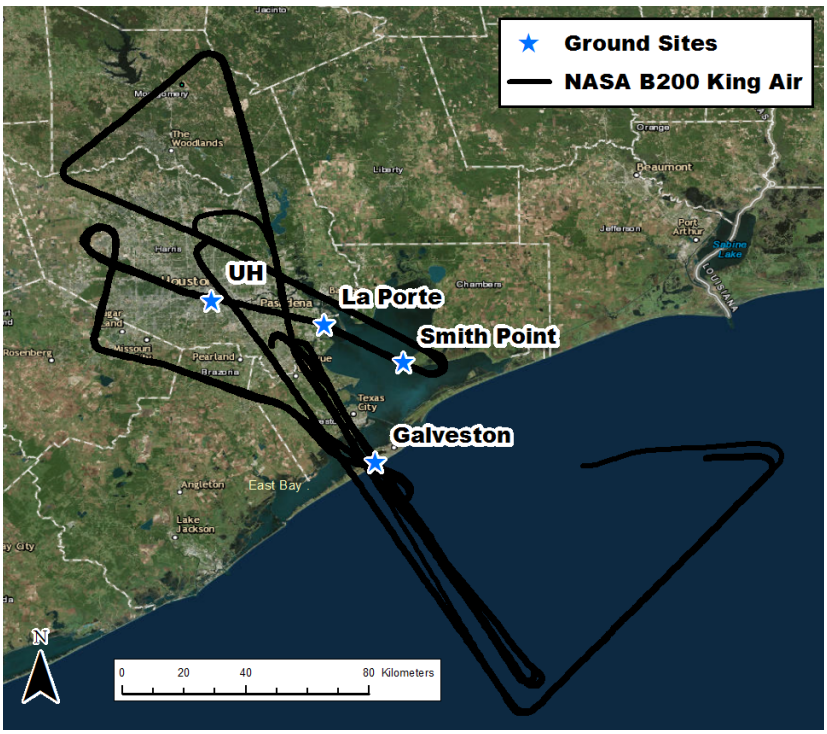

Figure 4.1. Composite flight tracks for September 25, 2013. LIDAR ground sites are shown in blue, and NASA aircraft flight tracks for the NASA B200 in black and NASA P3-B in red.

Table 4.1. Ground LIDARs locations, operating agencies and references.

Site	Latitude	Longitude	Instrument	Operated by	References
Galveston	29.25	-94.86	CL31 ceilometer	TCEQ (Texas Commission on Environmental Quality)	Münkel et al. (2007)
UH	29.72	-95.34	CL31 ceilometer	UH (University of Houston)	Münkel et al. (2007)
La Porte	29.66	-95.01	TOPAZ - Tunable Optical Profiler for Aerosol and oZone	NOAA (National Oceanic and Atmospheric Administration)	Alvarez et al. (2011, 2012)
Smith Point	29.55	-94.78	MPL - Micro Pulse Elastic LIDAR	Millersville University	Campbell et al. (2002)

The standard validation method for BLH detection is typically done against radiosondes, however the La Porte and TOPAZ sites did not have nearby radiosonde launches available. Therefore, for these sites we compared to HSRL derived BLHs. Comparison results are listed in the instrument descriptions. All comparisons are limited to a maximum of one hour between the times that each measurement was taken.

4.2.1 Vaisala CL31

The Vaisala CL31 ceilometers at University of Houston (UH CL31) and Galveston Island (Galveston CL31) operate at a wavelength of 905 nanometers (nm) using an indium-gallium arsenide laser diode (InGasAs) system with a 1.2 microjoule (mJ) pulse for 110 nanoseconds (ns) and mean pulse repetition rate of 8192 Hertz (Hz). A beam splitter gives full overlap of the transmitter and receiver field-of-view at an altitude of 70 m (Münkel, Eresmaa, Räsänen, and Karppinen, 2007). Aerosol backscatter profiles with signals from clouds, rain, or fog are identified as signals higher

than $2000\times10^{-9}m^{-1}sr^{-1}$ and were not used in this study. The CL31 can measure aerosol backscatter up to 7500 m. However, the CL31 does not record these signals, but instead only accumulates aerosol backscatter intensity every 16 seconds with a maximum height of 4500 m and 10 m resolution.

Aerosol backscatter signals below 100 m are removed due to an artificial peak in the ceilometer measured at the 40 m height most likely due to hardware related perturbations and CL31 software corrections in the Vaisala software (Kotthaus et al., 2016). Removing these signals prevent the incorrect calculation of the BLH due to strong gradients created by this artifact (Kotthaus et al., 2016; Sokół et al., 2014). Layers below 100 m are not detected by the Haar Wavelet Method due to the removal of the first 100 m in aerosol backscatter data. As a consequence this would also include the NSL as the removal of the first 100 m in aerosol backscatter might remove signals needed to calculate a lower NSL height.

Cloud-free CL31 aerosol backscatter profiles are averaged first vertically according to Table 4.2 followed by a 10-minute average before applying the Haar Wavelet algorithm. The ceilometer (Figure 4.1) locations require slightly different averaging and BLH retrieval settings. A smaller vertical averaging is applied to the Galveston CL31 (Table 4.2) due to the lower BLHs expected in coastal environments whereas the UH CL31 is expected to measure higher BLH in an urban environment. Too much averaging in lower altitude ranges will smooth gradients corresponding with possible coastal BLHs. Increasing noise with height requires more averaging in higher altitudes. However, high averaging is not needed for BLH detections of lower BLHs in a coastal environment.

Table 4.2. Averaging heights used on aerosol backscatter profiles by height range.

UH CL31		Galveston CL31	
Altitude Range	**Averaging Height**	**Altitude Range**	**Averaging Height**
10 – 490 m	70 m	10 – 490 m	110 m
500 – 990 m	330 m	500 – 990 m	190 m
1000 – 1990 m	590 m	1000 – 4500 m	230 m
2000 – 4500 m	690 m		

The Galveston CL31 is located in at the TCEQ C1034 CAMS site (Texas Commission of Environmental Quality Continuous Ambient Monitoring Station) on Galveston Island, TX (Figure 4.1) at an elevation of approximately 5 m. The site has its closest Gulf of Mexico shore about 0.9 km south and the closest Galveston Bay shore about 2.8 km north. The UH CL31 is located at the UH Main 25 Campus, which is about 70 km northwest of the Gulf of Mexico and 5 km southeast of downtown Houston (Figure 4.1). The UH CL31 was mounted a top a trailer approximately 3.5 m above ground and UH radiosonde launches were performed next to the CL31 trailer.

Caicedo et al. (2016) compared BLH retrievals from radiosonde and CL31 aerosol backscatter data using three distinct BLH retrieval methods. The results presented in Caicedo et al. (2016) showed the Haar Wavelet method to be the most robust and having the best agreement between radiosonde and Haar Wavelet derived BLHs ($r^2 = 0.89$).

4.2.2 NOAA TOPAZ (Tunable Optical Profiler for Aerosol and oZone) LIDAR

The TOPAZ LIDAR system located at La Porte, TX during the DISCOVER-AQ campaign (Figure 4.1) is a DIAL (Differential Absorption Lidar) measuured ozone concentrations and aerosol backscatter. In this study, we only use aerosol backscatter

measurements. An optical scanner allows for measurements at low pointing angles (0-30 degrees) and allows for ground level measurements and higher resolutions near ground level (Alvarez et al., 2011; Alvarez et al., 2012). The TOPAZ uses a Ce:LiCAF (cerium-doped lithium calcium aluminum fluoride) tunable solid-state laser with a tuning ouput range of 285-310 nm. The tunable wavelength feature gives the ability to select appropriate wavelengths depending on the ozone absorption cross section and the ambient various ozone concentrations and it thereby minimizes the interference by gases such as sulfur dioxide. Longer paired wavelengths are used under high ambient ozone conditions and shorter paired wavelengths are used under low to moderate ozone as shorter wavelengths can experience strong attenuation from ozone (Alvarez et al., 2011). It operates at 1 kHz pulse rate at 0.2-0.8 mJ/pulse. Aerosol backscatter profiles are originally retrieved at a 6 m resolution. However, aerosol backscatter profiles are spliced together from vertically projected 2, 6, 20, and 90-degree elevation angle data resulting in higher 1 m vertical resolution. Aerosol signals were averaged or interpolated (depending on the altitude) onto a 1-m altitude grid every 5 minutes (Alvarez et al., 2012; C. Senff, pers. comm., February 2017). The TOPAZ has a typical vertical range of up to 4 km, however this range varies with ozone concentrations. TOPAZ signals above 2 km during DISCOVER-AQ were generally too noisy and were deemed unusable. This is because higher attenuation of backscatter due to stronger aerosol signals and Rayleigh scattering resulted in a lower signal-to-noise ratio (C. Senff, pers. comm., February 2017). The TOPAZ was operational only during daytime from about 7:40-20:00 CST (no NSL measurements available). Here we use a 5 m vertical average and 10 minute average on cloud-free aerosol backscatter profiles before

applying the Haar wavelet algorithm in order to smooth profiles and aid in the detection of the largest aerosol gradients.

The La Porte airport site is approximately 6 km west of the Galveston Bay shore, ~52 km north from the Gulf of Mexico and ~30 km east from downtown Houston at an approximate elevation of 8 m asl. The La Porte site proximity to the Galveston Bay makes it susceptible to the bay breeze from the E direction and to the Gulf of Mexico sea breeze from the SE direction.

4.2.3 MicroPulse LIDAR

The Micropulse Lidar (MPL) is an eye-safe elastic backscatter LIDAR with a neodymium-doped yttrium lithium fluoride (Nd:YLF) laser operating at a 523 nm wavelength, a high repetition rate of 2500 Hz, and pulse rate of 3-4 μJ. The MPL has a 1 minute and 30 m temporal and vertical resolution, respectively, with a vertical range up to 60 km (Campbell et al., 2002). A range correction for the MPL overlap is required in the 0-6 km range and is applied as described in Campbell et al. (2002) and Berkoff et al. (2004). No further vertical averaging is applied to MPL profiles due to the 30 m resolution which in some cases, might be too low to resolve for shallow aerosol gradients and would not benefit from additional averaging. The first three measurements (90 m) are removed from the data set due to unreliable aerosol backscatter signals in these ranges likely due to the overlap corrections.

The Smith Point is an area of land that protrudes into the north east of Galveston Bay. Smith Point MPL measurements are located about 20 m from the nearest Galveston Bay shore, 30 km northeast from the Gulf of Mexico, and 60 km southeast

from downtown Houston at 5 m asl. As can be seen in Figure 4.1, Smith Point is surrounded by the Galveston Bay and is therefore expected to encounter strong influences from the bay breeze from the W direction. A strong sea breeze would be expected from the South direction. No ground measurements at Smith Point were available; therefore we use the Millersville University SODAR (SOnic Detection And Ranging) for surface wind speed and wind direction measurements. The La Porte wind profiler is used to infer winds at altitudes higher than 300 m as the SODAR cannot measure above this height.

4.2.4 NASA HSRL (High-Spectral Resolution LIDAR)

The downward-looking HSRL aboard the NASA B200 aircraft was flown around the Houston area at an altitude of approximately 8.5 km and followed similar flight track four times on September 25 at around 7:30-9:30, 9:30-11:00, 12:30-14:30, and 14:30-16:00 CST (Figure 4.1). The HSRL system uses a continuous-wave (CW) injection seed laser and a pulsed Nd:YAG (neodymium-doped yttrium aluminium garnet) laser. The HSRL measures aerosol extinction at 532 nm, backscatter at 532 nm and 1064 nm, depolarization at 532 nm and 1064 nm and aerosol optical depth (AOD) at 532 nm (Hair et al., 2008). This study uses 532 nm aerosol backscatter profiles from the HSRL. The 532 nm aerosol backscatter measurements are averaged over 30 m vertical resolution with a 15 m sampling interval computed every 0.5 s using a 10 s running average equivalent to ~1 km horizontal resolution (Hair et al., 2008; Rogers et al., 2008).

Profiles with cloud signals are removed from the analysis due strong aerosol gradients created by cloud signals mistakenly identified as the BLH, aerosol backscatter extinction below the cloud (downward looking LIDAR), and the distortion of aerosol backscatter above the cloud. Cloud-free 532nm aerosol backscatter profiles are smoothed using a 45 m running height average before applying the Haar Wavelet method for BLH detection. A comparison between the Smith Point radiosondes and the HSRL derived BLHs during the entire DISCOVER-AQ campaign was performed and resulted in an overall good agreement (r^2= 0.92).

4.2.5 Supporting Data Set - iMet Radiosondes

International Met Systems Incorporated model iMet-1 radiosondes were launched at the Smith Point and UH ground sites. iMet-1 radiosondes return GPS (Global Positioning System) location, GPS altitude, wind speed and direction, pressure, temperature, and relative humidity with a 1 Hz sampling rate using a 403 MHz transmitter. Radiosondes used here have a resolution of 0.01hPa, a response time of 1s, and an accuracy of 0.5 hPa for pressure measurements. Temperature sensing has a resolution of 0.01 °C, an accuracy of 0.2 °C, and a response time of 2 s. The humidity sensors for the radiosondes have a resolution of less than 0.1%, an accuracy of 5%, and a response time of 2 s. Average ascent rate for all launches was about 5 m/s.

4.3 Methods

4.3.1 Haar Wavelet Method

Aerosol derived BLH methods presented here are based on two assumptions: 1) the BL contains somewhat constant concentrations of aerosols due to convective and turbulent mixing and 2) the clean FT above will create a negative gradient in aerosol backscatter from higher concentrations within the BL towards lower concentrations in the FT. The local maximum of this gradient is identified as the top of the BL (Steyn et al., 1999).

Aerosol backscatter BLHs are derived with a Covariance Wavelet Transform utilizing the Haar wavelet compound step function with multiple user defined wavelet dilations (Baars et al., 2008; Brooks, 2003; Cohn and Angevine, 2000; Compton et al., 2013; Davis et al., 2000; Uzan et al., 2016). This method identifies the sharp aerosol-backscatter gradient corresponding to the top of the BL by calculating the wavelet transform. The Haar wavelet function *h* is defined as follows:

$$h\left(\frac{z-b}{a}\right) = \begin{Bmatrix} -1: b - \frac{a}{2} \le z < b \\ +1: b \le z \le b + \frac{a}{2} \\ 0 : elsewhere \end{Bmatrix}, \tag{4.1}$$

where z is the vertical altitude in this application, a is the vertical extent or dilation of the Haar function, and b is the center of the Haar wavelet function. The covariance transform of the Haar wavelet function, w_f is defined as:

$$\mathrm{w_f(a,b)} = \mathrm{a^{-1}} \int_{\mathrm{z_b}}^{\mathrm{z_t}} \mathrm{f(z)h}\left(\frac{\mathrm{z-b}}{\mathrm{a}}\right) \mathrm{dz}\ , \tag{4.2}$$

where z_t and z_b are the top and bottom altitudes in the aerosol backscatter profile, $f(z)$ is the aerosol backscatter profile as a function of altitude, and a is the normalization factor or the inverse of the dilation, respectively.

Defining the dilation factors a and the range of centers of b of the Haar wavelet function are key in correctly identifying the BLH using aerosol backscatter profiles. In this study, b ranges from the lowest acceptable ceilometer recorded aerosol backscatter altitude of 100 m to a maximum BLH of 1300 m.

As with previous studies (Baars et al., 2008; Brooks, 2003; Compton et al., 2013; Scarino et al., 2014) the dilation factor a affects the number of covariance wavelet transform coefficients (CWTC) local minimums. Larger values create large local minimums at the heights of the biggest aerosol gradients in the aerosol backscatter profile. Lower dilation values create numerous CWTC local minimums at heights of smaller aerosol gradients in the measured profiles. A range of dilation values is applied to the aerosol backscatter profile. The algorithm is applied to each LIDAR profile with incremental dilations until the maximum dilation factor is reached. The mean of all resulting CWT coefficients is then calculated and the local minimum of the mean CWT coefficients is identified as the BLH.

Lower dilation values are generally applied during nighttime and early morning hours, when the residual layer or lofted aerosol layers signals can create large gradients. In these cases the gradient closest to the surface is chosen as the BLH (or the NSL) with the aid of the height restriction. Higher dilation values during daytime hours are applied in order to detect the largest gradient and prevent the detection of other smaller gradients along an aerosol backscatter profile not corresponding to the MLH. The

dilation settings are set to automatically change two hours after sunrise (i.e., 8:00 CST for the case of September 25, 2013), except for the HSRL for which dilations are detailed in Table 4.3.

Table 4.3. Dilations and height detection limits (m agl) applied in the Haar Wavelet algorithm to each LIDAR.

LIDAR	Time (CST)	Dilation factor *a*	Height Detection Limits
HSRL	07:00 - 10:00	150 m over water	45 – 800 m over water
		750 m over land	45m – 1000 m over land
	10:00 - 17:00	150 m over water	150m – 1000 m over water
		750 m over land	45m – 3000 m over land
UH CL31	Nightime	30 m	100m – 500 m
	Daytime	300 m	100m – 2800 m
Galveston	Nightime	30 m	100m – 300 m
CL31	Daytime	100 m	100m – 1300 m
MPL	Nightime	270 m	100m – 500 m
	Daytime	870 m	100m – 2800 m
TOPAZ	Nightime	10 m	100m – 500 m
	Daytime	30 m	100m – 2000 m*

*No TOPAZ data available above 2000 m

Here we apply the dilation factors listed in Table 4.3 for each LIDAR instrument. These dilation factors were tested for each instrument and showed the most reliable BLH detection for the case study day with the least amount of misidentified BLHs and requiring little or no manual inspection. The HSRL uses different dilations for measurements over land and over water. We expect lower BLHs over water than those over land, therefore lower height limits are applied for measurements over water along with lower *a* values of 150 m over water and 750 m over land. This height limit also prevents the detection of residual layer signals during nighttime and early morning hours. An additional change in settings is applied after 10:00 CST when BLHs are expected to exceed the early morning detection limits. An additional height detection

limit is applied according to the time-of-day (Table 4.3) and switches at the same time as the dilation factor *a*.

Instruments with relatively higher resolutions (TOPAZ and CL31) use lower dilation values while instruments with relatively lower resolutions (MPL and HSRL) require high dilation values in order to detect significant aerosol gradients. CL31 dilation and height detection ranges were tested in Chapter 2, and are kept the same in this study. Height detection ranges applied to the HSRL, MLP and TOPAZ LIDARs are similar to those used for the CL31.

4.3.2 Skew-*T Log-P* method for radiosonde and P3-B profiles

A stable BL is characterized by having an environmental lapse rate greater than a moist/dry adiabatic lapse rate, while an unstable boundary layer is identified by having a dry adiabatic lapse rate greater than the environmental lapse rate. Stable profile BLHs are identified as the top of the shallow stable layer where a strong positive vertical gradient change in temperature and a strong negative gradient in dew point temperature are present. BLHs during unstable conditions are identified as the base of the stable EZ (i.e., temperature inversion) where the temperature profile intersects dry adiabats and/or where relative humidity or dew point temperature profiles sharply decrease as seen in the skew-*T log-P* diagram in (Haman et al., 2012; Kovalev and Eichinger, 2004; Stull, 1988). A previous study by Haman et al. (2012) found a correlation coefficient of 0.96 during unstable conditions and 0.91 during stable conditions when comparing ceilometer and radiosonde derived BLHs (both manually) using the skew-*T log-P* method.

4.3.3 Model Simulation

The Advanced Research Weather Research and Forecast (ARW-WRF), model version 3.7, was used (Skamarock et al., 2008) with two model domains and one-way nesting technique; the domains with sizes 161 x 145 and 97 x 79 with the horizontal resolution of 12 km and 4 km, respectively, centered over the state of Texas (coarse domain d01) and one nesting domain d02 centered over Houston (Figure 4.2). WRF was run for a 48-hour simulation period and initialized on September 24 at 06 UTC, 2013. The first day was considered spin-up; the model results of the last 24 hours-simulation period were used for further analysis. The NCEP North American Regional Reanalysis (NARR) data with 32-km horizontal resolution were downloaded from the UCAR website (http://rda.ucar.edu/datasets/ds608.0/) and used for initial and boundary conditions for the simulation. Table 4.4 shows some WRF characteristics for this experiment. The model simulations used here are part of an ongoing Texas Air Research Center (TARC) project (Li et al., 2017).

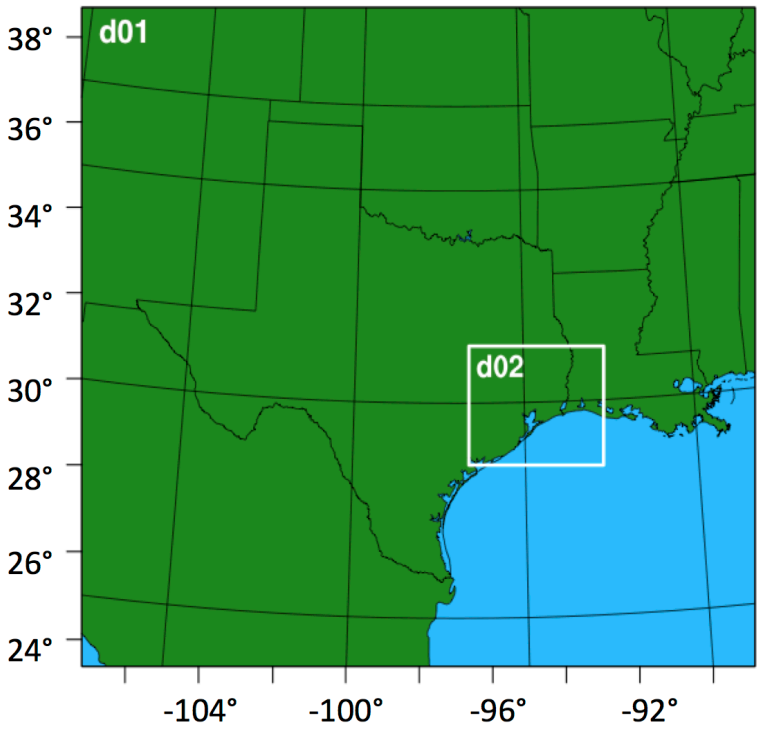

Figure 4.2. Outer coarse (d01) and nested inner domain (d02) used for the WRF System.

Table 4.4. WRF characteristics used

WRF Version	3.7 (released April 2016)
Simulation period	From 09/24 at 06 UTC to 09/26 at 06 UTC
Grid resolution	12 km x 4 km
Microphysics	Lin scheme
Long-wave radiation	Rapid Radiative Transfer Model for GCMs (RRTMG)
Short-wave radiation	New Goddard scheme
Surface layer	Monin-Obukhov with Carslon-Boland viscous sublayer
Land-surface Option	Unified Noah Land Surface Model
Boundary layer	Yonsei University (YSU)
Cumulus Cloud	Kain-Fritsch

The YSU boundary layer scheme used in WRF is a non-local closure model. This feature considers fluxes not only of neighboring cells, but other cells in a vertical grid. For this reason, a non-local scheme better represents the vertical mixing during convective conditions (Hong et al., 2006). The YSU scheme defines the BLH as the

height where the heat flux reaches a minimum and is identified in the critical bulk Richardson number approaching a zero value (Hong et al., 2006). Zhang et al. (2010) identified an over prediction of daytime BLHs under sea breeze conditions over the Houston area using the YSU scheme. This is not an usual result as the YSU scheme has a tendency to over estimate the BLH in deep convective environments resulting in predictions of higher temperature and lower moisture near the surface (Hu et al., 2010; Coniglio et al. 2013; Cohen et al., 2015). Studies such as Czader et al. (2013), Cuchiara et al. (2014) and Wilmot et al. (2014) have tested BL schemes and found YSU to be the better scheme for the Houston area.

The simulation of the sea breeze circulation has been extensively studied in various locations worldwide and the strength and inland propagation of the sea breeze seems to be largely influenced by the prevailing synoptic flow, simulation of land/sea surface temperatures, winds, and BLHs, and the classification of land use and land cover (e.g. Bao et al., 2005; Angevine et al., 2006; Fast et al., 2006; Chen et al., 2015). Here we use near-surface measurements of air temperatures, winds, and sea surface temperature (SST) to understand the differences between the modeled and observed sea breeze on September 25, 2013.

4.4 Case Study

Here we present the case study of September 25, 2013. On this day a strong sea breeze made its away across the Houston area. The effect of the sea breeze on the BLH and the BL spatial and temporal evolution is studied. The case study is analyzed in the

following sequence: the BLH and its evolution as detected by the ground LIDARs are discussed first along with the surface wind measurements (on the UH campus measurements taken at approximately 70 m agl) and airborne HSRL measurements at each location. Additional TCEQ CAMs sites are used to detect the progression of the sea and bay breeze relative to each ground LIDAR site.

On September 25, 2013 surface and upper air winds show low (<5 m/s) winds from the N direction at 6 CST. Similar synoptic winds from the north and west directions at wind speeds typically below 2 m/s (1.3 m/s on average) are measured consistently along all CAMs sites in the nighttime and morning hours (before the onset of the sea/bay breeze).

4.4.1 Ground-Based BLHs

Figure 4.3 shows the diurnal BLH evolution measured by the ground LIDARs for September 25, 2013 from 00:00-18:00 CST. Due to the afternoon decoupling of the BL, which created multiple aerosol layers and therefore multiple aerosol gradients, we do not include measurements past 18:00 CST, as multiple aerosol layers prevent the correct determination of the BLH. Morning time fog was measured over parts of the Gulf of Mexico, Smith Point and La Porte sites. Aerosol backscatter derived BLHs are not reported in this case (note: Figure 4.3 shows hourly averages which do not contain any fog signals).

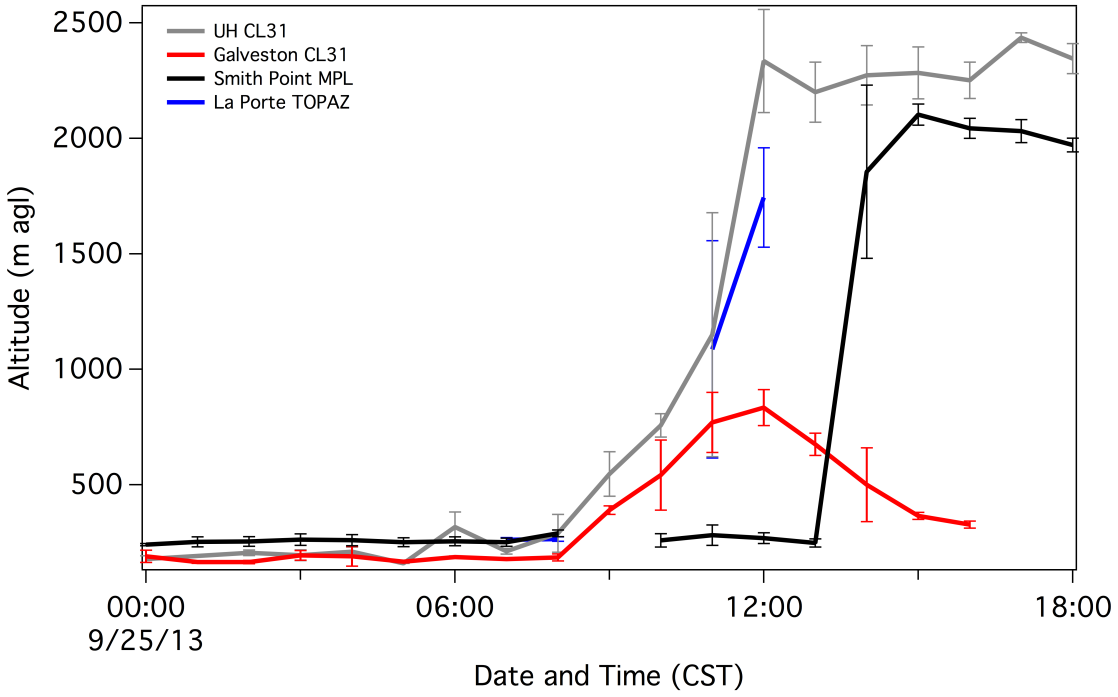

Figure 4.3. Hourly averages and standard deviations for BLHs detected by each ground LIDAR on September 25, 2013.

4.4.1.1 Galveston

The CL31 at the Galveston site measured NSL heights at an average of 180 m agl (Figure 4.3) with low average nighttime (00:00-06:00 CST) winds speeds of 1.3 m/s from the N/NW direction (Figure 4.4a and 4.4b). The Galveston BL begins to grow at about 08:00 CST and the onset of sea breeze (SE winds) is detected at about 11:00 CST (Figure 4.4a). The Galveston BL reaches its maximum hourly average height of 834±78 m agl at 12:00 CST (Figure 4.3). The BLH at Galveston unexpectedly decreases after 12:00 CST likely due to the strengthening of the sea breeze essentially pushing Galveston air inland and being replaced by cooler marine air (Snyder and Strawbridge,

2004). This is indicated by near-surface temperatures remaining relatively constant (~31 °C) after the sea breeze onset at that site.

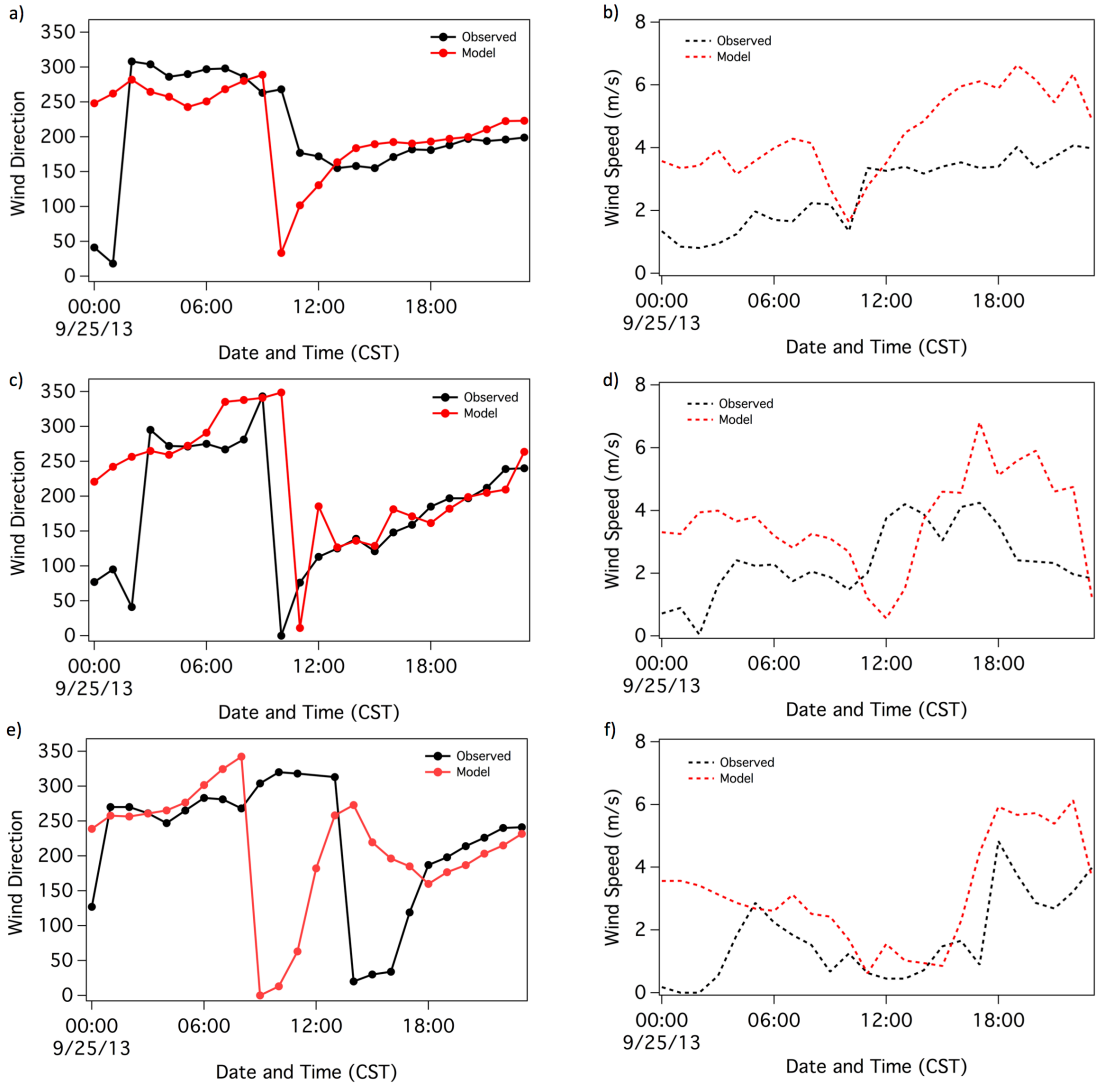

Figure 4.4. Modeled and observed winds at Galveston (a,b), La Porte (c,d) and UH campus (e,f).

The HSRL measurements over the Galveston site showed an interesting feature in the afternoon hours where the upper portion of the land-BL extrudes past the coast (Figure 4.5a and 4.5b). This extruding portion of the BL extends approximately 20 km

offshore over the West Bay, Galveston, and the Gulf of Mexico at around 14:30 CST (Figure 4.5a). Figure 4.5b shows the same airplane traverse at 15:30 CST, when this layer now extends to nearly 40 km offshore. No vertical wind profiles are available at this site so we use the nearest wind profiler at the University of Houston Coastal Center (UHCC; ~23 km NW of the Galveston site) as shown in Figure 4.6a. Wind profiler data comes from CAP-Cooperative Agency Profilers (http://madis-data.noaa.gov/cap) and have a range of about 100 m up to 3 km with vertical range resolutions from 60 m to 400 m and a 30-minute resolution.

The vertical profiles after 12:30 CST show N/NW winds above 1000 m agl indicative of the offshore return flow (recirculation) above the surface level sea breeze out of the SE direction. Steele (2013) studied the return flow component of the sea breeze at the south coast of England and found a return flow vertical depth (from both models and observations) approximately twice the vertical depth of the onshore sea breeze. For our case study, the onshore sea breeze at the time of these Figure 4.5a (~14:30 CST) measurements extends approximately 30 km inland as observed in the TCEQ CAMs surface wind measurements (SE winds) and approximate 40 km inland at ~15:30 CST (Figure 4.5b). The vertical depth of the observed return flow agreed with the findings by Steele (2013), i.e., typically about twice the magnitude of the sea breeze flow (Figure 4.5a, 4.5b, and 4.7a). Figure 4.7b however, shows a well-mixed BL with a lofted return flow that has penetrated down near the surface.

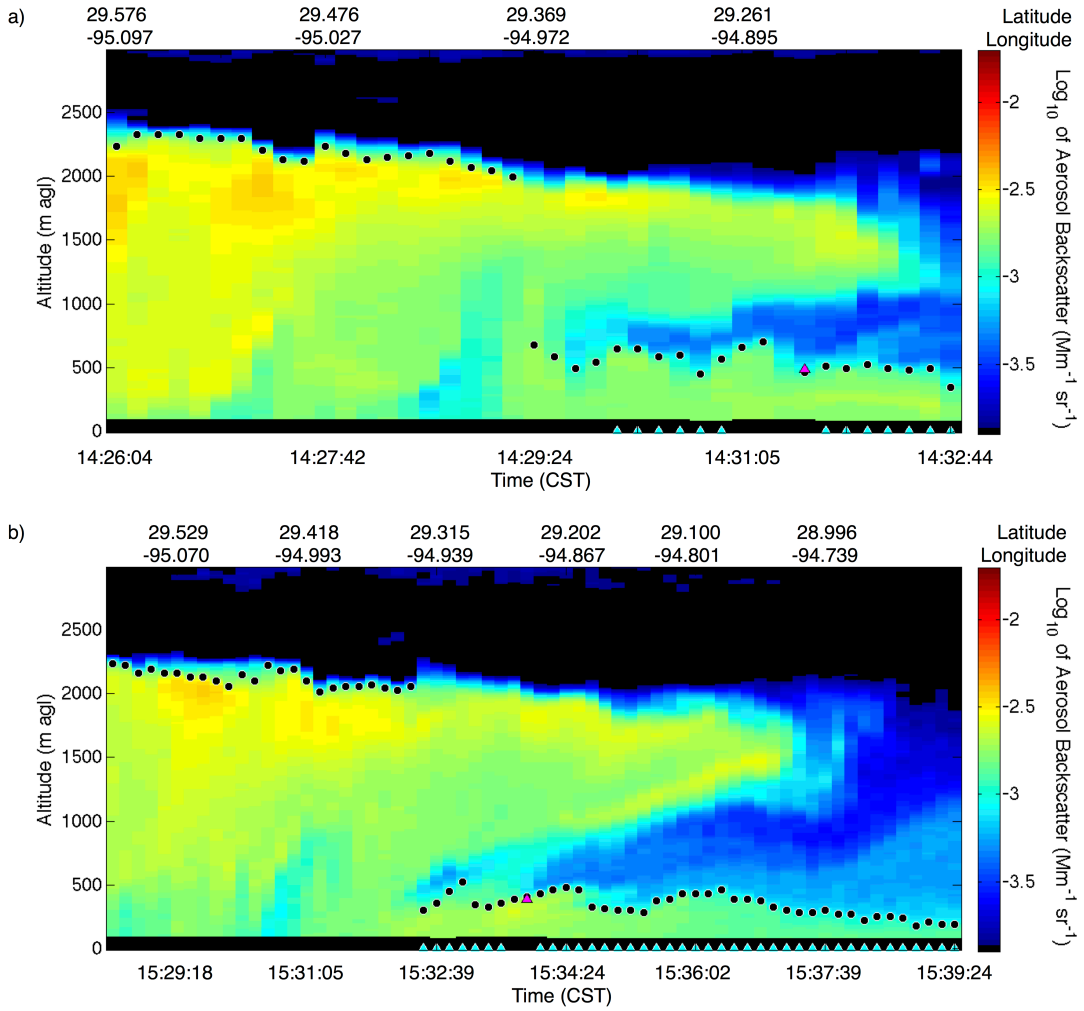

Figure 4.5. HSRL aerosol backscatter plots taken over Galveston and the Gulf of Mexico at about (a) 14:30 CST and (b) 15:30 CST (aircraft traveling from land to sea). Galveston CL31 BLH measurements are displayed as the magenta triangle. Measurements over water are indicated by the blue triangles at 0 m altitude.

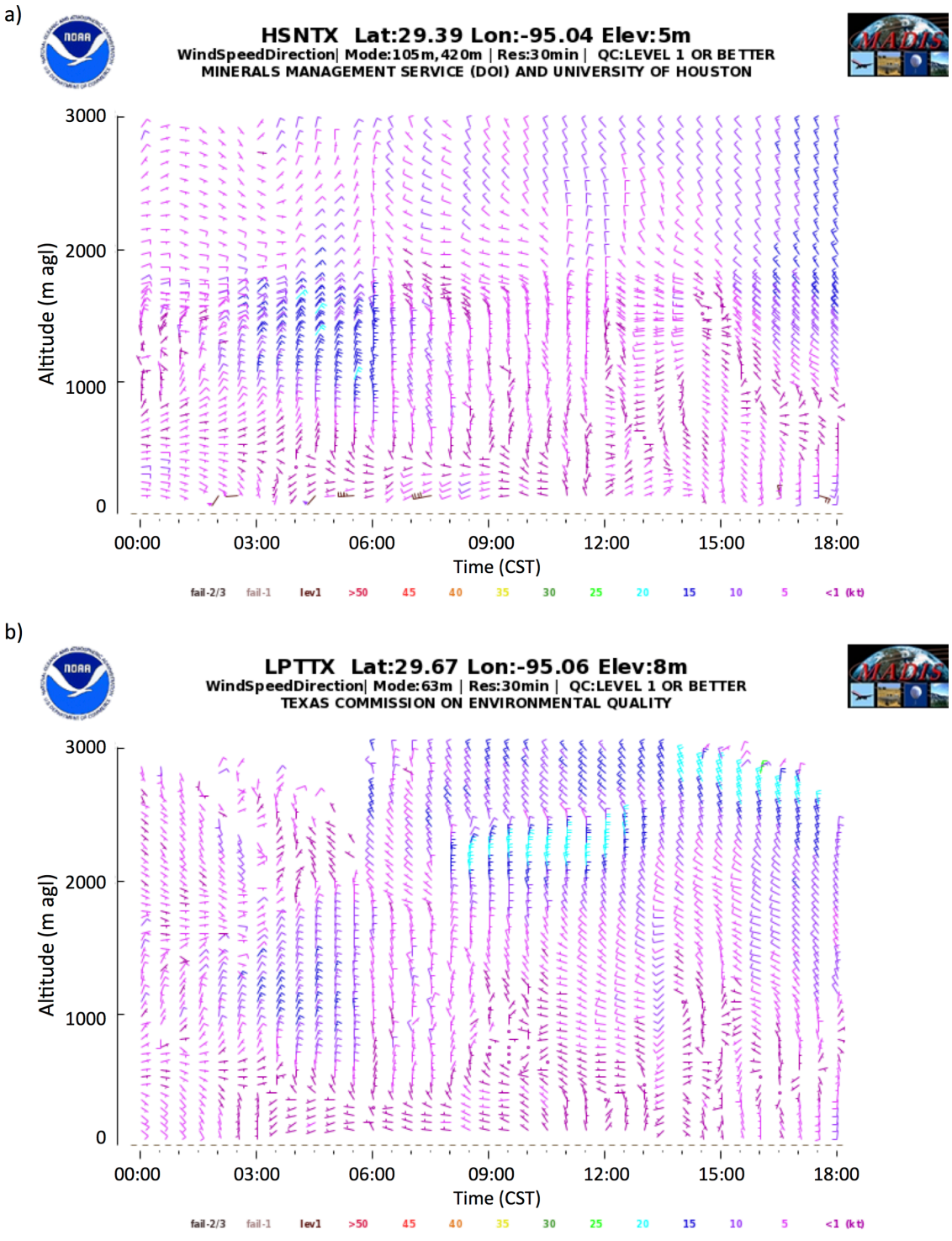

Figure 4.6. Wind profiler plots in CST for September 25, 2013 measured at the (a) UHCC and (b) La Porte.

4.4.1.2 Smith Point

The MPL measured in Smith Point approximately 30 km NE of the Galveston site in the NE side of Galveston Bay. The Smith Point site experienced some morning time fog where data from the MPL was removed (08:00-10:00 CST). Wind directions at this site are indicative of the bay breeze and land breeze in opposite directions than the UH and La Porte sites. At the Smith Point site (see Figure 4.1) we expect a bay breeze from the W direction and a land breeze from the E direction. The gulf breeze would be expected to arrive from the S and SE directions.

SODAR winds show nighttime winds from the E direction (land breeze) with relatively low wind speeds (< 3 m/s). At about 06:00 CST, winds shift to the W and then to the N directions at about 10:00 CST reflecting the prominent synoptic flow overpowering a bay breeze from the W direction.

NSL heights from the MPL have limitations due to low resolution and/or unreliable near ground measurements (See section 2.3 above), therefore the NSL heights measured by the MPL could be overestimated. Missing data from the MPL from 8:40-10:00 CST impedes detection of BL growth during this time, but measurements before and after the data gap show BLH measurements remaining near 240 m. As this site is surrounded by the Galveston Bay on three sides and is close to the shore, a BL evolution at this site could be similar to one over water and could account for the stable measurements observed.

The MPL continues to measures a shallow layer at ~270 m agl until approximately 13:00 CST, when the BLH rapidly increases to ~2200 m. This unusually

sharp BLH increase is explained with HSRL aerosol backscatter profiles (Figure 4.7a) showing aerosol backscatter at altitudes 1300-2000 m agl and extending from the inland area outwards to Smith Point. Here, BLHs are detected at the lowest gradient as this gradient is the strongest at this time (360 m agl) and the intruding aerosols are not yet directly above the Smith Point site. The HSRL 360 m agl BLH is slightly higher than the MPL BLHs at 250±18 m agl. Figure 4.7b shows the next measurements from the HSRL at about 15:00 CST, nearly an hour after Figure 4.7a. The intruding aerosols have now mixed to lower altitudes over Smith Point. This makes the BLH algorithms retrieve the BLH at the top of this layer (2055 m agl by the HSRL). This is consistent with the measurements taken by the MPL which as discussed earlier, sees a sharp increase in BLH at about 14:00-15:00 CST with a BLH about 2100 ± 46 m agl. Figure 4.7b also shows lower aerosol backscatter in low altitudes below the intruding aerosol backscatter. This might correspond to a thermal internal boundary layer (TIBL) below the incoming air above. A TIBL is created when cool onshore wind is heated over a land surface creating an internal boundary layer within the developing mixed layer (Garratt, 1990). As we define the aerosol backscatter BLHs as a strong negative gradient in aerosol backscatter, the clean (i.e., having lower aerosol backscatter) shallow layer is not identified as a BLH candidate. Wind profiler measurements from the nearby La Porte site show W/NW winds measured after 12:00 CST at altitudes above ~500 m indicating a return flow above the bay breeze (Figure 4.6b). As the HSRL travels from the La Porte towards the Smith Point site (Figures 4.7a and 4.7b) we can make a connection between these two sites and can conclude that the higher aerosol

backscatter over Smith Point can be attributed to a lofted return flow from land above the bay/sea breeze flow.

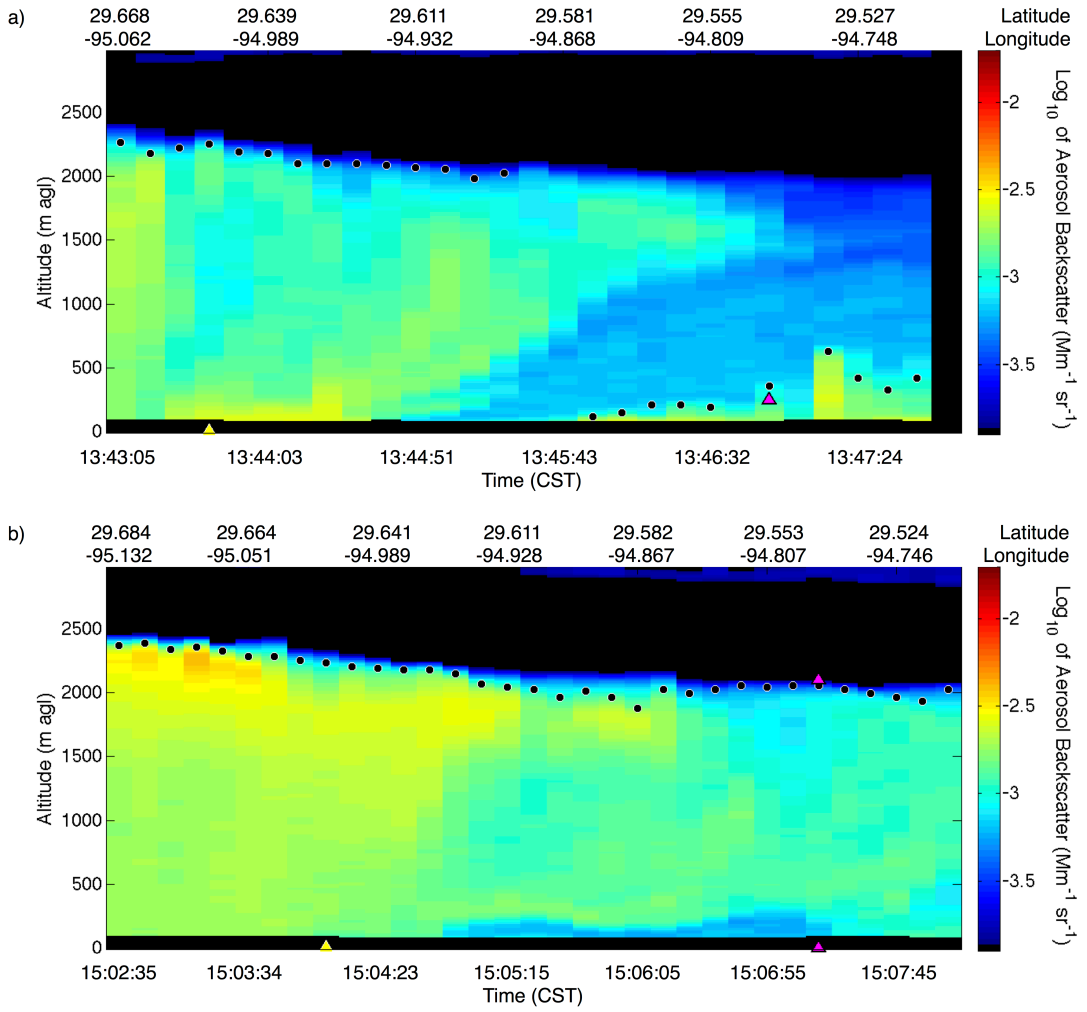

Figure 4.7. HSRL aerosol backscatter measured over Smith Point. Magenta triangles indicate measurements directly over Smith Point and the MPL BLH measured at this time. The yellow triangle indicates the La Porte site for reference. Measurements taken at about 13:45 CST are displayed in (4.7a) and measurements taken at about 15:05 CST in (4.7b).

4.1.3 La Porte

The TOPAZ at the La Porte site did not measure during the nighttime hours and started measurements at about 7:40 CST. The La Porte site is about 30 km NW of the Smith Point site on the western shore of Galveston Bay. Nighttime winds at La Porte

were measured from the N/NW directions with an average wind speed of 1.6 m/s until about 11:00 CST, when the onset of the bay breeze shifts winds to the E direction. Winds gradually shift to the SE as the gulf sea breeze arrives at La Porte (Figure 4.4c). BLHs detected by the TOPAZ in the early morning hours (7:00-08:00 CST) were identified at about 260 ±10 m agl however morning time fog during prevented the detection of the BLH from the TOPAZ from about 9:00 CST to 10:00 CST. After the fog dissipates the BLH measured by TOPAZ is at 1087 ±470 m agl about 11:00 CST (Figure 4.3). The higher BLH corresponds to a simultaneous increase in wind speed with the onset of the bay breeze (Figure 4.4d). As the yellow triangle indicating the La Porte site in Figures 4.7a shows, the BLH measured at 11:00 CST might be due to the lofted return flow. The top of the return flow creates a strong aerosol gradient and is identified as the BLH. This is also supported by the La Porte wind profiler data as it measures N/NW winds above the easterly bay breeze above 400 m agl. The BLH continues to grow and eventually reaches 1744 ±215 m in depth at 12:00 CST (Figure 4.3). BLHs after 12:00 CST are no longer considered, as the TOPAZ does not measure reliably aerosol backscatter above 2000 m and could therefore not measure BLHs higher than 2000 m. In fact, HSRL measurements over the La Porte site found BLHs of 2250 m agl and 2235 m agl at about 13:40 and 15:05, CST respectively.

4.4.1.4 University of Houston

Further inland, the UH CL31 is located approximately 28 km northwest from the La Porte site. Wind speeds at this site showed nighttime N/NW winds at an average of 1.1 m/s until about 17:00 CST, when winds start shifting to the S/SE directions and

wind speeds slightly increase to about 3-4 m/s (Figures 4.4e and 4.4f). This indicates that the sea breeze did not reach this most northern ground LIDAR site until about 17:00 CST. BLHs measured by the CL31 show NSL heights at an average of 209 ±47 m agl until about 8:00 CST when the BLH starts increasing. UH CL31 BLHs were highest among all ground LIDAR measurements reaching heights of 2200-2300 m agl.

4.4.2 Spatial evolution of the BLH

NSL heights measured by the Galveston CL31, UH CL31, and Smith Point MPL, (note: no nighttime TOPAZ measurements) show that Galveston has the shallowest NSL (on average 180 ±12 m deep). The earliest HSRL measurements are in the time frame 7:30-09:30 CST (Figure 4.8a) and show BLHs of 470± 64 m agl (over the Gulf of Mexico) and a decrease closer inland to 35±22 m agl. Over Galveston Island, the HSRL automatic BLH retrievals find the largest gradient at 390 m agl, yet the Galveston CL31 measures a BLH at 180±4 m agl. If the height detection limit is lowered for HSRL BLHs over Galveston, a similar BLH of 150 m agl is measured. By our definition of the BLH as being the largest aerosol gradient close to the surface, the 150 m heights are defined as the BLH. As can be seen in Figure 4.8a HSRL BLHs are fairly uniform over water at the Gulf of Mexico and Galveston Bay (460±28 m agl). They increase with increasing distance from the Bay and Gulf of Mexico. Outliers in HSRL BLHs were seen in some locations where multiple aerosol layering is present and cause a gradient at these heights (northernmost measurements in Figure 4.8a). The most inland ground site (UH) is the first to measure the start of the BL growth (at approximately 08:00 CST), followed closely by the Galveston CL31 and La Porte

TOPAZ showing BLH increases at about 09:00 CST (MPL does not show a significant BL increase until later in the day). The proximity to water is most likely responsible for the slight delay in growth times between the UH and both the Galveston and La Porte sites (Garrat, 1994).

The second HSRL loop starts at approximately 9:30 CST and finishes its trajectory at 11:00 CST (Figure 4.8b). HSRL measured BLHs over Galveston and Galveston Bay are at 430 ±53 m agl. BLHs during this HSRL loop are slightly more variable due to stratification of aerosol layers (Figure 4.8b) during the time the ML is developing and not yet well mixed. The last section of HSRL trajectory from the Houston downtown areas to the Gulf of Mexico show BLHs significantly higher than those measured during the first HSRL loop (about 700 m agl) and decrease again with closer proximity to the Gulf of Mexico). The HSRL does not measure again until about 12:30 CST and by this time most of the ground LIDARs have seen a sharp increase in the BLH (Figure 4.3).

Figure 4.8c and 4.8d show HSRL measurements from 13:00-16:00 CST when BLHs have significantly risen. The ML is well developed throughout the Houston area with increasing heights with increasing distance from bodies of water (both Galveston Bay and Gulf of Mexico) and with observed maximum heights in the NW corner of the HSRL measurements (Figures 4.8c and 4.8d). In Figure 4.8d BLHs in the Galveston Bay area are significantly higher than those in Figure 4.8c. This is explained by the aerosol backscatter measurements in Figures 4.5 and 7 (HSRL) where a land based return flow extends over Galveston Bay and its top is identified as the BLH.

According to the TCEQ CAMS network, a progressive shift to SE winds (sea breeze) occurred about 14:00 CST at the UHCC site, nearly 3 hours after this wind shift appeared at the Galveston site first (Figure 4.4a). Sites around the Galveston Bay first see a wind shift to the E (bay breeze), which gradually turns into SE by about 16:00 CST (Figure 4.4c). Further inland, at the UH site, winds shifted to SE at about 17:00 CST (Figure 4.4e) as did the remaining northwest of the Houston area, which observed a wind shift to the SE direction from 17:00-18:00 CST. The sea breeze shows its highest impact in the Galveston CL31 measurements: it prevents the full BL growth and eventually leads to an early (13:00 CST) BLH decrease at this site. The late arrival of the sea breeze does not seem to have a significant effect on the BLH over the Houston area as the ML has fully developed by the time of the arrival of the sea breeze (unlike the Galveston site case). The La Porte TOPAZ site experiences a strong bay breeze influence from the bay breeze which at the time of its onset, corresponds to a significant increase in the BLH.

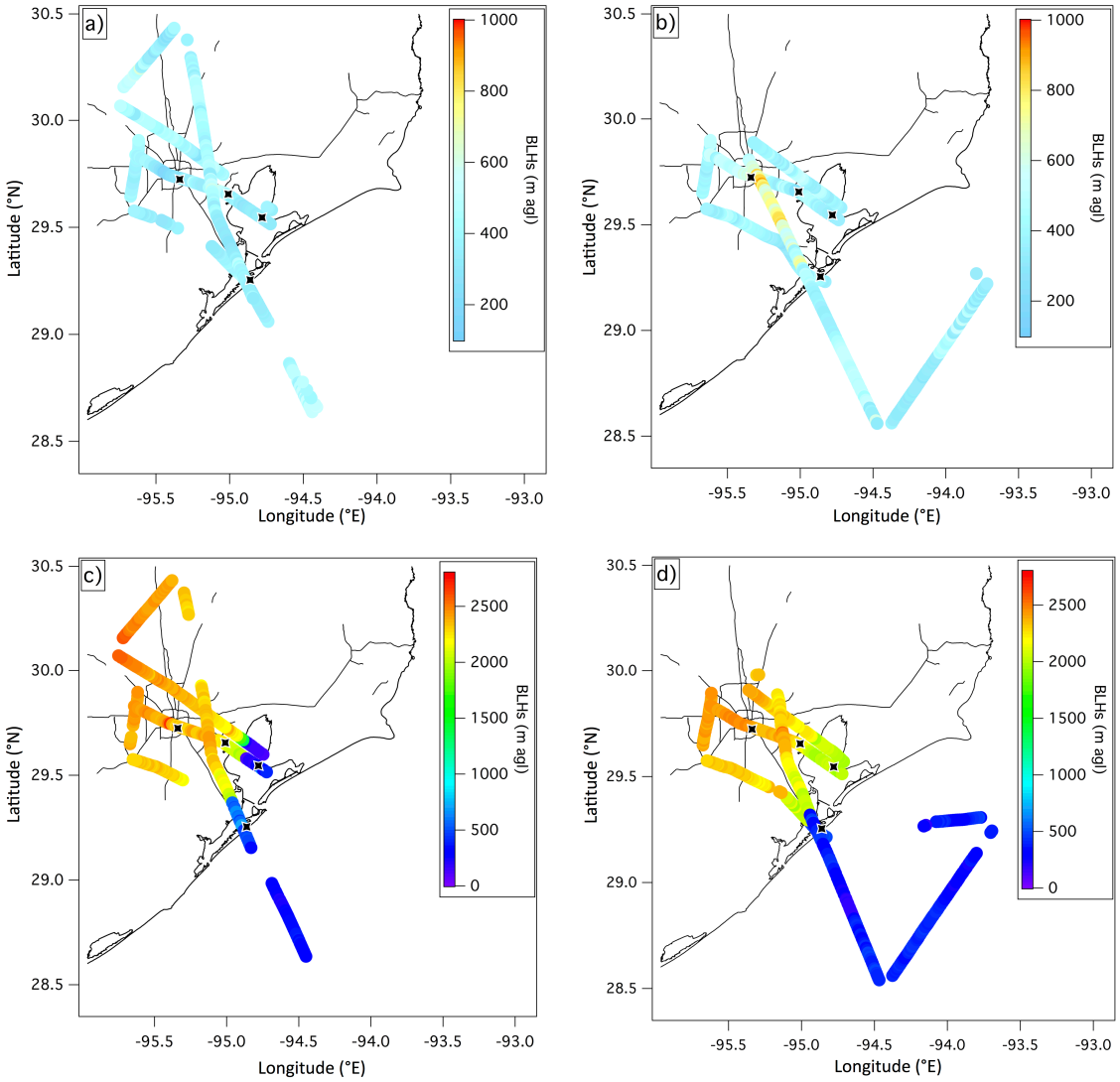

Figure 4.8. BLHs derived from the HSRL on September 25, 2013 divided by each Houston area loop at (a) 07:30-09:30, (b) 09:30-11:00, (c) 12:30-14:30, and (d) 14:30-16:00 CST.

4.4.3 Simulated BL Heights

Simulated BLHs were determined as described in Section 3.3. Here we use simulated near-surface air temperatures (at 2 m agl) as an indication of the surface sensible heat fluxes used to simulate the BLHs and compare them to observed TCEQ CAMs temperatures measured at about 10 m agl. The WRF near-surface temperature at

2 m are not directly simulated, but instead are a calculation between land surface temperature and the lowest model layer air temperature values. The model calculations of the 2 m air temperatures could contain some errors and lead to false biases when compared to observations (Hu et al., 2010). Here, we expect that the higher the near-surface temperatures, the greater the expected simulated surface fluxes and therefore the higher the modeled convective BLH (Hu et al., 2010; Steele et al., 2013). We also use the model 2 m agl near-surface temperatures and model SST as an indication of the temperature gradients used to determine the sea breeze (Pendergrass et al., 2010; Chen et al., 2011; Steele et al., 2013).

Figure 4.9 represents simulated BLHs and overlaid observations from the HSRL (no averaging was used for HSRL BLHs) measured in the hour of the model output (i.e. a 07:00 CST figure displays HSRL data measured from 07:00-07:59 CST). An over estimation with a bias of -508.6 m in the SW regions is seen in Figure 4.9c at 9:00 CST. No indication of an overestimation of near-surface temperatures were seen for this region.

Figures 4.9a-4.9h show a significant underestimation of simulated BLHs over the Gulf of Mexico with a bias of 199 m and mean simulated and observed BLHs of 162 m agl and 361 m agl respectively. Another significant underestimation (bias of 1854 m) of the BLH over the Galveston Bay is seen (Figures 4.9f and 4.9h) with mean simulated BLHs of 227 m agl and observed BLHs of 2081 m agl. This is most likely due to the observed return flow over this area that is identified as the BLH (see sections 4.1.2 and 4.1.3). Both model and observations see the highest BLHs in the NW areas with increasing distance from both the Gulf of Mexico and Galveston Bay.

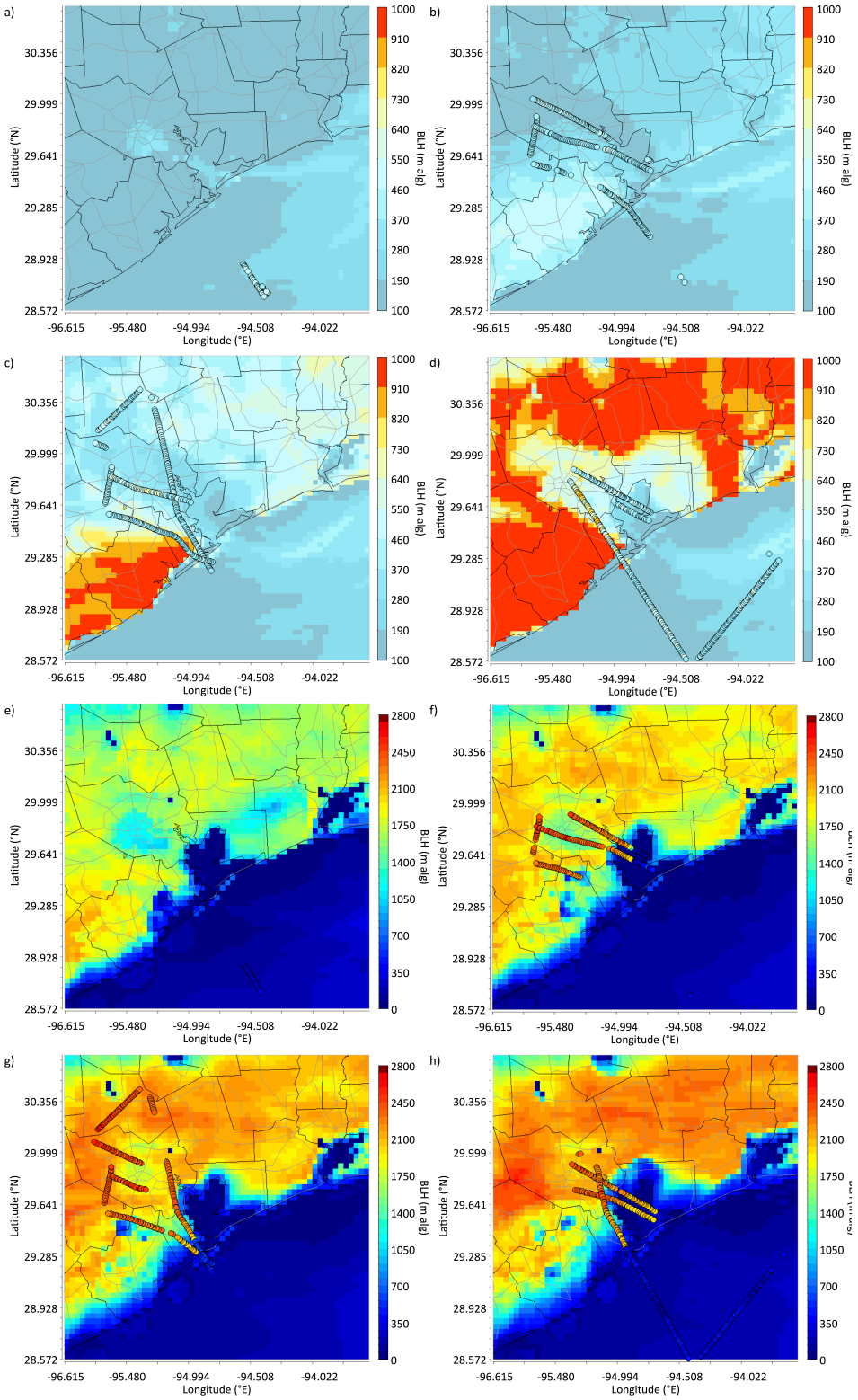

Figure 4.9. Model BLHs and corresponding HSRL BLHs measured at (a) 07:00, (b) 08:00, (c) 09:00, (d) 10:00 (e) 12:00, (f) 13:00, (g) 14:00, and (h) 15:00 CST.

Table 4.5 gives a summary of errors for the model with regard to corresponding observations. HSRL BLHs are used for BLH comparisons and TCEQ ground sites are used for near-surface temperature comparisons. Mean biases are calculated as the difference between observations and simulation results. Airborne HSRL BLHs were compared to the corresponding simulated BLH at the location of each HSRL measurement (note that multiple HSRL measurements can fall into the same grid cell). The simulated boundary layer height at each observation location was chosen at the hour of the measurements (i.e., a 14:30 CST measurement from the HSRL was compared to a 14:00 CST simulated BLH at the same location as the HSRL measurement). No averaging is applied to aircraft BLH observations as this would also create a spatial averaging of the BLH. Temperature observations are hourly averaged and then compared to the model results.

Table 4.5. Overall statistical analysis of simulated and observed near-surface temperatures and BLHs. Correlation coefficient (r), root-mean-square error (RMSE), mean absolute error (MEA), mean bias, mean values, and number of comparison points (No.) are shown.

Parameter	***r***	**RMSE**	**MEA**	**Mean Bias**	**Mean Observed**	**Mean Model**	**No.**
Near-surface air Temperatures	0.88	4.0	3.2	0.5	27.4	27.9	1008
BLHs	0.86	554.8	374.9	309			1597

Overall, model BLHs were lower than those measured by the HSRL with a bias of 309 m. These results are similar to those found by Scarino et al. (2014) who compared HSRL BLHs and WRF simulated BLHs using the Mellor–Yamada–Janjic´ BL scheme. The WRF BLHs over predictions were attributed to differences in the morning time BL growth rates and difficulties in the simulation of the BLH over

complex terrains. However, Scarino et al. (2014) did not observe (simulated or observed) thermodynamic physical processes. In contrast, the results presented here, showed that the YSU BLH under predictions were accompanied by an under prediction of near-surface temperature during daytime hours, which likely explains the under prediction of the BLHs as an underestimation of surface heat fluxes (Table 4.5 and 7). During nighttime hours however, the simulated near-surface temperatures were over predicted (bias of -2.3 to -1.3 °C). From 07:00-13:00 CST, the model under predicts near-surface temperatures, with the highest under predictions from ~08:00-10:00 CST (bias 1.2-1.6 °C).

Table 4.6. Correlation coefficient (*r*), root-mean-square error (RMSE), mean absolute error (MEA), number of BLHs compared (No.), and mean bias are calculated for hourly simulated and observed BLHs and near-surface temperatures (T) for 42 ground stations.

Hour (CST)	*r*	RMSE (m)	MAE (m)	BLH Mean Bias (m)	No. (BLHs)	T Mean Bias (°C)
7	-0.53	301.8	292.6	292.6	27	0.2
8	-0.2	206	179.7	159.2	222	1.5
9	-0.31	242	195.5	-28	289	1.6
10	0.4	273.1	232.3	102.5	277	1.2
12	0.26	197.8	191.1	191.1	40	0.6
13	0.79	818.5	679.7	674.8	175	0.3
14	0.88	545.2	451.6	449.8	262	-0.1
15	0.71	907.8	619.1	617.4	305	-0.4

Table 4.6 shows hourly correlations and errors between observations and simulated BLHs and near-surface temperatures. Table 4.7 lists the corresponding hourly maximum and minimum simulated and observed BLHs and near-surface temperatures. Hourly bias between observed and model BLHs (Table 4.6) show an under prediction of BLHs for all but one hour of measurements (09:00 CST) where an over estimation of BLHs is

seen over the SW regions in Figure 4.9c. The largest under prediction in near-surface temperatures are seen in the morning hours (two hours after sunrise) from 08:00 to 10:00 CST during the beginning of the BL growth. These times are vital to the development of the BLH as an under prediction of surface heat fluxes during the morning time ML growth will limit the vertical mixing of a convective ML and therefore underestimate the BLH. This underestimation during growth times could hinder the subsequent daytime BLHs (Snyder and Strawbridge, 2004). Negative correlations of *r* from -0.5 to -0.2 are seen during morning hours (07:00-08:00 CST see Figures 4.9a-4.9c) indicating a weak negative correlation during these times. Correlations increase later in the day (*r* from 0.71-0.88 after 12:00 CST) along with a more developed and well mixed BL.

Table 4.7. Maximum and minimum observed (OBLH) and modeled (MBLH) BLHs (in meters and °C respectively) by hour and corresponding near-surface air temperatures for both observations and model results.

Hour (CST)	**Max OBLH**	**Min OBLH**	**Max MBLH**	**Min MBLH**	**No. BLH**	**Max OT**	**Min OT**	**Max MT**	**Min MT**	**Mean OT**
7	555	375	215	167	27	27	20.8	26.1	18.8	24.3
8	615	135	480	120	222	30.3	23.9	27.9	22.2	27.2
9	675	255	951	23	289	32.4	26.7	29.9	25	29.1
10	900	285	1285	16	277	34.3	28.6	31.5	26.4	30.8
12	405	210	146	65	40	34	30.4	33.9	26.2	32.8
13	2670	120	2115	15	175	34.7	31	34.7	25.9	33.2
14	2595	345	2307	64	262	35	30.7	35.6	25.9	33.5
15	2535	180	2209	22	305	35.4	30.4	36.3	26.1	33.4

It is important to note that statistics given in Tables 5, 6, and 7 are taken over the HSRL flight tracks, therefore they cover both land and water measurements. Large differences between simulated and observed BLHs can be due to the land mask and land cover classifications. The model simulations will assign a water/land mask identity to

each grid cell, and a respective land cover classification (e.g., urban land, grassland, water body, mixed forest, etc.). Areas near bodies of water are typically impacted by this classification as the near-water classification can be assigned too far inland. This will make simulations underpredict near-surface temperatures and BLHs, e.g. in Figure 4.9g and 4.9h near the Gulf of Mexico coast. When these are compared to the observed BLHs a large uncertainty is calculated (e.g., hours 13, 14 and 15 in Tables 6 and 7). No mean values are calculated for BLHs as they contain both water and land-based BLHs and a mean value would not be representative of a BLH over the entire study area.

The buoy SST data from the U.S. National Data Buoy Center (http://seaboard.ndbc.noaa.gov) within the simulation domain (one buoy available) was averaged to a daily value to compare with sea surface temperatures (SST) used by the model. The default treatment of SST in WRF involves assigning the input SST field (from NARR 32 km input data) to corresponding water grid cell points in the model domain, therefore SST at each grid cell does not vary with time over the entire model run. Here we use the closest grid cell to the buoy location. Model SST was slightly higher (25.8 °C) than daily averaged observed SST of 22.6°C over the Gulf of Mexico. An under estimation of land surface temperatures combined with an overestimation of SSTs create a smaller gradient between land/sea temperatures leading to a weaker simulated sea breeze. The model simulated a slightly earlier onset of the sea breeze and faster movement of the sea breeze front inland compared to observations (Figures 4.4.4a, 4.4c, and 4.4e). This early onset might be explained by higher simulated wind speeds (Figures 4.4.4b, 4.4d, and 4.4f) leading to a quicker movement of the sea breeze inland. The overestimation of surface winds over the Gulf of Mexico and the coastal zones in

the Houston area has been documented earlier (Czader et al., 2013; Li and Rappenglück, 2014).

Time series of simulated BLHs and ground LIDAR measurements are displayed in Figure 4.10. These show reasonably good agreement between observations and simulated BLHs in the Galveston, La Porte, and UH sites. Overall, peak BLHs are underestimated by the model at all ground sites. However, a few differences in the ML growth were observed. The early growth of the Galveston BL (~1 hour) is associated with an early onset of simulated sea breeze. The UH BLH however, is simulated with a slower growth, which could be attributed to under estimated surface temperatures that indicate an underestimation of surface heat fluxes used to simulate the BLH. The La Porte BLHs correlate well with the modeled heights. However the TOPAZ La Porte measurements are limited to 2000 m agl hence the observed La Porte BLHs displayed here are also under estimated (see Section 4.2.2).

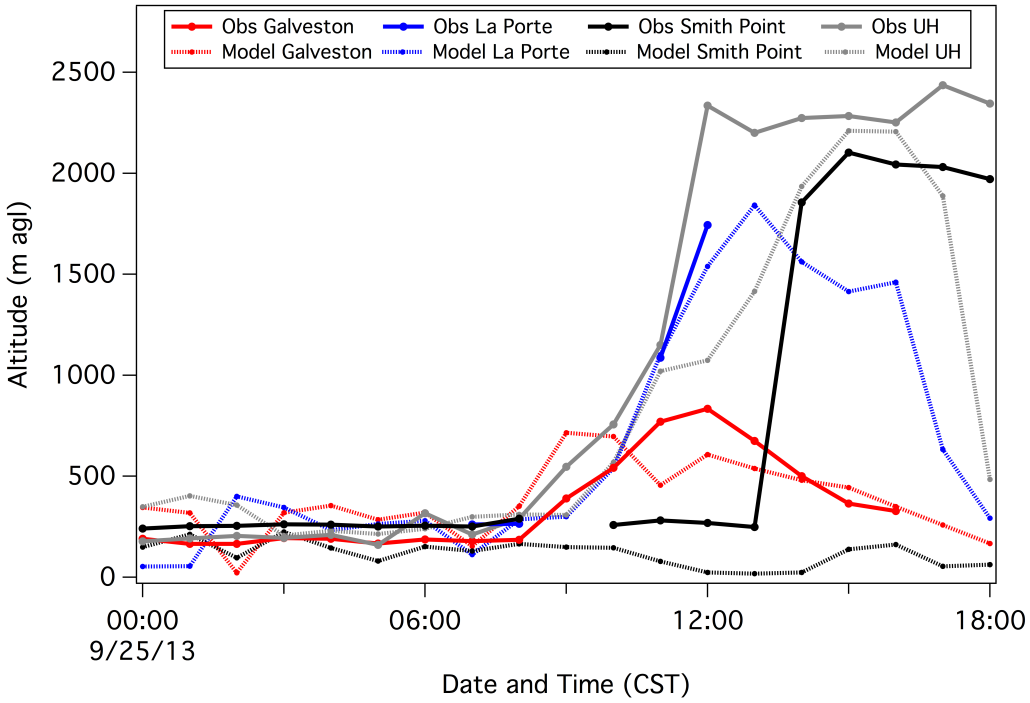

Figure 4.10. Ground LIDAR BLHs and simulated BLHs at each ground site for September 25, 2013.

The modeled BLH at the Smith Point site shows the least similarity to the observed BLHs. The proximity to water at this location and the shape of this land mass is expected to have lower and more stable BLHs compared to inland areas, as is seen in the modeling results (Figure 4.10). However, the MPL at Smith Point measured a sharp increase in the BLH, when a strong return flow moved air masses with higher BLHs and higher aerosol backscatter over that site. This return flow is in fact, simulated by the model yet the BLH remains at low altitudes. This is a result of the different methods for determining BLHs used in observations and the BL schemes (McElroy and Smith, 1991; Seibert et al. 2000). In this case, the observed BLHs are calculated at the top of the lofted return flow (largest aerosol gradient) while the model identifies the BLH as the level of lowest surface heat fluxes.

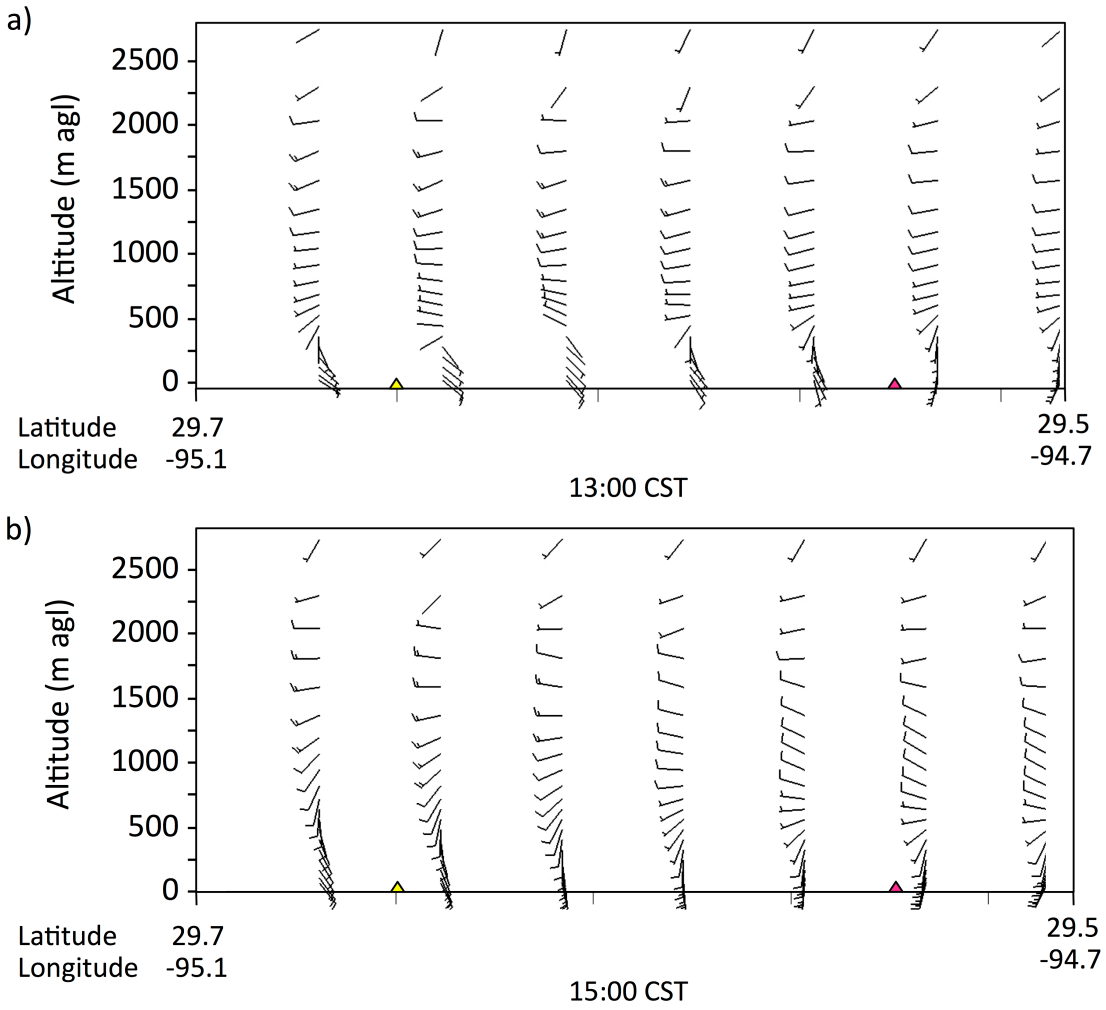

Figure 4.11. Simulated vertical wind profiles over similar HSRL trajectories in Figure 4.7. Yellow triangle indicates the La Porte site and magenta triangle indicates the Smith Point site for reference. Wind profile simulations at 13:00 CST are displayed in (a) and simulations at 15:00 CST in (b).

Figure 4.11 shows WRF vertical wind profiles closest to the HSRL trajectories in Figure 4.7. WRF wind profiles display a return flow at altitudes from about 300 m to 2000 m agl in Figures 4.11a and 4.11b. Above the return flow a different wind direction is seen (SW). The top of the return flow is simulated slightly lower than HSRL observations (2200 m agl) over the La Porte wind profiler (Figure 4.6b). Both observed and simulated wind profiles exhibit two distinct layers with tops indicated by wind

shear. The first layer being the near-surface sea breeze flow, and the second layer being the lofted return flow above. This reveals that the aerosol backscatter derived BLHs measured by the HSRL are identified as the top of the return flow layer, while the thermodynamically derived BLHs simulated by the model are identified as the top of the sea breeze flow. As Figures 4.7a and 4.7b show, high aerosol backscatter signals are measured at both layers and a gradual vertical mixing is happening between the two layers from measurements taken in Figure 4.7a to Figure 4.7b. However, a chemistry coupled model simulation might not simulate appropriate pollutant mixing between and within the two distinct layers as the thermodynamically derived top of the lowest layer is identified as the BLH.

As discussed previously, various studies have shown that the sea/land breeze circulation can transport both freshly emitted pollutants and aged air masses leading to increased pollutant concentrations compared to background marine air masses (Banta et al., 2005; Day et al., 2005; Rappenglueck et al., 2008; Ngan et al., 2012; Li and Rappenglueck, 2014). This occurs when the convergence of large-scale flows and the sea breeze flow create a period of stagnation over emission sources that allow for the accumulation and photochemical reaction of pollutants. These freshly polluted air masses are then transported inland by the sea breeze and lead to increased pollutant concentrations. The nighttime land breeze in turn will carry these polluted air masses back over water (here the Gulf of Mexico) where pollutants such as ozone are less-efficiently removed. The following day's sea breeze can then return these aged air masses inland once again, increasing background concentrations and leading to overall higher pollutant concentrations (Banta et al., 2005; Day et al., 2005; Rappenglueck et

al., 2008; Li and Rappenglueck, 2014). A similar situation is observed in this study as both sea breeze and lofted return flow show high aerosol backscatter signals (indicative of high particulate concentrations). The combination of the two flows containing high aerosol backscatter signals could contribute to overall high pollutant concentrations.

4.5 Summary and Conclusions

This case study used multiple ground-based aerosol backscatter LIDARs and one airborne LIDAR deployed on September 25, 2013 as part of the DISCOVER-AQ campaign to study the boundary layer spatial and temporal evolution over the southeast Texas region. Ground-based LIDARs included two ceilometers on the University of Houston Campus and Galveston Island, an elastic MicroPulse LIDAR at Smith Point, a Tunable Optical Profiler for Aerosol and oZone (TOPAZ) at La Porte, and an airborne high-spectral resolution LIDAR (HSRL). Conditions for the case study were favorable for high ozone concentrations as clear skies, low wind speeds, and a sea breeze circulation prevailed. Observed BL heights (spatially and temporarily) were compared with those simulated by the Advanced Research Weather Research and Forecast (ARW-WRF) model version 3.7 using the Yonsei University (YSU) boundary layer scheme, to observe modeled sea breeze circulation and its influences on the BLH and evolution.

Surface wind and near-surface air temperature measurements, were used to study the inland progression of the sea breeze and its possible effects on the BLH. No impacts on the observed BLHs could be found as the inland progression of the sea breeze happened in the afternoon hours when the BL was fully developed. The only

exception was the Galveston Island site; as the sea breeze strengthened, the BLH decreased in the early afternoon (13:00 CST) as marine air was pushed inland.

A lofted return flow was observed with HSRL and wind profiler measurements, with HSRL showing elevated aerosols backscatter signals within the return flow. These lofted aerosols were observed to mix downward to near-surface altitudes at the Smith Point and La Porte sites (Figures 4.7a and 4.7b) in the early afternoon hours, while they remained lofted over the Galveston site (Figures 4.5a and 4.5b). Aerosol retrieval methods identified the top of the return flow as the BLH over the Smith Point and La Porte sites (~2200 m agl), while the Galveston BLH was measured below the lofted return flow (~900 m agl). The most inland location (UH campus) experienced the fastest morning time growth, whereas the coastal site (Galveston) showed the slowest BL growth (Figure 4.3). BLHs measured by the HSRL showed the highest BLHs in the most northwestern regions (Figures 4.8c and 4.8d).

WRF simulations displayed an overall underestimation of BLHs with a larger bias over water surfaces (bias 199 m) compared to land surfaces (bias of 309 m). The underestimation of BLHs was attributed to under predicted surface heat fluxes indicated by under predicted near-surface air temperatures compared to observations. Lower BLH correlation coefficients between HSRL BLHs and simulated BLHs were found during morning hours from about 07:00-09:00 CST ($-0.5 \leq r \leq -0.2$) but increased as the ML fully developed in the early afternoon hours ($0.71 \leq r \leq 0.88$).

An earlier inland onset of the sea breeze was also simulated by WRF with slightly higher wind speeds (bias -1.5 m/s) than those measured by ground stations. As the strength and progression of the sea breeze is simulated from land-to-sea temperature

gradients in WRF, we used observed and simulated sea surface temperature (SST) and near-surface air temperatures over land to compare observation and model land-to-sea temperature gradients, this approach however, could have some limitations. Results showed comparable yet slightly higher SST values in the model, but lower simulated near-surface air temperatures over land. A lower land-to-sea temperature gradient would indicate an under prediction of the sea breeze strength. However, the inland progression of the simulated sea breeze was seen earlier than the observations. An earlier inland onset of the simulated sea breeze is expected to simulate lower BLHs as cool marine air may impede the ML growth, and could explain the lower simulated BLHs.

Due to the different methods used to calculate the BLH (thermodynamically in WRF simulations versus aerosol backscatter gradients for LIDARs) large biases were calculated for marine BLHs (up to 400 m) and in cases where the top of the aerosol loaded return flow was identified as the BLH by LIDAR platforms (bias of 1854 m). In the later cases, aerosols are well mixed within the aerosol derived BLH (Figure 4.7) and therefore aerosol derived BLHs are more representative of the convective mixed layer height than the thermodynamically derived BLHs by WRF. Although not shown here, La Porte measured the highest ozone mixing ratios on September 25, 2013 with an hourly average of 151 ppbv at 13:00 CST as measured by the local TCEQ CAMS monitoring station. According to Banta et al. (2005) and Darby et al. (2005), the stagnation period during early- to mid-afternoon hours that happens as large-scale offshore flow converges with the local sea breeze, favors the accumulation of pollutants over emission sources and will eventually lead to higher pollutant concentrations. The

duration of this stagnation period (>1 hour), the location (over emission sources), and timing (around noon/early afternoon) of the stagnation zone are key to allow the emissions to accumulate and chemically react. The late inland onset of the sea breeze is also critical for the accumulation of pollutants. These high pollutant concentrations can then be transported further inland by the sea breeze (Banta et al., 2005; Darby et al., 2005; Ngan et al., 2012). The results of this study imply that both the thermodynamic BLH and the aerosol backscatter BLH provide the complete extent of vertical mixing of pollutants.

5 Conclusions

The extent of the vertical mixing of pollutants given by the boundary layer height (BLH) is a vital parameter in air quality monitoring and air-quality modeling. Although the BLH is key for atmospheric studies, it is seldom continuously monitored. For this reason, we use remote sensing instruments such as Light Detection And Ranging (LIDAR) sensors that can monitor and measure the BLH uninterruptedly. This study aims to efficiently monitor and capture the temporal, season, and spatial BL evolution using aerosol LIDARs platforms, and ultimately use observations to aid in the simulation of BLHs for air quality modeling.

The first task (Chapter 2) presents aerosol backscatter derived boundary layer heights from three distinct retrieval methods were tested and compared to radiosonde derived BLHs. An aerosol gradient method, a cluster analysis method, and a Haar wavelet method were compared to daytime radiosonde profiles using aerosol backscatter from a Vaisala CL31 ceilometer. Overall good agreement was found for all comparisons yet all methods found cases where radiosonde thermodynamic BLHs did not strongly correlate with a maximum aerosol gradient due to differences in thermodynamic and aerosol BLHs and the method used to estimate these heights. The aerosol gradient method showed difficulties in determining the BLH in low aerosol backscatter conditions. The cluster method showed drawbacks due to sensitivity to noise generated artifacts and/or lofted aerosol layers where the algorithm calculated peaks in variance and incorrectly identified them as the BLH. The wavelet method showed the best agreement of all methods tested, with 77.5% of cases showing

excellent agreement with radiosonde BLHs without requiring a previous knowledge of the BL. The wavelet method also showed a higher ability of calculating the BLH under low aerosol conditions where the aerosol gradient method and cluster methods were not able to resolve a BLH.

BLH detection in the presence of cloud signals showed a clear difference between the negative gradient methods (aerosol backscatter and wavelet methods) and the cluster analysis method. Both aerosol gradient and wavelet methods identify the BLH as the top of the cloud layer (sharp negative gradient) while the cluster method identified the BLH as the base of the cloud layer.

The results presented in Chapter 2 demonstrate the ability of the Haar Wavelet method to more accurately detect BLHs than the other two methods tested, while requiring the least amount of manual inspection. However, this method requires the careful determination of dilation values dependant on instrumentation and location. Chapter 2 results were implemented in both Chapters 3 and 4 as it was determined that the Haar wavelet method could be successfully used for automated long-term seasonal and diurnal boundary layer studies and spatial analysis of the BL using aerosol LIDARs.

Chapter 2 presents aerosol backscatter derived boundary layer heights measured at a coastal site in Southeast Texas. Continuous aerosol backscatter measurements from September 1, 2013 to September 30, 2016 retrieved by a Vaisala CL31 ceilometer were used. Daily evolution of aerosol backscatter BLHs were divided into four scenarios (A, B, C, and D) of similar heights, evolution, associated surface wind measurements and

Hybrid Single-Particle Lagrangian Integrated Trajectory model (HYSPLIT) backward trajectories.

BLHs were found to be relatively low (~400-600 m agl) in scenarios A and B and associated with light to moderate wind speeds (<7 m/s) from the S/SE directions, while higher BLHs (up to ~1100 m agl) occurred in scenarios C and D with high wind speeds (>7 m/s) from the N/NW directions. The most important finding however was the increase in wind speeds during the morning hours that correlated strongly with the gradual connection between the NSL and ML in scenarios B and D. Scenarios A (19.9% of days) and C (13.6% of days) were the most frequently measured scenarios in the summer and winter months, respectively. Scenarios B and D were less frequent (3.8 and 2.6 % of days, respectively) and mostly occurred in the winter and fall months respectively.

Additionally, as BLHs did not show a strong correlation to backward trajectories, it can be concluded that over a coastal area the local circulations (such as the land-sea breeze circulation) might largely modify turbulent properties of advected air masses and consequently be more influential in the development of the BLHs than the air mass type. The case study revealed a stratified coastal boundary layer with aerosol layer tops corresponding to layers measured in the radiosonde profiles that were not only specific to aerosol backscatter measurements, but also corresponds to thermodynamically derived layers measured by sounding data.

Chapter 3 used multiple aerosol ground LIDARs including an airborne LIDAR deployed on September 25, 2013 as part of the Deriving Information on Surface conditions from Column and Vertically Resolved Observations Relevant to Air Quality

(DISCOVER-AQ) campaign to observe the boundary layer spatial and temporal evolution over the southeast Texas region. Four ground LIDARs and an airborne high-spectral resolution LIDAR (HSRL) were used for BLH detection. This study also compared observed BL heights with those simulated by The Advanced Research Weather Research and Forecast (ARW-WRF) model version 3.7 using the Yonsei University (YSU) boundary layer scheme. This modeling platform was further used to observe the simulated sea breeze circulation and examine its influences on the BLH and evolution.

No impacts on the observed BLHs could be found as the inland progression of the sea breeze happened in the afternoon hours when the BL was fully developed. The only exception was the Galveston Island site, which exhibited decreasing BLHs as marine air was pushed inland. A lofted return flow was observed with HSRL and wind profiler measurements, with HSRL showing elevated aerosols backscatter signals within the return flow. These lofted aerosols were observed to mix downward to near-surface heights at the Smith Point and La Porte sites, while remaining aloft over the Galveston site. The most inland location (UH campus) experienced the fastest morning time growth, whereas the coastal site (Galveston) showed the slowest BL growth. BLHs measured by the HSRL showed the highest BLHs in the most north-western Houston regions.

WRF simulations displayed an overall underestimation of BLHs with a larger bias over water surfaces compared to land surfaces. The underestimation of BLHs was attributed to under predicted surface heat fluxes indicated by under predicted near-surface air temperatures compared to observations. An earlier inland onset of the sea

breeze was also simulated by WRF with slightly higher wind speeds than those observed. An early inland onset of the simulated sea breeze is likely to simulate lower BLHs as cool marine air may impede the ML growth, and could explain the lower simulated BLHs.

Lastly, due to the different methods used to calculate the BLH, in this study thermodynamically in WRF simulations and using aerosol backscatter gradients for LIDARs, large biases were calculated for marine BLHs during cases where the top of the aerosol loaded return flow was identified as the BLH by LIDAR platforms. Overall, the results of this study imply that both the thermodynamic BLH and the aerosol backscatter BLH provide the complete extent of vertical mixing of pollutants.

6 References

Alvarez, R. J., Senff, C. J., Langford, A. O., Weickmann, A. M., Law, D. C., Machol, J. L., Merritt, D. A., Marchbanks, R. D., Sandberg, S. P., Brewer, W. A., Hardesty, R. M., Banta, R. M. (2011). Development and Application of a Compact, Tunable, Solid-State Airborne Ozone Lidar System for Boundary Layer Profiling. J. Atmos. Ocean. Tech., 28(10), 1258–1272, doi.org/10.1175/JTECH-D-10-05044.1

Alvarez, R. J., Senff, C. J., Weickmann, A. M., Sandberg, S. P., Langford, A. O., Marchbanks, R. D., Brewer, W. A., and Hardesty, R. M. (2012). Reconfiguration of the NOAA TOPAZ lidar for ground-based measurement of ozone and aerosol backscatter, Proceedings of the 26th International Laser Radar Conference, Porto Heli, Greece.

Anderberg, M. R. (1973). Cluster Analysis for Applications, Academic Press.

André , J. C. and Mahrt, L. (1982). The Nocturnal Surface Inversion and Influence of Clear-Air Radiative Cooling, J. Atmos. Sci., 39, 864– 878.

Angevine, W. M., Tjernström, M., and Žagar, M. (2006). Modeling of the Coastal Boundary Layer and Pollutant Transport in New England. J. Appl. Meteorol. Clim., 45(1), 137–154, doi.org/10.1175/JAM2333.1

Baars, H., Ansmann, A., Engelmann, R., and Althausen, D. (2008). Continuous monitoring of the boundary-layer top with lidar, Atmos. Chem. Phys., 8, 7281–7296, doi:10.5194/acp-8-7281-2008.

Balsley, B. B., Lawrence, D. A., Woodman, R. F., and Fritts, D. C. (2013). Fine-Scale Characteristics of Temperature, Wind, and Turbulence in the Lower Atmosphere (0–1,300 m) Over the South Peruvian Coast. Bound.-Lay. Meteorol., 147(1), 165–178, doi.org/10.1007/s10546-012-9774-x

Banta, R. M., Senff, C. J., Nielsen-Gammon, J., Darby, L. S., Ryerson, T. B., Alvarez, R. J., Sandberg, S. P., Williams, E. J., and Trainer, M. (2005). A Bad Air Day in Houston. Bull. Am. Meteorol. Soc., 86(5), 657–669, doi.org/10.1175/BAMS-86-5-657

Banta, R. M., Senff, C. J., White, A. B., Trainer, M., McNider, R. T., Valente, R. J., Mayor, S. D., Alvarez, R. J., Hardesty, R. M., Parrish, D., and Fehsenfeld, F. C. (1998). Daytime buildup and nighttime transport of urban ozone in the boundary layer during a stagnation episode. J. Geophys. Res.-Atmos., 103(D17), 22519–22544, doi.org/10.1029/98JD01020

Bao, J. W., Michelson, S. A., McKeen, S. A., and Grell, G. A. (2005). Meteorological evaluation of a weather-chemistry forecasting model using observations from

the TEXAS-AQS 2000 field experiment. J. Geophys. Res.-Atmos., 110(D21), D21105, doi.org/10.1029/2004JD005024

Berkoff, T. A., Welton, E. J., Campbell, J. R., Scott, V. S., and Spinhirne, J. D. (2003). Investigation of overlap correction techniques for the Micro-Pulse Lidar NETwork (MPLNET). Proc. Geoscience and Remote Sensing Symp. 2003, IGARSS'03, Toulouse, France, IEEE International, Vol. 7, 4395–4397, doi.org/10.1109/IGARSS.2003.1295527

Berman, S., Ku, J. Y., and Rao, S. T. (1999). Spatial and temporal variation in the mixing depth over the northeastern United States during the summer of 1995, J. Appl. Meteor., 38, 1661–1673.

Biavati, G., Feist, D. G., Gerbig, C., and Kretschmer, R. (2015). Error estimation for localized signal properties: application to atmospheric mixing height retrievals, Atmos. Meas. Tech., 8, 4215– 4230, doi:10.5194/amt-8-4215-2015.

Brooks, I. M. (2003). Finding Boundary Layer Top: Application of a Wavelet Covariance Transform to Lidar Backscatter Profiles, J. Atmos. Ocean. Tech., 20, 1092–1105.

Caicedo, V., Rappenglueck, B., Lefer, B., Morris, G., Toledo, D., and Delgado, R. (2016). Comparison of aerosol LIDAR retrieval methods for boundary layer height detection using ceilometer backscatter data, Atmos. Meas. Tech. Discuss., doi:10.5194/amt-2016-340.

Calmet, I., and Mestayer, P. (2016). Study of the thermal internal boundary layer during sea-breeze events in the complex coastal area of Marseille. Theor. Appl. Climatol., 123(3–4), 801–826, doi.org/10.1007/s00704-015-1394-1

Campbell, J. R., Hlavka, D. L., Welton, E. J., Flynn, C. J., Turner, D. D., Spinhirne, J. D., Scott, S. V., and Hwang, I. H. (2002). Full-Time, Eye-Safe Cloud and Aerosol Lidar Observation at Atmospheric Radiation Measurement Program Sites: Instruments and Data Processing. J. Atmos. Ocean. Tech., 19(4), 431–442, doi.org/10.1175/1520-0426(2002)019<0431:FTESCA>2.0.CO;2

Chen, F., Miao, S., Tewari, M., Bao, J.-W., and Kusaka, H. (2011). A numerical study of interactions between surface forcing and sea breeze circulations and their effects on stagnation in the greater Houston area. J. Geophys. Res.-Atmos., 116(D12), D12105, doi.org/10.1029/2010JD015533

Cohen, A. E., Cavallo, S. M., Coniglio, M. C., and Brooks, H. E. (2015). A Review of Planetary Boundary Layer Parameterization Schemes and Their Sensitivity in Simulating Southeastern U.S. Cold Season Severe Weather Environments. Weather and Forecast., 30(3), 591–612, doi.org/10.1175/WAF-D-14-00105.1

Cohn, S. and Angevine, W. (2000). Boundary layer height and entrainment zone thickness measured by lidars and wind-profiling radars, J. Appl. Meteor., 39, 1233–1247.

Compton, J. C., Delgado, R., Berkoff, T. A., and Hoff, R. M. (2013). Determination of Planetary Boundary Layer Height on Short Spatial and Temporal Scales: A Demonstration of the Covariance Wavelet Transform in Ground-Based Wind Profiler and Lidar Measurements, J. Atmos. Ocean. Tech., 30, 1566–1575, doi:10.1175/JTECH-D-12-00116.1.

Coniglio, M. C., Correia, J., Marsh, P. T., and Kong, F. (2013). Verification of Convection-Allowing WRF Model Forecasts of the Planetary Boundary Layer Using Sounding Observations. Weather and Forecasting, 28(3), 842–862, doi.org/10.1175/WAF-D-12-00103.1

Cuchiara, G. C., Li, X., Carvalho, J., and Rappenglück, B. (2014). Intercomparison of planetary boundary layer parameterization and its impacts on surface ozone concentration in the WRF/Chem model for a case study in Houston/Texas. Atmos. Environ., 96, 175–185, doi.org/10.1016/j.atmosenv.2014.07.013

Czader, B. H., Li, X., and Rappenglück, B. (2013). CMAQ modeling and analysis of radicals, radical precursors, and chemical transformations. J. Geophys. Res.-Atmos., 118(19), 11,376-11,387, doi.org/10.1002/jgrd.50807

Darby, L. S. (2005). Cluster Analysis of Surface Winds in Houston, Texas, and the Impact of Wind Patterns on Ozone. J. Appl. Meteorol., 44(12), 1788–1806, doi.org/10.1175/JAM2320.1

Davis, K. J., Gamage, N., Hagelberg, C. R., Kiemle, C., Lenschow, D. H., and Sullivan, P. P. (2000). An objective method for deriving atmospheric structure from airborne lidar observations, J. Atmos. Ocean. Tech., 17, 1455–1468.

Day, B. M., Rappenglück, B., Clements, C. B., Tucker, S. C., and Brewer, W. A. (2010). Nocturnal boundary layer characteristics and land breeze development in Houston, Texas, during TexAQS-II, Atmos. Environ., 44, 4014–4023, doi:10.1016/j.atmosenv.2009.01.031.

Draxl, C., Hahmann, A. N., Peña, A., and Giebel, G. (2014). Evaluating winds and vertical wind shear from Weather Research and Forecasting model forecasts using seven planetary boundary layer schemes. Wind Energy, 17(1), 39–55, doi.org/10.1002/we.1555

de Bruine, M., Apituley, A., Donovan, D., Klein Baltink, H., and de Haij, M. (2016). Pathfinder: Applying graph theory for consistent tracking of daytime mixed layer height with backscatter lidar, Atmos. Meas. Tech. Discuss., doi:10.5194/amt-2016-327.

de Haij M., Wauben W., and Baltink, H. K. (2006). Determination of mixing layer height from ceilometer backscatter profiles, Proc. SPIE 6362, 63620R-63620R-12, doi:10.1117/12.691050.

Di Giuseppe, F., Riccio, A., Caporaso, L., Bonafé, G., Gobbi, G. P., and Angelini, F. (2012). Automatic detection of atmospheric boundary layer height using ceilometer backscatter data assisted by a boundary layer model, Q. J. Roy. Meteorol. Soc., 138, 649–663, doi:10.1002/qj.964.

Emeis, S., Münkel, C., Vogt, S., Müller, W. J., and Schäfer, K. (2004). Atmospheric boundary-layer structure from simultaneous SODAR, RASS, and ceilometer measurements, Atmos. Environ., 38, 273– 286, doi:10.1016/j.atmosenv.2003.09.054.

Emeis, S. and Schäfer, K. (2006). Remote Sensing Methods to Investigate Boundary-layer Structures relevant to Air Pollution in Cities, Bound.-Lay. Meteorol., 121, 377–385.

Emeis, S., Schäfer, K., and Münkel, C. (2008a). Long-term observations of the urban mixing-layer height with ceilometers, IOP Conference Series: Earth and Environ. Sci. 1, 012027.

Emeis, S., Schäfer, K., and Münkel, C. (2008b). Surface-based remote sensing of the mixing-layer height – a review, Meteorol. Z., 17, 621– 630.

Emeis, S., Schäfer, K., Münkel, C., Friedl, R., and Suppan, P. (2012). Evaluation of the Interpretation of Ceilometer Data with RASS and Radiosonde Data, Bound.-Lay. Meteorol., 143, 25– 35, doi:10.1007/s10546-011-9604-6.

Endlich, R., Ludwig, F., and Uthe, E. (1979). An automatic method for determining the mixing depth from lidar observations, Atmos. Environ., 13, 1051–1056.

Eresmaa, N., Karppinen, A., Joffre, S. M., Räsänen, J., and Talvitie, H. (2006). Mixing height determination by ceilometer, Atmos. Chem. Phys., 6, 1485–1493, doi:10.5194/acp-6-1485-2006.

Fast, J. D., Gustafson, W. I., Easter, R. C., Zaveri, R. A., Barnard, J. C., Chapman, E. G., Grell, G. A., and Peckham, S. E. (2006). Evolution of ozone, particulates, and aerosol direct radiative forcing in the vicinity of Houston using a fully coupled meteorology-chemistry-aerosol model. J. Geophys. Res.-Atmos., 111(D21), D21305, doi:10.1029/2005JD006721

Floors, R., Vincent, C. L., Gryning, S.-E., Peña, A., and Batchvarova, E. (2013). The Wind Profile in the Coastal Boundary Layer: Wind Lidar Measurements and Numerical Modelling. Bound.-Lay. Meteorol., 147(3), 469–491, doi.org/10.1007/s10546-012-9791-9

Garratt, J. R. (1990). The internal boundary layer – A review, Bound.-Lay. Meteorol., 50, 171–203, doi:10.1007/BF00120524.

Garratt, J. R. (1994). Review: the atmospheric boundary layer. Earth-Science Reviews, 37(1), 89–134, doi.org/10.1016/0012-8252(94)90026-4

Haeffelin, M., Angelini, F., Morille, Y., Martucci, G., Frey, S., Gobbi, G. P., Lolli, S., O'Dowd, C. D., Sauvage, L., XuerefRémy, I., Wastine, B., and Feist, D. G. (2012). Evaluation of MixingHeight Retrievals from Automatic Profiling Lidars and Ceilometers in View of Future Integrated Networks in Europe, Bound.-Lay. Meteorol., 143, 49–75.

Hair, J. W., Hostetler, C. A., Cook, A. L., Harper, D. B., Ferrare, R. A., Mack, T. L., Welch, W., Izquierdo, L. R., and Hovis, F. E. (2008). Airborne High Spectral

Resolution Lidar for profiling aerosol optical properties. Applied Optics, 47(36), 6734–6752, doi.org/10.1364/AO.47.006734

Haman, C. L., Lefer, B., and Morris, G. A. (2012). Seasonal Variability in the Diurnal Evolution of the Boundary Layer in a NearCoastal Urban Environment. J. Atmos. Ocean. Tech., 29, 697– 710, doi:10.1175/JTECH-D-11-00114.1.

Haman, C. L., Couzo, E., Flynn, J. H., Vizuete, W., Heffron, B., and Lefer, B. L. (2014). Relationship between boundary layer heights and growth rates with ground-level ozone in Houston, Texas, J. Geophys. Res.-Atmos., 119, 6230–6245, doi:10.1002/2013JD020473.

Hoff, R. M., Harwood, M., Sheppard, A., Froude, F., Martin, J. B., and Strapp, W. (1997). Use of airborne lidar to determine aerosol sources and movement in the Lower Fraser Valley (LFV), BC. Atmos. Environ., 31(14), 2123–2134, doi.org/10.1016/S1352-2310(96)00302-0

Hong, S.-Y., Noh, Y., and Dudhia, J. (2006). A New Vertical Diffusion Package with an Explicit Treatment of Entrainment Processes. Monthly Weather Review, 134(9), 2318–2341, doi.org/10.1175/MWR3199.1

Hooper, W. P. and Eloranta, E. W. (1986). Lidar measurements of wind in the planetary boundary layer: The method, accuracy and results from joint measurements from radiosonde and kytoon, J. Appl. Meteorol. Clim., 25, 990–1001.

Hu, X.-M., Nielsen-Gammon, J. W., and Zhang, F. (2010). Evaluation of Three Planetary Boundary Layer Schemes in the WRF Model. J. Appl. Meteorol. Clim., 49(9), 1831–1844, doi.org/10.1175/2010JAMC2432.1

Jiménez, P. A., Arellano, J. V. G., Dudhia, J., and Bosveld, F. C. (2016). Role of synoptic- and meso-scales on the evolution of the boundary-layer wind profile over a coastal region: the near-coast diurnal acceleration. Meteorol. Atmos. Phys., 128(1), 39–56, doi.org/10.1007/s00703-015-0400-6

Kamp, D. and McKendry, I. (2010). Diurnal and Seasonal Trends in Convective Mixed-Layer Heights Estimated from Two Years of Continuous Ceilometer Observations in Vancouver, BC, Bound.-Lay. Meteorol., 137, 459–475, doi:10.1007/s10546-010-9535-7.

Kotthaus, S., O'Connor, E., Münkel, C., Charlton-Perez, C., Haeffelin, M., Gabey, A. M., and Grimmond, C. S. B. (2016). Recommendations for processing atmospheric attenuated backscatter profiles from Vaisala CL31 ceilometers, Atmos. Meas. Tech., 9, 3769– 3791, doi:10.5194/amt-9-3769-2016.

Kovalev, V. A. and Eichinger, W. E. (2004). Elastic Lidar: Theory, Practice and Analysis Methods, Wiley and Sons.

Lee, S.-H., Kim, S.-W., Angevine, W. M., Bianco, L., McKeen, S. A., Senff, C. J., Trainer, M., Tucker, S. C., and Zamora, R. J. (2011). Evaluation of urban surface parameterizations in the WRF model using measurements during the

Texas Air Quality Study 2006 field campaign. Atmos. Chem. Phys., 11(5), 2127–2143, doi:10.5194/acp-11-2127-2011

Li, X., and Rappenglück, B. (2014). A WRF–CMAQ study on spring time vertical ozone structure in Southeast Texas. Atmos. Environ., 97, 363–385, doi.org/10.1016/j.atmosenv.2014.08.036

Lo Feudo, T., Calidonna, C., Sempreviva, A. M., Courtney, M., De Leo, L., Federico, S., Wagner, R., and Bellecci, C. (2010). Flow evolution at a coastal site in the Central Mediterranean. Proc. International Symposium for the Advancement of Boundary Layer Remote Sensing (ISARS), Paris, France, 28-30 June 2010.

McElroy, J. L. and Smith, T. B. (1991). Lidar Descriptions of Mixing-Layer Thickness Characteristics in a Complex Terrain/Coastal Environment, J. Appl. Meteorol., 30, 585–597.

McKendry, I. G., van der Kamp, D., Strawbridge, K. B., Christen, A., and Crawford, B. (2009). Simultaneous observations of boundary-layer aerosol layers with CL31 ceilometer and 1064/532nm lidar, Atmos. Environ., 43, 5847–5852, doi:10.1016/j.atmosenv.2009.07.063.

Milroy, C., Martucci, G., Lolli, S., Loaec, S., Sauvage, L., Xueref-Remy, I., Lavrič, J. V., Ciais, P., Feist, D. G., Biavati, G., and O'Dowd, C. D. (2012). An Assessment of Pseudo-Operational Ground-Based Light Detection and Ranging Sensors to Determine the Boundary-Layer Structure in the Coastal Atmosphere, Adv. Meteor., 2012:18.

Münkel, C., Eresmaa, N., Räsänen, J., and Karppinen, A. (2007). Retrieval of mixing height and dust concentration with lidar ceilometer, Bound.-Lay. Meteorol., 124, 117–128, doi:10.1007/s10546-0069103-3.

Muñoz, R. C. and Undurraga, A. A. (2010). Daytime Mixed Layer over the Santiago Basin: Description of Two Years of Observations with a Lidar Ceilometer, J. Appl. Meteorol. Clim., 49, 1728–1741, doi:10.1175/2010JAMC2347.1.

Ngan, F., Byun, D., Kim, H., Lee, D. Rappenglueck, B., and Pour-Biazar, A. (2012). Perfomance Assessment of retrospective meteorological inputs for use in air quality modelling during TexAQS 2006, Atmos. Environ., 54, 86-96, doi: 10.1017/j.atmosenv.2012.01.035

Nielsen-Gammon, J. W., Powell, C., Mahoney, M., Angevine, W., Senff, C., White, A., Berkowitz, C., Doran, C., and Knupp, K. (2008). Multisensor Estimation of Mixing Heights over a Coastal City, J. Appl. Meteor. Clim., 47, 27–43, doi:10.1175/2007JAMC1503.1.

Pal, S., Haeffelin, M., and Batchvarova, E. (2013). Exploring a geophysical process-based attribution technique for the determination of the atmospheric boundary layer depth using aerosol lidar and nearsurface meteorological measurements, J. Geophys. Res.-Atmos., 118, 9277–9295, doi:10.1002/jgrd.50710.

Pandolfi, M., Martucci, G., Querol, X., Alastuey, A., Wilsenack, F., Frey, S., O'Dowd, C. D., and Dall'Osto, M. (2013). Continuous atmospheric boundary layer observations in the coastal urban area of Barcelona during SAPUSS, Atmos. Chem. Phys., 13, 4983– 4996, doi:10.5194/acp-13-4983-2013.

Parameswaran, K. (2001). Influence of micrometeorological features on coastal boundary layer aerosol characteristics at the tropical station, Trivandrum. J. Earth Syst. Sci., 110(3), 247–265, doi.org/10.1007/BF02702240

Petäjä, T., Järvi, L., Kerminen, V.-M., Ding, A. J., Sun, J. N., Nie, W., Kujansuu, J., Virkkula, A., Yang, X., Fu, C. B., Zilitinkevich, S., and Kulmala, M. (2016). Enhanced air pollution via aerosol-boundary layer feedback in China, Sci. Rep., 6, 18998, doi:10.1038/srep18998.

Peña, A., Floors, R., and Gryning, S.E. (2014a). The Høvsøre Tall Wind-Profile Experiment: A Description of Wind Profile Observations in the Atmospheric Boundary Layer. Bound.-Lay. Meteorol., 150(1), 69–89, doi:10.1007/s10546-013-9856-4

Peña, A., Gryning, S. E., and Hahmann, A. N. (2013). Observations of the atmospheric boundary layer height under marine upstream flow conditions at a coastal site, J. Geophys. Res.-Atmos., 118, 1924– 1940, doi:10.1002/jgrd.50175.

Piironen, A. K. and Eloranta, E. W. (1995). Convective boundary layer depths and cloud geometrical properties obtained from volume imaging lidar data, J. Geophys. Res.-Atmos., 100, 569–576.

Poltera, Y., Martucci, G., Collaud Coen, M., Hervo, M., Emmenegger, L., Henne, S., Brunner, D., and Haefele, A. (2017). PathfinderTURB: an automatic boundary layer algorithm. Development, validation and application to study the impact on in-situ measurements at the Jungfraujoch, Atmos. Chem. Phys. Discuss., doi:10.5194/acp-2016-962, in review.

Rappenglück, B., Perna, R., Zhong, S., and Morris, G. A. (2008). An analysis of the vertical structure of the atmosphere and the upper-level meteorology and their impact on surface ozone levels in Houston, Texas, J. Geophys. Res.-Atmos., 113, D17315, doi:10.1029/2007JD009745.

Rogers, R. R., Hair, J. W., Hostetler, C. A., Ferrare, R. A., Obland, M. D., Cook, A. L., Harper, D. B., Burton, S. P., Shinozuka, Y., McNaughton, C. S., Clarke, A. D., Redemann, J., Russell, P. B., Livingston J. M., and Kleinman, L. I. (2009). NASA LaRC airborne high spectral resolution lidar aerosol measurements during MILAGRO: observations and validation. Atmos. Chem. Phys., 9(14), 4811–4826, doi:10.5194/acp-9-4811-2009.

Salvador, N., Loriato, A. G., Santiago, A., Albuquerque, T., Reiz, N., Santos, J. M., Landulfo, E., Moreira, G., Lopes, F., Held, G., and Moreira, D. M. (2016). Study of the Thermal Internal Boundary Layer in Sea Breeze Conditions Using Different Parameterizations: Application of the WRF Model in the Greater

Vitória Region. Revista Brasileira de Meteorologia, 31(4), 593–609, doi.org/10.1590/0102-7786312314b20150093.

Scarino, A. J., Obland, M. D., Fast, J. D., Burton, S. P., Ferrare, R. A., Hostetler, C. A., Berg, L. K., Lefer, B., Haman, C., Hair, J. W., Rogers, R. R., Butler, C., Cook, A. L., and Harper, D. B. (2014). Comparison of mixed layer heights from airborne high spectral resolution lidar, ground-based measurements, and the WRFChem model during CalNex and CARES, Atmos. Chem. Phys., 14, 5547–5560, doi:10.5194/acp-14-5547-2014.

Schäfer, K., Emeis, S., Höß, M., Friedl, R., Münkel, C., and Suppan, P. (2011). Comparison of continuous detection of mixing layer heights by ceilometer with radiosonde observations, SPIE, 817707.

Seibert, P., Beyrich, F., Gryning, S. E., Joffre, S., Rasmussen, A., and Tercier, P. (2000). Review and intercomparison of operational methods for the determination of the mixing height, Atmos. Environ., 34, 1001–1027.

Sokół, P., Stachlewska, I. S., Ungureanu, I., and Stefan, S. (2014). Evaluation of the boundary layer morning transition using the CL-31 ceilometer signals. Acta Geophysica, 62(2), 367–380, doi.org/10.2478/s11600-013-0158-5

Steele, C. J., Dorling, S. R., von Glasow, R., and Bacon, J. (2013). Idealized WRF model sensitivity simulations of sea breeze types and their effects on offshore windfields. Atmos. Chem. Phys., 13(1), 443–461, doi.org/10.5194/acp-13-443-2013

Stein, A. F., Draxler, R. R., Rolph, G. D., Stunder, B. J. B., Cohen, M. D., and Ngan, F. (2015). NOAA's HYSPLIT Atmospheric Transport and Dispersion Modeling System. Bull. Am. Meteorol. Soc., 96(12), 2059–2077, doi.org/10.1175/BAMS-D-14-00110.1

Steyn, D. G., Baldi, M., and Hoff, R. M. (1999). The Detection of Mixed Layer Depth and Entrainment Zone Thickness from Lidar Backscatter Profiles, J. Atmos. Ocean. Tech., 16, 953–959.

Strawbridge, K. B., and Snyder, B. J. (2004). Planetary boundary layer height determination during Pacific 2001 using the advantage of a scanning lidar instrument. Atmos. Environ., 38(34), 5861–5871, doi.org/10.1016/j.atmosenv.2003.10.065

Stull, R. B. (1988). An Introduction to Boundary Layer Meteorology, Kluwer Academic.

Talbot, C., Augustin, P., Leroy, C., Willart, V., Delbarre, H., and Khomenko, G. (2007). Impact of a sea breeze on the boundary-layer dynamics and the atmospheric stratification in a coastal area of the North Sea. Bound.-Lay. Meteorol., 125(1), 133–154, doi:10.1007/s10546-007-9185-6

Tijm, A. B. C., Holtslag, A. A. M., and van Delden, A. J. (1999). Observations and Modeling of the Sea Breeze with the Return Current. Monthly Weather Review, 127(5), 625–640,

doi.org/10.1175/1520-0493(1999)127<0625:OAMOTS>2.0.CO;2

Toledo, D., Córdoba-Jabonero, C., and Gil-Ojeda, M. (2014). Cluster Analysis: A New Approach Applied to Lidar Measurements for Atmospheric Boundary Layer Height Estimation, J. Atmos. Ocean. Tech., 31, 422–436, doi:10.1175/JTECH-D-12-00253.1.

Talbot, C., Augustin, P., Leroy, C., Willart, V., Delbarre, H., and Khomenko, G. (2007). Impact of a sea breeze on the boundary-layer dynamics and the atmospheric stratification in a coastal area of the North Sea. Bound.-Lay. Meteorol., 125(1), 133–154, doi.org/10.1007/s10546-007-9185-6

Tomasi, F. D., Miglietta, M. M., and Perrone, M. R. (2011). The Growth of the Planetary Boundary Layer at a Coastal Site: a Case Study. Bound.-Lay. Meteorol., 139(3), 521–541, doi.org/10.1007/s10546-011-9592-6

Uzan, L., Egert, S., and Alpert, P. (2016). Ceilometer evaluation of the eastern Mediterranean summer boundary layer height – first study of two Israeli sites, Atmos. Meas. Tech., 9, 4387–4398, doi:10.5194/amt-9-4387-2016.

Vaisala Oyj (2011). BL-Matlab User's Guide v0.98, Vaisala Oyj, Helsinki, Finland.

Weitkamp, C. (2005). Lidar: Range-Resolved Optical Remote Sensing, Optical Sciences Series, Springer.

Wiegner, M. and Gasteiger, J. (2015). Correction of water vapor absorption for aerosol remote sensing with ceilometers, Atmos. Meas. Tech., 8, 3971–3984, doi:10.5194/amt-8-3971-2015.

Wilmot, C.-S. M., Rappenglück, B., Li, X., and Cuchiara, G. (2014). MM5 v3.6.1 and WRF v3.5.1 model comparison of standard and surface energy variables in the development of the planetary boundary layer. Geosci. Model Dev., 7(6), 2693–2707, doi:10.5194/gmd-7-2693-2014

Zhang, Y., Pan, Y., Wang, K., Fast, J. D., and Grell, G. A. (2010). WRF/Chem-MADRID: Incorporation of an aerosol module into WRF/Chem and its initial application to the TexAQS2000 episode. J. Geophys. Res.-Atmos., 115(D18), D18202, doi.org/10.1029/2009JD013443

Zhong, S., and Takle, E. S. (1992). An Observational Study of Sea- and Land-Breeze Circulation in an Area of Complex Coastal Heating. J. Appl. Meteorol., 31(12), 1426–1438, doi.org/10.1175/1520-0450(1992)031<1426:AOSOSA>2.0.CO;2